

1

UNIVERSITY OF BRISTOL

2

DOCTORAL THESIS

3

4

Investigating, implementing, and creating methods for analysing large neuronal ensembles

5

6

Author:

Thomas J. DELANEY

Supervisors:

Dr. Cian O'DONNELL

Dr. Michael C. ASHBY

7

9 *A thesis submitted in fulfillment of the requirements*

10 *for the degree of Doctor of Philosophy*

11

in the

12 Biological Intelligence & Machine Learning Unit

13 Department of Computer Science

14

August 11, 2020

15

Word count: 39000

¹⁶ **Declaration of Authorship**

¹⁷ I declare that the work in this dissertation was carried out in accordance with the requirements of the University's Regulations and Code of Practice for Research Degree Programmes
¹⁸ and that it has not been submitted for any other academic award. Except where indicated by
¹⁹ specific reference in the text, the work is the candidate's own work. Work done in collabora-
²⁰ tion with, or with the assistance of, others, is indicated as such. Any views expressed in the
²¹ dissertation are those of the author.

²² Signed:

²³ _____

²⁴ Date:

²⁵ _____

Acknowledgements

28 I would like to thank my supervisors, Cian O'Donnell and Mike Ashby, for their help, en-
29 couragement, advice, and patience over the last four years. This includes not only helping
30 with research, but also enabling and encouraging me to make the most of my opportunities
31 during that time. Without their help, I would not have grown as much as I have done in those
32 years. I very grateful for their time and effort.

33 I would also like to thank the members of the Bristol Computational Neuroscience Unit
34 for introducing me to all the various aspects of computer science, neuroscience, and machine
35 learning, of which I otherwise would not have heard. As the first person to introduce me to
36 the concept of mathematical neuroscience during my undergraduate days, and a great source
37 of advice and guidance during my PhD, I would also like to thank Conor Houghton.

38 Personally, I would like to thank my girlfriend Ashley, who has been nothing but helpful since
39 I met her.

40 Finally, I would like to thank my father, mother, brother and sister. I am truly fortunate to
41 have such a good family. I thank them for their love, encouragement, and excellent example.

42 *Abstract*

43 Since the use of multi-electrode recording in neuroscience began, the number neurons
44 being recorded in parallel has been increasing. Recently developed methods using calcium
45 or voltage imaging have also contributed to the growth in neuronal datasets. As datasets grow,
46 the need for new analysis methods also grows. In this research we attempted to address some
47 of the problems associated with reading from large neuronal ensembles using fluorescent
48 calcium indicators, and some of the problems with analysing data read from large neuronal
49 ensembles.

50 We created a biophysical model for the fluorescence trace produced by a calcium indicator
51 responding to a given spike train. Our model reproduced the characteristics of a real
52 fluorescence trace recognised by spike inference algorithms. This model will be useful for
53 anyone using or considering calcium imaging.

54 To find order in the correlated behaviour of a large multi-region neuronal ensemble, we
55 applied a novel method from network science to detect structure and communities in corre-
56 lated behaviour. We investigated the similarities between these communities and their brain
57 anatomy. Our results indicate local correlated networks function at shorter timescales (<
58 50ms), while multi-region correlated networks function over longer timescales (> 100ms).
59 This result agrees with previous findings from EEG data, but has not been shown before using
60 spiking data.

61 We developed a statistical model for the number of neurons spiking in a neuronal ensem-
62 ble based on the Conway-Maxwell-binomial distribution. Our aim was to capture correlated
63 activity in a neuronal population without measuring correlation coefficients directly. The
64 model captured correlated activity at very short timescales better than measuring correlation
65 coefficients. We also replicated one of the findings of Churchland et al. (2010) relating to
66 the quenching of neural variability at stimulus onset. We propose a connection between this
67 result and the changes in association captured by our model.

68 **Contents**

69	Declaration of Authorship	iii
70	Acknowledgements	v
71	Abstract	vii
72	1 Introduction	1
73	1.1 Overview	1
74	1.2 Modelling the fluorescence of calcium indicators	2
75	1.3 Functional networks	4
76	1.4 A new statistical model for capturing correlated behaviour	6
77	2 Sensitivity of the spikes-to-fluorescence transform to calcium indicator and neu-	
78	ron properties	9
79	2.1 Introduction	10
80	2.2 Methods	12
81	2.2.1 Calcium dynamics model	12
82	Photon release & capture	14
83	2.2.2 Parameter optimisation	15
84	Fixed parameters	16
85	2.2.3 Julia	18
86	2.2.4 Spike inference	18
87	Comparing spike inference quality	20
88	2.2.5 Perturbation analysis	20
89	2.2.6 Signal-to-noise ratio	21
90	2.2.7 Data sources	21
91	2.3 Results	21
92	2.3.1 A biophysical computational model can generate accurate fluores-	
93	cence traces from spike trains	21

94	2.3.2	Spike inference algorithms perform similarly on real data compared with time series simulated from the model	22
95	2.3.3	Relative effects of various buffers to the fluorescence signal	24
96	2.3.4	Spike inference accuracy is sensitive to indicator properties, and likely varies within and between cells	26
97	2.3.5	Single spike inference accuracy drops for high firing rates, but firing rate itself can be estimated from mean fluorescence amplitude	31
98	2.4	Discussion	31
102	3	Functional networks expand across anatomical boundaries as correlation time- scale increases	35
103	3.1	Introduction	36
104	3.2	Data	37
105	3.2.1	Brain regions	37
106	3.2.2	Video recordings	38
107	3.3	Methods	38
108	3.3.1	Binning data	38
109	3.3.2	Correlation coefficients	39
110		Total correlations, r_{SC}	39
111		Shuffled total correlations	40
112		Separating Correlations & Anti-correlations	40
113	3.3.3	Conditioning on behavioural data	40
114		Linear regression	40
115		Elastic net regularisation	41
116		Conditional covariance	42
117		Measures of conditional correlation	42
118	3.3.4	Information Theory	43
119		Entropy $H(X)$	43
120		Maximum entropy limit	44
121		Mutual Information $I(X; Y)$	45
122		Variation of Information $VI(X, Y)$	46
123		Measuring entropies & mutual information	46
124	3.3.5	Network analysis	47
125		Correlation networks	47

127	Rectified correlations	47
128	Sparsifying data networks	47
129	Communities	47
130	Weighted configuration model	48
131	Sparse weighted configuration model	48
132	Spectral rejection	48
133	Node rejection	49
134	Community detection	50
135	3.3.6 Clustering Comparison	50
136	Adjusted Rand Index	50
137	Clusterings as random variables	51
138	Information based similarity measures	52
139	Information based metrics	53
140	Comparing detected communities and anatomical divisions	53
141	3.4 Results	54
142	3.4.1 Average correlation size increases with increasing time bin width . .	54
143	3.4.2 Goodness-of-fit for Poisson and Gaussian distributions across increasing time bin widths	55
144	3.4.3 Differences between and inter- and intra- regional correlations decrease with increasing bin width	57
145	3.4.4 Connected and divided structure in correlation based networks reduces in dimension with increasing bin width	58
146	3.4.5 Detecting communities in correlation based networks	62
147	3.4.6 Functional communities resemble anatomical division at short timescales	62
148	3.4.7 Conditional correlations & signal correlations	64
149	3.4.8 Absolute correlations and negative rectified correlations	68
150	3.5 Discussion	72
151	4 A simple two parameter distribution for modelling neuronal activity and capturing neuronal association	75
152	4.1 Introduction	76
153	4.2 Data	77
154	4.2.1 Experimental protocol	77
155	4.3 Methods	78

160	4.3.1	Binning data	78
161	4.3.2	Number of <i>active</i> neurons	78
162	4.3.3	Moving windows for measurements	78
163	4.3.4	Fano factor	80
164	4.3.5	Probability Distributions suitable for modelling ensemble activity	80
165		Association	80
166		Binomial distribution	81
167		Beta-binomial distribution	81
168		Conway-Maxwell-binomial distribution	82
169	4.3.6	Fitting	84
170	4.3.7	Goodness-of-fit	86
171	4.4	Results	86
172	4.4.1	Increases in mean number of active neurons and variance in number of active neurons at stimulus onset in some regions	86
173		Primary visual cortex	87
174		Hippocampus	87
175		Thalamus	87
176	4.4.2	Conway-Maxwell-binomial distribution is usually a better fit than binomial or beta-binomial	87
177	4.4.3	Conway-Maxwell-binomial distribution captures changes in association at stimulus onset	92
178	4.4.4	Replicating stimulus related quenching of neural variability	92
179	4.5	Discussion	94
183	5	Studies with practical limitations & negative results	97
184	5.1	Dynamic state space model of pairwise and higher order neuronal correlations	98
185	5.2	A multiscale model for hierarchical data applied to neuronal data	98
187	6	Discussion	101
188	Bibliography		109

¹⁸⁹ List of Figures

190	2.1 A: Example spike train (blue) and the corresponding GCaMP6s fluorescence	
191	trace (green), data replotted from (Berens et al., 2018). Inset shows zoomed	
192	section of traces to highlight slow decay of GCaMP6s fluorescence relative	
193	to spike time intervals. B: Schematic diagram of the neuron calcium and	
194	GCaMP computational model. C: Good visual match of data fluorescence	
195	trace (green) and model simulated fluorescence (orange) in response to an	
196	identical spike train (blue).	11
197	2.2 A: Workflow to compare spike inference for real versus simulated fluores-	
198	cence data. B: True positive rates achieved by three different spike inference	
199	algorithms when applied to observed spike trains, and simulated spike trains.	
200	Data points overlaid as blue circles. The performance is similar from real	
201	and simulated data for each of the algorithms.	23
202	2.3 Calcium Buffering Dynamics (A) The proportions of bound and free cal-	
203	cium concentrations within a cell, with the associated spike train. (B)-(F)	
204	The dynamics of the concentration of (B) excited indicator bound calcium,	
205	(C) indicator bound calcium, (D) immobile endogenous buffer bound cal-	
206	cium, (E) mobile endogenous buffer bound calcium, and (F) free calcium in	
207	response to an action potential at $\sim 23.2\text{s}$	25
208	2.4 (A) An example trace for each of the five pairs of values used for the binding	
209	and unbinding rates of the fluorescent calcium indicator. (B) The signal-to-	
210	noise ratio of the modelled fluorescence traces using each of the four per-	
211	turbed value pairs, and the experimental value. The SNRs for the value pairs	
212	perturbed downward are lower than that for the unperturbed value pair or	
213	the higher value pairs. (C) The true-positive rates of the deconvolution al-	
214	gorithm's predictions when inferring from the observed data, and inferring	
215	from modelled traces using the perturbed and experimental values.	27

216	2.5 (A) An example trace for each of the five perturbed values for the concen-	
217	tration of fluorescent calcium indicator. The top two traces are produced	
218	by the lower perturbed values, the middle trace is produced by the experi-	
219	mental value, and the lowest two traces are produced when using the higher	
220	perturbed values. (B) The signal-to-noise ratio of the modelled fluorescence	
221	traces using each of the four perturbed values, and the experimental value.	
222	Extreme perturbations of the concentration either above or below the experi-	
223	mental level lowered the SNR. (C) The true-positive rates of the deconvolu-	
224	tion algorithm's predictions when inferring from the observed data, and	
225	inferring from modelled traces using the perturbed and experimental values.	
226	We found that the algorithms performs equally badly on the two most ex-	
227	treme values, and performs equally well on the experimental value, and the	
228	next higher perturbed value.	28
229	2.6 (A) An example trace for each of the five perturbed values for the concen-	
230	tration of immobile endogenous buffer. (B) The signal-to-noise ratio of the	
231	modelled fluorescence traces using each of the four perturbed values, and	
232	the experimental value. The lower values for the immobile buffer produce	
233	the same SNR as the experimental value. But the higher perturbed values	
234	produce fluorescence traces with a lower SNR. (C) The true-positive rates of	
235	the deconvolution algorithm's predictions when inferring from the observed	
236	data, and inferring from modelled traces using the perturbed and experimen-	
237	tal values.	30
238	2.7 Simulating fluorescence traces at different firing rates Example modelled	
239	traces created using simulated spike trains with a mean firing rate of 1Hz	
240	(left column), 5Hz (middle column), and 10Hz (right column). Note the	
241	difference in amplitude with different mean firing rates.	32
242	2.8 Inference quality and $\Delta F/F_0$ vs Firing rate (left) The spike inference ac-	
243	curacy when applied to 30 traces created using simulated spike trains with	
244	mean firing rates of 1, 5, and 10 Hz. (right) The mean $\Delta F/F_0$ across those	
245	30 traces for each frequency.	32
246	3.1 Probe Locations: The locations of the probes in each of the three mouse	
247	brains (Stringer et al., 2019).	38

248	3.2	Entropy Limit: The upper limit on entropy of binned spike count data as a function of the maximum observed spike count. The orange line is the analytical maximum. The blue line is the entropy of samples with $N = 1000$ data points taken from the discrete uniform distribution.	44
252	3.3	(A) An example of the correlation coefficients between two different pairs of cells, one where both cells are in the same brain region (intra-regional pair), and one where both cells are in different brain regions (inter-regional pair). The correlation coefficients have been measured using different time bin widths, ranging from 5ms to 3s. Note the increasing amplitude of the correlations with increasing bin width. (B) A raster plot showing the spike times of each pair of cells.	54
256			
260	3.4	Mean correlation coefficients measured from pairs of 50 randomly chosen neurons. (A) All possible pairs, (B) positively correlated pairs, and (C) neg- atively correlated pairs. (D) Mean and standard error of χ^2 test statistics for Poisson and Gaussian distributions fitted to neuron spike counts.	56
264			
268	3.5	(Left)The mean intra-region and inter-region correlations using all possible pairs of ~ 500 neurons, spread across 9 different brain regions. (Right) Courtesy of Stringer et al. (2019), mean inter-regional (out-of-area) correla- tion coefficients vs mean intra-regional (within-area) correlation coefficients for a bin width of 1.2s. Note that the intra-regional coefficients are higher in each case.	58
272			
276	3.6	The mean intra-regional correlations (coloured dots) and mean inter-regional correlations (black dots) for a given region, indicated on the x-axis, for dif- ferent time bin widths. Each black dot represents the mean inter-regional correlations between the region indicated on the x-axis and one other region. (A) shows these measurements when we used a time bin width of 5ms. (B) shows these measurements when we used a time bin width of 1s. Note that the difference between the mean inter-regional correlations and mean intra- regional correlations is smaller for 1s bins.	59
280			
284	3.7	Mean inter-regional (main diagonal) and intra-regional (off diagonal) corre- lation coefficients. (A) Shows these measurements when spike times were binned using 5ms time bins. (B) Shows the same, using 1s time bins. Note that the matrices are ordered according to the main diagonal values, therefore the ordering is different in each subfigure.	60

282	3.8 The number of dimensions in the k -partite and connected structure in the cor-	
283	relation based networks beyond the structure captured by a sparse weighted	
284	configuration null network model (see section 3.3.5), shown for different time	
285	bin widths. Note that the k -partite structure disappears for time bin width	
286	greater than 200ms for all three subjects. The dimension of the connected	
287	structure reduces with increasing bin width for 2 of the 3 subjects (top row).	61
288	3.9 (A-B) Correlation matrices with detected communities indicated by white	
289	lines. Each off main diagonal entry in the matrix represents a pair of neu-	
290	rons. Those entries within a white square indicate that both of those neurons	
291	are in the same community as detected by our community detection proce-	
292	dure. Matrices shown are for 5ms and 1s time bin widths respectively. Main	
293	diagonal entries were set to 0. (C-D) Matrices showing the anatomical dis-	
294	tribution of pairs along with their community membership. Entries where	
295	both cells are in the same region are given a colour indicated by the colour	
296	bar. Entries where cells are in different regions are given the grey colour also	
297	indicated by the colour bar.	63
298	3.10 (A) The variation of information is a measure of distance between cluster-	
299	ings. The distance between the anatomical ‘clustering’ and community de-	
300	tection ‘clustering’ increases with increasing time bin width. (B) The ad-	
301	justed Rand index is a normalised similarity measure between clusterings.	
302	The anatomical and community detection clusterings become less similar as	
303	the time bin width increases.	64
304	3.11 Comparing the components of the total covariance across different values for	
305	the time bin width. We observed a consistent increase in $E[\text{cov}(X, Y Z)]$ as	
306	the time bin width increased. But we saw different trends for $\text{cov}(E[X Z], E[Y Z])$	
307	for each mouse.	65
308	3.12 Comparing the components of the total covariance across different values for	
309	the time bin width. We saw a consistent increase in $\rho_{X,Y Z}$ as the time bin	
310	width increased in all three subjects. But we saw different trends in ρ_{signal} for	
311	each of the subjects.	66

312	3.13 Matrices showing the regional membership of pairs by colour, and the com-	
313	munities in which those pairs lie. (A-B) Detected communities and regional	
314	membership matrix for network based on rectified spike count correlation	
315	$\rho_{X,Y Z}$, using time bin widths of 0.005s and 1s respectively. (C-D) Detected	
316	communities and regional membership matrix for network based on rectified	
317	signal correlation ρ_{signal} , using time bin widths of 0.005s and 1s respectively.	67
318	3.14 Distance and similarity measures between the anatomical division of the neu-	
319	rons, and the communities detected in the network based on the spike count	
320	correlations $\rho_{X,Y Z}$. (A) The variation of information is a ‘distance’ mea-	
321	sure between clusterings. The distance between the anatomical ‘clustering’	
322	and the community clustering increases as the time bin width increases. (B)	
323	The adjusted Rand index is a similarity measure between clusterings. The	
324	detected communities become less similar to the anatomical division of the	
325	cells as the time bin width increases.	68
326	3.15 Distance and similarity measures between the anatomical division of the neu-	
327	rons, and the communities detected in the network based on the signal cor-	
328	relations ρ_{signal} . (A) The variation of information is a ‘distance’ measure be-	
329	tween clusterings. The distance between the anatomical ‘clustering’ and the	
330	community clustering increases as the time bin width increases. (B) The ad-	
331	justed Rand index is a similarity measure between clusterings. The detected	
332	communities become less similar to the anatomical division of the cells as	
333	the time bin width increases.	69
334	3.16 (A-B) Absolute correlation matrices with detected communities indicated by	
335	white lines. These communities are based on the absolute value of the total	
336	correlation between each pair of cells. Those entries within a white square in-	
337	dicate that both of those neurons are in the same community. Matrices shown	
338	are for 5ms and 1s time bin widths respectively. Main diagonal entries were	
339	set to 0. (C-D) Matrices showing the anatomical distribution of pairs along	
340	with their community membership. Regional membership is indicated by the	
341	colour bar. (E) Variation of information between the anatomical division of	
342	the cells, and the detected communities. (F) Adjusted Rand index between	
343	the anatomical division, and the detected communities.	70

344	3.17 (A-B) Sign reversed rectified correlation matrices with detected communities indicated by white lines. Those entries within a white square indicate that both of those neurons are in the same community. Matrices shown are for 5ms and 1s time bin widths respectively. Main diagonal entries were set to 0. (C-D) Matrices showing the anatomical distribution of pairs along with their community membership. Regional membership is indicated by the colour bar. (E) Variation of information between the anatomical division of the cells, and the detected communities. (F) Adjusted Rand index between the anatomical division, and the detected communities.	71
353	4.1 Figures showing the over-dispersion possible for a beta-binomial distribution relative to a binomial distribution. Parameters are shown in the captions. . .	82
355	4.2 Figures showing (A) the under-dispersion and (B) over-dispersion permitted by the COMb distribution relative to a binomial distribution. (C) illustrates that the p parameter of the COMb distribution does not correspond to the mean of the distribution, as it does for the binomial and beta-binomial distributions. (D) shows a heatmap for the value of the Kullback-Liebler divergence between the COMb distribution and the standard binomial distribution with same value for n , as a function of p and ν . Parameters are shown in the captions.	85
363	4.3 (A) Raster plot showing the spikes fired by 33 randomly chosen neurons in the primary visual cortex. (B-C) (B) average and (C) variance of the number of active neurons, measured using a sliding window 100ms wide, split into 100 bins. The midpoint of the time interval for each window is used as the timepoint (x-axis point) for the measurements using that window. The grey shaded area indicates the presence of a visual stimulus. The opaque line is an average across the 160 trials that included a visual stimulus of any kind. We can see a transient increase in the average number of active neurons and the variance of this number, followed by a fluctuation and another increase. .	88

372	4.4 (A) Raster plot showing the spikes fired by 33 randomly chosen neurons in	
373	the hippocampus. (B-C) (B) average and (C) variance of the number of active	
374	neurons, measured using a sliding window 100ms wide, split into 100 bins.	
375	The midpoint of the time interval for each window is used as the timepoint (x-	
376	axis point) for the measurements using that window. The grey shaded area	
377	indicates the presence of a visual stimulus. The opaque line is an average	
378	across the 160 trials that included a visual stimulus of any kind. We can see	
379	a transient increase in the average number of active neurons and the variance	
380	of this number at stimulus onset.	89
381	4.5 (A) Raster plot showing the spikes fired by 33 randomly chosen neurons in	
382	the thalamus. (B-C) (B) average and (C) variance of the number of active	
383	neurons, measured using a sliding window 100ms wide, split into 100 bins.	
384	The midpoint of the time interval for each window is used as the timepoint (x-	
385	axis point) for the measurements using that window. The grey shaded area	
386	indicates the presence of a visual stimulus. The opaque line is an average	
387	across the 160 trials that included a visual stimulus of any kind. We can	
388	see in immediate increase at stimulus onset, a subsequent fall, and another	
389	sustained increased until the stimulus presentation ends.	90
390	4.6 (A) An example of the binomial, beta-binomial, and Conway-Maxwell-binomial	
391	distributions fitted to a sample of neural activity. The Conway-Maxwell-	
392	binomial distribution is the best fit in this case. The histogram shows the	
393	empirical distribution of the sample. The probability mass function of each	
394	distribution is indicated by a different coloured line. (B) Across all samples	
395	in all trials, the proportion of samples for which each fitted distribution was	
396	the the best fit. The Conway-Maxwell-binomial distribution was the best fit	
397	for 93% of the samples taken from V1 using a bin width of 1ms.	91

398	4.7 (A) We fit a Conway-Maxwell-binomial distribution to the number of active	
399	neurons in 1ms time bins of a 100ms sliding window. We did this for all	
400	trials with a visual stimulus and took the average across those trials. We see	
401	a transient drop in value for the distribution's ν parameter at stimulus onset.	
402	This shows an increase in positive association between the neurons. (B) We	
403	measured the correlation coefficient between the spike counts of all possible	
404	pairs of neurons in the same sliding window. The took the average of those	
405	coefficients. We also did this for every visually stimulated trial, and took the	
406	average across trials. The increase in positive association is not reflected with	
407	an increase in average correlation.	93
408	4.8 (A) The mean Fano factor of the spike counts of the cells in the primary visual	
409	cortex. Means were taken across cells first, then across trials. There was a	
410	significant decrease in the Fano factors immediately after stimulus onset. (B)	
411	The mean Fano factor of the spike counts of the cells in the motor cortex. No	
412	significant change in measurements at any point.	94

⁴¹³ List of Tables

414	2.1 Fixed parameters A table of the parameters fixed before optimising the	
415	model. The values of these parameters could be changed to model differ-	
416	ent fluorescent calcium indicators.	17
417	4.1 Details of the different bin width and analysis window sizes used when bin-	
418	ning spike times, and analysing those data.	79
419	4.2 Relative dispersion of the COMb distribution, and association between Bernoulli	
420	variables as represented by the value of the ν parameter.	84
421	4.3 Proportion of samples for which each distribution was the best fit, grouped	
422	by bin width. The COMb distribution is the best fit most of the time.	92

List of Abbreviations

COMb	Conway-Maxwell-binomial (distribution)
OASIS	Online active set method to infer spikes
SNR	Signal to noise ratio
NMI	Normalised mutual information
AMI	Adjusted mutual information
VI	Variation of information

List of Symbols

$[Ca^{2+}]$	Free calcium concentration	mol
$[BCa]$	Fluorescent indicator bound calcium	mol
$[ECa]$	Endogenous mobile buffer bound calcium	mol
$[ImCa]$	Immobile mobile buffer bound calcium	mol
$[BCa^*]$	excited fluorescent indicator bound calcium	mol
k_{X_f}	binding (affinity) rate	$mol^{-1} s^{-1}$
k_{X_b}	unbinding (dissociation) rate	s^{-1}

425 **Chapter 1**

426 **Introduction**

427 **1.1 Overview**

428 Since Hodgkin and Huxley's squid experiments featuring a single axon (Hodgkin and Hux-
429 ley, 1939), to more recent research with spike sorted data from ~ 24000 neurons from 34
430 brain regions from 21 mice (Allen et al., 2019), the number of neurons contributing to elec-
431 trophysiological datasets has been growing. The number of simultaneously recorded neurons
432 has doubled approximately every seven years since the use of multi-electrode recording in
433 neuroscience began (Stevenson and Kording, 2011). Recording methods using two-photon
434 calcium imaging have also been used to extract data from populations containing over 10000
435 neurons (Peron et al., 2015). This dramatic growth in the number of neurons available for
436 analysis requires a dramatic change in analysis methods.

437 There are multiple methods for reading activity from neuronal ensembles: electrophysiolog-
438 ical, calcium imaging, and voltage imaging. Electrophysiology involves inserting electrodes
439 into the brain of an animal. The electrodes read extra-cellular membrane potential, and using
440 these readings we observe activity in the ensemble. Calcium imaging and voltage imaging
441 use indicator dyes or fluorescent proteins that emit fluorescence traces that indicate either
442 the concentration of calcium in a neuron's cytoplasm, or the neuron's membrane potential.
443 In this project, we have attempted to address some of the difficulties in collecting data from
444 these large ensembles using fluorescent calcium indicators, and some of the difficulties in
445 analysing the collected data.

446 The rest of this introductory chapter will give some background about methods of record-
447 ing from the brain, and some background for the rest of the document. Chapter two describes
448 a biophysical model for the fluorescence trace induced by a given spike train in a cell con-
449 taining a fluorescent calcium indicator. Our third chapter describes our investigations into

450 the correlated activity across different regions of a mouse behaving spontaneously. We ap-
451 plied a novel community detection method (Humphries et al., 2019) from network science
452 to correlation based networks of neurons, and observed differences in the structure of these
453 correlations at different timescales. In our fourth chapter, we detail a new statistical model
454 for the number of neurons spiking in a neuronal ensemble at any given moment. With this
455 model, we attempted to capture correlated activity in a new way. The fifth chapter is a brief
456 description of the work that yielded negative results or was abandoned. The final chapter is a
457 discussion of our work and results from the previous chapters and their implications.

458 1.2 Modelling the fluorescence of calcium indicators

459 To focus on calcium imaging for a start, a neuron that contains a fluorescent calcium indicator
460 in its cytoplasm will fluoresce when bombarded with photons. The amount that the cell
461 will fluoresce is dependent on the concentration of fluorescent indicator within the cell, and
462 the concentration of calcium within the cell. When a neuron fires an action potential, the
463 influx of free calcium ions causes an increase in fluorescence when those ions bond with the
464 fluorescent indicator and those bounded molecules are bombarded with photons. After the
465 action potential, as calcium is extruded from the cell the fluorescence returns to a baseline
466 level. This is the basic mechanism of fluorescent calcium indicator based imaging.

467 This method has some advantages over electrophysiology as measure of neuronal ensem-
468 ble activity. Many of the problems with electrophysiology are within the processes used to
469 isolate spikes in the extracellular voltage readings, and assign these spikes to individual cells.
470 These processes are collectively called ‘spike sorting’. A comparison of many different spike
471 sorting algorithms found that these algorithms only agreed on a fraction of cases (Buccino
472 et al., 2019). Furthermore, because electrodes measure extracellular voltage, neurons that do
473 not spike will not be detected. Isolating individual neurons is easier and more reliable when
474 using calcium imaging data, because cells will emit a baseline level of fluorescence when not
475 firing action potentials. Another advantage is that calcium imaging sites can be re-used for
476 weeks for longitudinal studies (Chen et al., 2013). One of the methods of delivering the flu-
477 orescent indicator is by adeno-associated viruses, consequently there can be problems with
478 indicator gradients around the infection site, and expression levels will change in individual
479 cells over weeks (Tian et al., 2009; Chen et al., 2013). This delivery method can also cause
480 cell pathology, and nuclear filling (Zariwala et al., 2012), but these problems can be solved by
481 using lines of transgenic mice (Dana et al., 2014). The fluorescence signal itself can serve a a

482 good indicator of cell activity, but similarly to electrophysiology, the aim of calcium imaging
483 is often spike detection.

484 If the imaging data is collected at a high enough frequency, and the signal-to-noise ratio
485 of the fluorescence trace is high enough, it should be possible to infer the spike times to some
486 level of accuracy. For example, the calmodulin based indicator GCaMP6s has a sufficiently
487 high signal-to-noise ratio that isolated action potentials can be detected and inferred (Chen
488 et al., 2013). Many spike inference algorithms exist (Vogelstein et al., 2010; Pnevmatikakis
489 et al., 2016; Friedrich and Paninski, 2016; Pnevmatikakis et al., 2013; Pnevmatikakis et al.,
490 2014; Deneux et al., 2016; Greenberg et al., 2018), and some of these can perform both cell
491 isolation and spike detection simultaneously (Vogelstein et al., 2010; Pnevmatikakis et al.,
492 2016; Pnevmatikakis et al., 2014; Deneux et al., 2016). But the relationship between spik-
493 ing and fluorescence change is not fully understood. For example, the fluorescent indicator
494 will act like an additional calcium buffer within the cell cytoplasm and will compete with
495 the other endogenous buffers to bind with free calcium ions. Therefore, the concentration
496 of those endogenous buffers, and the binding dynamics of those buffers will have an effect
497 on the change in fluorescence in response to an action potential. Furthermore, the binding
498 dynamics of the fluorescent indicator itself will have an effect on the change in fluorescence.
499 For example, the GCaMP series of fluorescence indicators are based on the calcium buffer
500 protein calmodulin. This protein has four binding sites, whose affinities interact non-linearly.
501 But most of the spike inference algorithms model the fluorescence as a linear function of
502 a calcium trace, and they model this calcium trace as a first or second order autoregression
503 with a pulse input to represent action potentials. Deneux et al. (2016) developed two dif-
504 ferent calcium fluorescence models behind their spike inference algorithm (MLspike) with a
505 more biological inspiration. For their simpler model, they take a physiological approach and
506 account for baseline calcium indicator dynamics. They end up with a system of first order
507 differential equations defining the dynamics of calcium concentration, baseline fluorescence,
508 and fluorescence. For their more complicated model specifically for genetically encoded cal-
509 cium indicators, they also took into account indicator binding and unbinding rates, which
510 added another equation to their system of equations. The algorithms that use the autore-
511 gression model and the MLspike algorithm are outperformed by the most recently published
512 spike inference algorithm (Greenberg et al., 2018). This algorithm takes into account the
513 binding dynamics of both the endogenous buffers and fluorescent calcium indicator, and the
514 concentrations of free calcium, indicator, and endogenous buffer within the cell cytoplasm.
515 The performance of this algorithm shows that there is value in more biologically inspired

516 models of fluorescent calcium indicators.

517 In light of the growing popularity of two-photon calcium imaging, and the lack of bio-
518 logically inspired spike inference algorithms ((Greenberg et al., 2018) developed their spike
519 inference algorithm in parallel to our work), we decided to develop a biologically inspired
520 model for fluorescent calcium indicator fluorescence. The idea being that our model would
521 take a spike train, or simply spike times, provided by the user, and return the fluorescence
522 trace that would be induced by this spike train or spike times. The model contains parameters
523 for concentrations of indicator and endogenous buffers, as well as affinity and unbinding rates
524 for these buffers. There are also parameters for the baseline concentration of free calcium in
525 the cell cytoplasm, and the cell radius (as a means for calculating the cell volume). With this
526 model, we hoped that experimentalists would be able to test out different calcium indicators
527 on the types of spike trains that they expect to encounter. This way they could decide ahead
528 of time which indicator suited their situation best. Since the output of our model is a fluo-
529 rescence trace, the spike inference models mentioned above can be applied to the modelled
530 fluorescence. This means that the model could also be used to benchmark the performance
531 of these spike inference algorithms, and to investigate the impact of variations in the model
532 on spike inference accuracy.

533 1.3 Functional networks

534 We have outlined some of the advantages that calcium imaging has over electrophysiology.
535 But electrophysiology is more useful in some situations. One particular drawback for two-
536 photon calcium imaging is that usually it can only be used for imaging near to the surface
537 of the brain. This problem can be solved by removing the tissue around the area to be im-
538 aged, and custom building a two-photon microscope Dombeck et al., 2010. Imaging with
539 three (or presumably more) photons may solve this problem in the future (Ouzounov et al.,
540 2017). A better option for reading activity from neurons beyond the surface of the brain is to
541 use Neuropixels probes (Jun et al., 2017). These probes can be used to read from thousands
542 of neurons simultaneously in many different areas of the brain (Allen et al., 2019; Stringer
543 et al., 2019; Steinmetz, Carandini, and Harris, 2019; Steinmetz et al., 2019). This brings us
544 to another problem for which we require new innovations in our analysis methods. Specif-
545 ically, analysing correlated behaviour in neural ensembles consisting of neurons from many
546 different brain regions.

547 Until the invention of new technologies such as the Neuropixels probes, most elec-
548 trophysiology datasets read from neurons in only one or two regions. Therefore most of
549 the research on interactions between neurons in different regions is limited to two regions
550 (Wierzynski et al., 2009; Patterson et al., 2014; Girard, Hupé, and Bullier, 2001). In chapters
551 3 and 4 we used datasets with neurons from 9 and 5 different brain regions respectively. In
552 their review of the interaction between growing the number of neurons in datasets and the
553 analysis methods applied to those dataset, Stevenson and Kording (2011) assert that an im-
554 portant objective of computational neuroscience is to find order in these kinds multi-neuron
555 of datasets. This was our main aim for the research described in chapter 3.

556 In light of recent findings based on correlated behaviour showing that spontaneous be-
557 haviours explain activity in many different parts of the brain that would otherwise be regarded
558 as noise (Stringer et al., 2019), that satiety is represented brain wide (Allen et al., 2019), and
559 that exploratory and non-exploratory states are represented in the amygdala (Gründemann
560 et al., 2019), it was clear that state representation or motor control had an influence on cor-
561 related behaviour in areas of the brain not usually associated with these tasks. Also, given
562 differences in timescales of fluctuations in different brain regions (Murray et al., 2014), and
563 different timescales for event representation in different brain regions (Baldassano et al.,
564 2017), we decided to investigate brain wide correlated behaviour at timescales ranging from
565 5ms up to 3s.

566 We started off measuring the correlations in spike counts between individual neurons in
567 our ensemble. These measurements induced a weighted undirected graph where each node
568 represented a neuron, and the weight of each edge was the strength of the correlation be-
569 tween the neurons represented by the nodes at either end of that edge. In order to put the
570 neurons into groups with correlated behaviour, we applied a novel community detection al-
571 gorithm (Humphries et al., 2019) to this graph. We repeated this analysis for timescales
572 from milliseconds to seconds. Bear in mind that our correlation based graph was completely
573 agnostic of the anatomical regions in which our cells resided. We then compared our corre-
574 lated communities to their anatomy at each timescale. In this way, we used a novel method,
575 never applied neuronal data before, to analyse the makeup of correlated communities across
576 different regions at different timescales.

577 1.4 A new statistical model for capturing correlated behaviour

578 Many important findings have been made by measuring the correlations between binned
 579 spike counts, but there are some problems with this method of analysis. Firstly, the width
 580 of the bins used to bin spike times into spike counts has an effect on the magnitude of the
 581 correlations measured. Using a short bin width can cause your measurements to be artificially
 582 small (Cohen and Kohn, 2011). This may not be an issue if one is considering relative size of
 583 correlations when using the same bin width, but it is still not ideal. Secondly, while pairwise
 584 correlations can capture most of the information in a small network (up to 40 cells) of highly
 585 correlated cells (Schneidman et al., 2006), a model based on pairwise correlations alone will
 586 fail to capture the activity of larger (~ 100 cells) networks, higher order correlated activity
 587 is required (Ganmor, Segev, and Schneidman, 2011). One problem with these higher order
 588 correlations is that they may be defined in different ways (Staude, Grün, and Rotter, 2010).
 589 Furthermore if we want to include them in a model this usually involves greatly increasing the
 590 number of parameters to fit, which increases the dimension of the parameter space leading
 591 to the ‘curse of dimensionality’. Some models attempt to sidestep these problems while
 592 still capturing higher-order correlations. These models attempt to capture the relationship
 593 between each individual neuron in the ensemble, and the ensemble as a whole. Okun et al
 594 (2015) called the strength of this relationship the ‘population coupling’, and demonstrated
 595 that this quantity can predict an individual neuron’s response to optogenetic stimulation of
 596 the whole ensemble. They also showed that this quantity was an indicator of the neuron’s
 597 synaptic connectivity (Okun et al., 2015). With the ‘population tracking model’, O’Donnell
 598 et al. (2016) linked the probability of firing an action potential for each individual neuron
 599 with the distribution of the number of active neurons. This allowed model fitting for a large
 600 number of neurons, as well as calculation of full pattern probabilities, and population entropy
 601 (O’Donnell et al., 2017).

602 In this work, we also aimed to capture correlated behaviour between the neurons in a
 603 neuronal ensemble without measuring correlations directly. Correlation coefficients capture
 604 the linear component of the relationship between two random variables, but will not mea-
 605 sure any relationship beyond linearity. Also, measuring correlation coefficients using short
 606 timebins can be difficult for neuronal data (Cohen and Kohn, 2011). We decided to abandon
 607 correlation, and we aimed to quantify a more general concept of association by modelling
 608 the number of active neurons in the ensemble using a Conway-Maxwell-binomial (COMb)
 609 distribution (Kadane, 2016).

610 The COMb distribution is a probability distribution over the number of successes in a
611 sequence of Bernoulli trials, where these trials can be associated in some way. The COMb
612 distribution is an extension of the standard binomial distribution, with an additional parameter
613 to model association between the Bernoulli variables. Using this additional parameter the
614 distribution can capture positive association, where the Bernoulli variables tend to take the
615 same value, negative association, where the Bernoulli variables tend to take opposite values,
616 or no association i.e. the standard binomial distribution.

617 We fit a COMb distribution to spike sorted electrophysiological data taken from five
618 different regions in the brain of an awake mouse exposed to visual stimuli (Steinmetz et al.,
619 2019). We examined whether or not a model based on the COMb distribution was able to
620 capture changes in the number of active neurons in these neuronal ensembles in response to
621 the stimuli. We also investigated the relationship between the changes as captured by the
622 COMb model and the change in neural variability as measured by Churchland et al. in their
623 famous paper (Churchland et al., 2010).

624 Our overall aim was to investigate some of the challenges in analysing large ensembles
625 of neurons present today. That included collecting the data to analyse (via calcium imaging),
626 and subsequently analysing these data. We felt that this was a worthwhile project because
627 the size of datasets, in terms of numbers of neurons and data collected, is growing rapidly.
628 Consequently these challenges will only become greater unless they are addressed. This is
629 our attempt at addressing them.

630 **Chapter 2**

631 **Sensitivity of the**
632 **spikes-to-fluorescence transform to**
633 **calcium indicator and neuron**
634 **properties**

635 *Abstract*

636 Fluorescent calcium indicators such as GCaMP are widely used to monitor neuronal activity.
637 However the relationship between the fluorescence signal and the underlying action potential
638 firing is poorly understood. This lack of knowledge makes it difficult for experimenters
639 to decide between different indicator variants for a given application. We addressed this
640 problem by studying a basic biophysical model of calcium dynamics in neuronal soma. We
641 fit the model parameters to publicly available data where GCaMP6s fluorescence and whole-
642 cell electrophysiological recordings were made simultaneously in the same single neurons.
643 We systematically varied the model's parameters to characterise the sensitivity of spike train
644 inference algorithms to the calcium indicator's main biophysical properties: binding rate,
645 dissociation rate, and molecular concentration. This model should have two potential uses:
646 experimental researchers may use it to help them select the optimal indicator for their desired
647 experiment; and computational researchers may use it to generate simulated data to aid design
648 of spike inference algorithms.

649 **2.1 Introduction**

650 Although fluorescent calcium indicators such as GCaMP are widely used to monitor neuronal
651 activity, the relationship between the fluorescence signal and the underlying action potential
652 firing is imperfect. The fluorescence signal has a low signal-to-noise ratio, and most indica-
653 tors' kinetics are slow relative to the millisecond-timescale dynamics of the membrane volt-
654 age (example in figure 2.1A). This makes spike inference difficult. Furthermore, the effects
655 of the indicator and cell properties on the fluorescence signal are unknown. For example,
656 genetically encoded indicators can accumulate within neurons over weeks and months (Chen
657 et al., 2013). Studies using calcium-sensitive fluorescent dyes have shown that indicator con-
658 centration has substantial effects on the spike-to-fluorescence relationship (Maravall et al.,
659 2000). Therefore spike rates inferred from GCaMP fluorescence signals may give mislead-
660 ing results if comparing across imaging sessions. More generally, the poor understanding of
661 the spike-to-fluorescence transform means experimenters may not know whether to trust the
662 outputs of spike train inference methods in any given application.

663 Spike trains are usually inferred from the time series of intensity values of one pixel of the
664 fluorescence image, where the pixel is located at the cell's soma. The problems of identifying
665 these pixels, and inferring spikes from their time series can solved separately or together.
666 When attempting to infer spikes, the fluorescence trace is modelled as a linear combination of
667 calcium concentration dynamics, a baseline calcium concentration, and some Gaussian noise.
668 The calcium concentration dynamics are modelled as an autoregressive process of degree 1
669 or 2 with a pulse input corresponding to the spike train, or the number of spikes fired in a
670 time step. The model includes no dynamics for the fluorescent indicator itself. Furthermore,
671 in order to make this model into an easily solvable linear programming problem the number
672 of spikes fired in a timestep is not restricted to non-negative integers but to arbitrary non-
673 negative values (Vogelstein et al., 2010; Pnevmatikakis et al., 2016; Friedrich and Paninski,
674 2016; Pnevmatikakis et al., 2013; Pnevmatikakis et al., 2014). More biologically inspired
675 spike inference models do exist (Deneux et al., 2016), but their fundamentals are very similar.
676 In this work, we investigated the effect of changing dynamics and buffer concentrations on
677 the accuracy of the inference algorithms based on these models.

678 The aim of this project was to model the fluorescence traces produced by a fluorescent
679 calcium indicator in a neuron soma resulting from a specific spike train, given calcium indi-
680 cator parameters such as binding rate, dissociation rate, and molecular concentration. Such

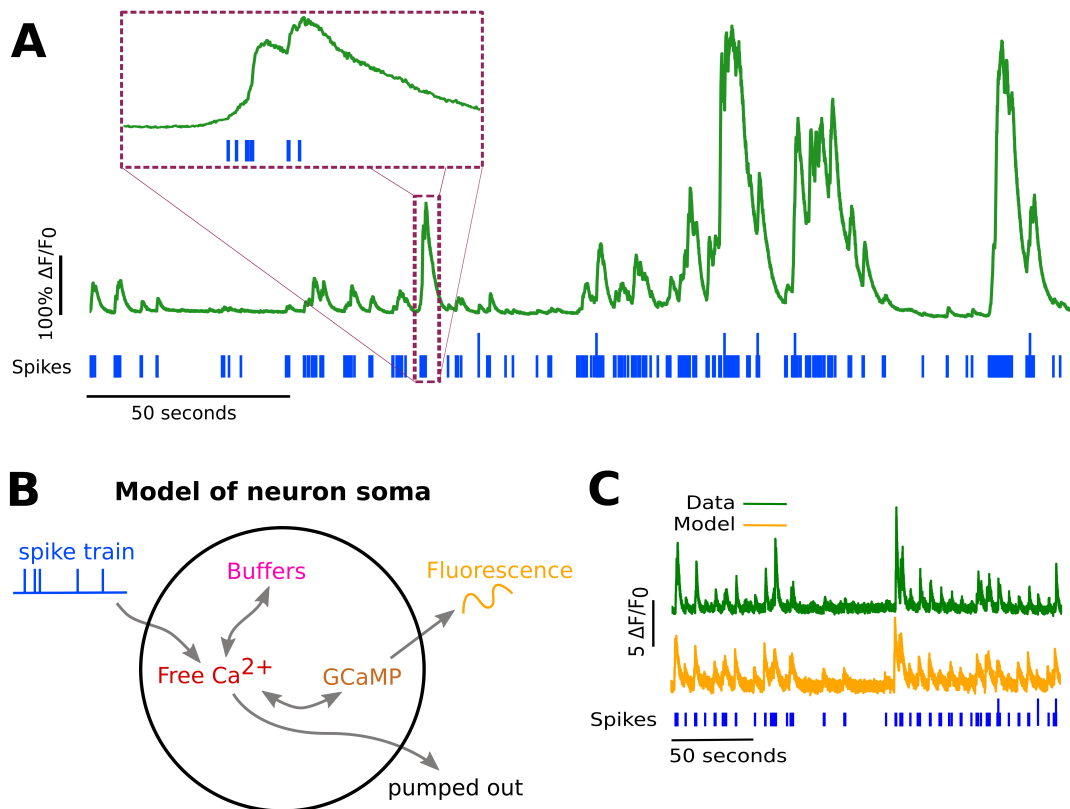


FIGURE 2.1:

- A: Example spike train (blue) and the corresponding GCaMP6s fluorescence trace (green), data replotted from (Berens et al., 2018). Inset shows zoomed section of traces to highlight slow decay of GCaMP6s fluorescence relative to spike time intervals.
- B: Schematic diagram of the neuron calcium and GCaMP computational model.
- C: Good visual match of data fluorescence trace (green) and model simulated fluorescence (orange) in response to an identical spike train (blue).

681 a model would allow benchmarking of various spike inference algorithms, and enable under-
682 standing of how indicator characteristics affect the quality of spike train inference.

683 The model we developed consisted of free calcium, fluorescent indicator molecules, and
684 mobile and immobile endogenous calcium buffers. The indicator molecules which were
685 bound to a calcium molecule could be either excited, i.e. able to release a photon, or relaxed.
686 In order to reproduce the noise inherent in the data collection, we modelled the release of
687 photons from the excited indicator bound calcium as a stochastic process.

688 The fluorescence traces produced by the simulation were calibrated to reproduce the
689 signal-to-noise ratio observed in experimental data. Previously published spike inference
690 algorithms were then used to infer spike trains from the experimental fluorescence traces and
691 the modelled fluorescence traces. The parameters of the model were then varied in order to
692 determine the effect on the system dynamics and the effects on spike inference.

693 2.2 Methods

694 2.2.1 Calcium dynamics model

695 We wrote a biophysical model of the calcium dynamics within a cell soma. When a neuron
696 fires an action potential, voltage-dependent calcium ion-channels open up that allow a current
697 of calcium ions (Ca^{2+}) to flow into the neuron (Koch, 1999). The increase in the free calcium
698 ion concentration inside of the cell, along with changes in the concentration of potassium
699 and sodium, causes the change in cell membrane potential, which must be repolarised. The
700 repolarising process consists of free calcium ions leaving the cell through open ion channels,
701 or binding to molecules within the cell called buffers, or calcium storage by organelles such
702 as the endoplasmic reticulum. A diagram illustrating the cell, its channels, and its buffers
703 can be seen in figure 2.1A. There are several different types of calcium buffer, each with
704 different dynamics and different concentrations within different types of excitable cell. The
705 fluorescent calcium indicator is another calcium buffer, with the useful property that when it
706 is bound to a calcium ion, the bound molecule may become excited by a photon and release
707 a photon in return. This is what creates the fluorescence. After the action potential has taken
708 place, the free calcium concentration within the cell will return to a baseline level (Maravall
709 et al., 2000).

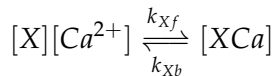
710 We modelled the the dynamics of five molecular concentrations,

- 711 • Free calcium ion concentration, $[\text{Ca}^{2+}]$

2.2. Methods

- 712 • Fluorescent indicator bound calcium, $[BCa]$
- 713 • Endogenous mobile buffer bound calcium, $[ECa]$
- 714 • Endogenous immobile buffer bound calcium, $[ImCa]$
- 715 • Excited buffered calcium, $[BCa^*]$

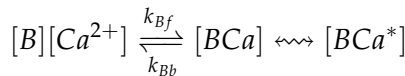
The term ‘buffering’ refers to free calcium ions coming into contact with buffer molecules followed by the binding of those molecules. Diagrammatically:



716 where $[X]$ represents any buffer molecule, and k_{X_f} and k_{X_b} represent the binding (association)
 717 and unbinding (dissociation) rates in units of per molar concentration per second (M^{-1}
 718 s^{-1}) and per second (s^{-1}) respectively. The speed of this chemical reaction is determined by
 719 the binding and unbinding rates.

720 There are a number different endogenous buffers in any neuron. Which buffers are
 721 present, and the buffers’ concentrations vary from cell to cell. In order to capture the ef-
 722 fects of mobile and immobile endogenous buffers without introducing several parameters,
 723 they were modelled as two buffers. One representing mobile buffers and the other represent-
 724 ing immobile buffers, each with their own binding and unbinding rates. Note that since the
 725 model has no spatial component, the mobile and immobile buffers only differ in their binding
 726 and unbinding rates.

The fluorescent calcium indicator behaves similarly to the other calcium buffers. The calcium is buffered by the indicator in the same way. But an indicator bound calcium molecule can become excited by absorbing the energy from a photon. An excited indicator bound calcium molecule can then release a photon to go back to its ‘relaxed’ state.



727 The released photons are captured by a photon collector. This gives us the fluorescence trace.
 728 The system of equations we used to model all of these interactions is as follows:

$$\begin{aligned} \frac{d[Ca^{2+}]}{dt} = & k_{Bb}[BCa] + k_{Eb}[ECa] + k_{Imb}[ImCa] \\ & - k_{Bf}[B][Ca^{2+}] - k_{Ef}[E][Ca^{2+}] - k_{Imf}[Im][Ca^{2+}] \\ & + \beta([Ca_0^{2+}] - [Ca^{2+}]) \end{aligned} \quad (2.1)$$

$$\frac{d[BCa]}{dt} = k_{Bf}[B][Ca^{2+}] - k_{Bb}[BCa] + r[BCa^*] - \eta[BCa] \quad (2.2)$$

$$\frac{d[ECa]}{dt} = k_{Ef}[E][Ca^{2+}] - k_{Eb}[ECa] \quad (2.3)$$

$$\frac{d[ImCa]}{dt} = k_{Imf}[Im][Ca^{2+}] - k_{Imb}[ImCa] \quad (2.4)$$

$$\frac{d[BCa^*]}{dt} = \eta[BCa] - r[BCa^*] \quad (2.5)$$

where $[Ca_0^{2+}]$ is the baseline calcium concentration within the cell soma, β is a rate defining how quickly free calcium enters or leaves the cell in the absence of an action potential, η is the excitation rate for indicator bound calcium, r is the photon release rate for the excited indicator bound calcium, and f and b are used to indicate the forward and backward rates for chemical reactions respectively. The excitation rate defines the proportion of indicator bound calcium that becomes excited at each time step. The photon release rate defines the proportion of excited indicator bound calcium that releases a photon and returns to its relaxed state at each time step. An action potential is modelled as a discontinuous increase in the free calcium concentration to an appropriate value (Maravall et al., 2000).

Note that each of the three pairs of binding and unbinding terms in the first equation has a corresponding pair in one of the subsequent three equations. Binding removes a free calcium molecule and adds a bound calcium molecule, and unbinding does the opposite.

When using this model to simulate a fluorescence trace, the system of equations above are first solved over a period of 25s without action potentials. This lets each of the five tracked chemical concentrations reach their steady state. Then we use the given spike train and the parameters to model the fluorescence trace.

Photon release & capture

We used a simple model for the photon release. The number of photons released at each time step was controlled by the number of excited indicator bound calcium molecules in the cell and a parameter called the ‘release rate’. The release rate is an optimised free parameter of the model.

As for the photon capture, in two-photon excitation microscopy the photons scattered by the fluorescent indicator get scattered in all directions. Therefore the number of photons detected is stochastic. This made the process for capturing photons the natural source of noise in the system. The number of photons captured, and therefore the intensity of the fluorescence, is modelled using a binomial distribution. The number of photons released was

2.2. Methods

755 used as the number of trials. The probability of success, or ‘capture rate’ was a free parameter
756 of the model that we optimised.

757 **2.2.2 Parameter optimisation**

758 The free parameters of the model are as follows:

759 **Calcium rate, β** Controls how quickly the concentration of free calcium will be driven to
760 the baseline concentration.

761 **Capture rate, p** The average proportion of photons captured by the photon detector.

762 **Excitation rate, η** The number of indicator bound calcium molecules that become excited
763 by photon bombardment at each time step.

764 **Release rate, r** The number of excited indicator bound calcium molecules that release a
765 photon at each time step.

766 To optimise the free parameters given a fluorescence trace, we applied the following proce-
767 dure:

- 768 1. The frequency power spectrum of the trace was measured.
- 769 2. The power spectrum was smoothed using a boxcar smoother (aka. sliding average, box
770 smoother).
- 771 3. The log of the smoothed power spectrum was measured.
- 772 4. Use the model to create a modelled fluorescence trace.
- 773 5. Apply steps 1, 2, and 3 to the modelled fluorescence trace.
- 774 6. Calculate the root mean squared difference between the log power of the actual fluo-
775 rescence trace, and the log power of the modelled fluorescence trace.
- 776 7. Calculate the root mean squared difference between the actual fluorescence trace and
777 the modelled fluorescence trace.
- 778 8. Use an optimisation algorithm to reapply this process, attempting to minimize the sum
779 of the two root mean squared differences at each iteration.

780 Using the root mean squared difference of the log power spectra as part of the objective
781 function forces the model to match the noise frequency of the actual fluorescence. Using

782 the root mean squared difference of the traces themselves forces the model to match the
783 amplitude of the fluorescence trace more accurately.

784 In order to minimise the objective function, a suite of meta-heuristic optimisation (aka.
785 black-box optimisation) algorithms were implemented on each of the traces in the dataset.
786 These methods were chosen because they don't require a gradient for the objective function
787 (gradient-free) and they are particularly useful for minimising stochastic objective functions
788 like the one we used here. The free parameters were optimised for each individual fluores-
789 cence trace. The most successful method for each trace was recorded. The method that was
790 most often successful was probabilistic descent, and the second most successful method was
791 generating set search. Both of these methods are examples of pattern search. These two
792 methods were the best optimisers on about 75% of the traces in the dataset. The other meth-
793 ods were differential evolution (with and without radius limited sampling, adaptive and not
794 adaptive), natural evolution strategy, and random search for comparison.

795 Although this optimisation procedure minimises the value of the optimisation function,
796 the value never reaches zero for a number of reasons. Firstly, the fluorescence traces carry
797 low frequency fluctuations that cannot be captured by the model. Secondly, the model as-
798 sumes that the process of calcium binding to the fluorescent indicator is linear in time (see
799 equation 1), but there are more complicated dynamics involved here. Fluorescent calcium
800 indicators, the GCaMP series for example, are often built upon the calcium binding protein
801 called 'calmodulin'. This protein has four calcium binding sites. These sites are locally split
802 into two pairs. Each pair has a different affinity for calcium, and the affinity of the binding
803 sites is affected by the occupancy of the other binding sites (Kilhoffer et al., 1992). So the
804 calcium to calcium indicator binding process is non-linear, but the model does not take this
805 into account.

806 Fixed parameters

807 As well as the optimised parameters mentioned in section 2.2.2, the model also has thirteen
808 fixed parameters. Please see table 2.1 for details of these parameters and their values. In
809 an application of the model, these parameters can be changed in order to model any given
810 fluorescent calcium indicator, or even prospective indicators that only exist in theory.

2.2. Methods

Parameter	Description	Value	Source
baseline	The baseline concentration of free calcium within the cell soma	$4.5 \times 10^{-8} M$	(Maravall et al., 2000)
cell radius	The radius of the soma (assumed to be spherical)	$10^{-5} M$	(Fiala and Harris, 1999)
endogenous	The concentration of endogenous mobile buffer within the cell soma	$10^{-4} M$	(Faas et al., 2011)
frequency	The frequency at which the spike trains are sampled.	100Hz	
immobile	The concentration of endogenous immobile buffer within the cell soma	$7.87 \times 10^{-5} M$	(Bartol et al., 2015)
indicator	The concentration of fluorescent indicator within the cell soma	$10^{-4} M$	(Maravall et al., 2000)
k_{Bb}	The unbinding rate of the fluorescent calcium indicator	$160 s^{-1}$	(Bartol et al., 2015)
k_{Bf}	The binding rate of the fluorescent calcium indicator	$7.77 \times 10^8 s^{-1} M^{-1}$	(Bartol et al., 2015)
k_{Eb}	The unbinding rate of the endogenous mobile buffer	$10^4 s^{-1}$	(Bartol et al., 2015)
k_{ef}	The binding rate of the endogenous mobile buffer	$10^8 s^{-1} M^{-1}$	(Bartol et al., 2015)
k_{Imb}	The unbinding rate of the endogenous immobile buffer	$524 s^{-1}$	(Bartol et al., 2015)
k_{Imf}	The binding rate of the endogenous immobile buffer	$2.47 \times 10^8 s^{-1} M^{-1}$	(Bartol et al., 2015)
peak	The increase in free calcium concentration within the cell induced by an action potential	$2.9 \times 10^{-7} M$	(Maravall et al., 2000)

TABLE 2.1: **Fixed parameters** A table of the parameters fixed before optimising the model. The values of these parameters could be changed to model different fluorescent calcium indicators.

811 **2.2.3 Julia**

812 The programming language used to write and execute the model was ‘Julia’. Julia is a dy-
813 namic programming language designed for technical computing. Julia was designed specif-
814 ically to provide a convenient high-level dynamic language similar to MATLAB, or Python,
815 with improved performance. Julia’s type system and Julia’s direct interfaces with C and
816 Fortran allow this aim to be achieved (Bezanson et al., 2012). The Julia version of the
817 ‘Sundials’ package for ODE solving was used to solve the system of equations above. The
818 BlackBoxOptim.jl package for Julia was used to perform the optimisation.

819 **2.2.4 Spike inference**

820 We used spike inference algorithms to compare the quality of spike inference using the mod-
821 eled traces to the quality of spike inference using the observed traces. We also used the
822 spike inference algorithms to assess the effect of parameter perturbation on the spike infer-
823 ence. Three algorithms were used:

824 **Constrained non-negative matrix deconvolution algorithm (aka CNMD algorithm)** The
825 underlying model models the fluorescence as a linear function of a calcium trace with
826 additional noise. This calcium trace is a first order autoregression with a pulse input to
827 represent action potentials. This algorithm uses a constrained version of non-negative
828 Weiner deconvolution to infer a calcium signal and a ‘spiking activity signal’ from the
829 fluorescence trace (Vogelstein et al., 2010; Pnevmatikakis et al., 2016). The spiking ac-
830 tivity signal is a non-negative vector of real numbers reflecting the cell’s activity rather
831 than an actual spike train. We inferred a spike train by choosing an optimised thresh-
832 old for the spiking activity signal. Whenever the spiking activity signal exceeded that
833 threshold, an action potential was inferred. The threshold was optimised by minimis-
834 ing the difference between the number of spikes observed and the number of spikes
835 predicted.

836 **MLSpike algorithm** Deneux et al. (2016) developed two different calcium fluorescence
837 models behind their spike inference algorithm (MLspike) with a more biological in-
838 spiration. For their simpler model, they take a physiological approach and account for
839 baseline calcium indicator dynamics. They end up with a system of first order differen-
840 tial equations defining the dynamics of calcium concentration, baseline fluorescence,
841 and fluorescence. For their more complicated model specifically for genetically en-
842 coded calcium indicators, they also took into account indicator binding and unbinding

2.2. Methods

843 rates, which added another equation to their system of equations. This algorithm uses a
844 generalised version of the Viterbi algorithm to return the spike train that maximises the
845 likelihood of producing the given fluorescence trace. The Viterbi algorithm is an algo-
846 rithm for estimating the most likely sequence of hidden states resulting in a sequence
847 of observed states in a discrete-time finite-state Markov process (Forney, 1973). In this
848 case, each hidden state is defined by the presence or absence of an action potential, and
849 each observed state is the value of the fluorescence trace at each time step. (Deneux
850 et al., 2016).

851 **Online Active Set method to Infer Spikes (OASIS)** This algorithm is once again based on
852 an auto-regressive model of the fluorescence trace, but can be generalised to any or-
853 der. Both the first and second order versions can be fit to a spike train in a reasonable
854 time. The algorithm itself is a generalisation of the pool adjacent violators algorithm
855 (PAVA) that is used in isotonic regression. The OASIS algorithm works through the
856 fluorescence trace from beginning to end, this combined with the speed of the algo-
857 rithm means that it could be used for real-time online spike inference (Friedrich and
858 Paninski, 2016). Given a fluorescence trace, the algorithm will return the most likely
859 spike train and an inferred denoised fluorescence signal.

860 In order to quantify the quality of spike inference for a given algorithm, we ran that algorithm
861 on all of the fluorescence traces in dataset number eight of the spike finder datasets. Then we
862 measured some binary classification measures on the results. These measures included

- 863 ● Accuracy
- 864 ● True positive rate (aka recall, sensitivity, hit rate)
- 865 ● True negative rate (aka specificity)
- 866 ● Precision
- 867 ● Negative predicted value
- 868 ● False negative rate (aka miss rate)
- 869 ● False positive rate (aka fall-out)
- 870 ● False discovery rate
- 871 ● False omission rate

872 In making these measurements, we allowed a tolerance of two subsequent time bins for spike
873 prediction. For example, the spike train data is a vector of 0s and 1s, with one element for
874 each time bin. A ‘0’ denotes inactivity, a ‘1’ denotes the presence of at least one action
875 potential. The inferred spike trains produced by the spike inference algorithms take the same
876 form. In our analysis, if a spike appeared in the inferred spike train up to two time frames
877 after a spike in the observed spike train, that spike was considered correctly inferred i.e. a
878 true positive. However, once a spike in the inferred spike train was matched to a spike from
879 the observed spike train, the inferred spike could not be matched to another observed spike.
880 To illustrate, if two spikes were inferred in the two time bins following an isolated observed
881 spike, the first inferred spike was considered correctly inferred, but the second inferred spike
882 was considered incorrectly inferred, i.e. a false positive.

883 The most useful measure was the true positive rate. This is because the spiking is sparse
884 and this measurement is sensitive to the number of spikes observed and inferred, but is not
885 affected by the true negative or false negative rates. After optimising the parameters for each
886 fluorescence trace we measured the spike inference quality for the observed fluorescence
887 traces, and compared this to the spike inference quality for the modelled traces.

888 When measuring the spike inference quality for higher frequency spike train (1 – 10Hz),
889 we used the accuracy as our binary classification measure. At these frequencies the variance
890 of the fluorescence trace was much higher than for sparser spiking regimes, therefore we
891 wanted to take into account the number of false negatives inferred by the algorithm.

892 Comparing spike inference quality

893 In order to compare spike inference quality we had to use methods for comparing samples.
894 When comparing the true positive rate distributions arising from two different datasets, or
895 two different algorithms on the same dataset, we compared the distributions using a paired
896 t-test.

897 2.2.5 Perturbation analysis

898 In order to measure the sensitivity of spike inference to changes in a given model parameter,
899 we perturbed the parameter and compared the quality of spike inference with the perturbed
900 parameters to the quality of spike inference with the experimental or optimised parameters.
901 In order to maximise the possibility of observing a difference due to the perturbation, we
902 perturbed the chosen parameter by a relatively large amount. For example, the experimen-
903 tal value for the molar concentration of the fluorescent indicator within the cell was $10^{-4}M$

2.3. Results

904 (Maravall et al., 2000). The perturbed values used for this parameter were $10^{-2}M$, $10^{-3}M$,
905 $10^{-5}M$, and $10^{-6}M$. The quality of the inference was compared by measuring the true posi-
906 tive rate for each perturbed value and using a t-test to compare the distributions of the results.

907 2.2.6 Signal-to-noise ratio

908 To assess the effect of perturbation on the modelled traces, we measured and compared the
909 signal to noise ratio (SNR) on each of the modelled traces. We calculated the SNR as the
910 peak change in fluorescence divided by the standard deviation of the baseline fluctuation of
911 the fluorescence trace (Tada et al., 2014). We measured these values by running the model
912 on a spike train consisting a long period of inactivity followed by one action potential. We
913 ran the model on this spike train one hundred times. We then measured the mean change
914 in fluorescence and standard deviation of baseline activity across the one hundred modelled
915 fluorescence traces, and calculated the SNR.

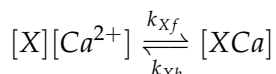
916 2.2.7 Data sources

917 All of the data used in this project was sourced from the ‘Spike Finder’ project
918 (spikefinder.codeneuro.org). The data consisted of a collection of datasets with simultane-
919 ously measured fluorescence traces and action potentials (Berens et al., 2018).

920 2.3 Results

921 2.3.1 A biophysical computational model can generate accurate fluorescence 922 traces from spike trains

To study the relationship between action potential firing and calcium fluorescence, we built a computational model of calcium dynamics in a neuronal soma. The model consisted of four dynamic variables: the concentration of free calcium, two types of endogenous buffer, and the calcium-sensitive fluorescent indicator. Each of the buffers and the indicator could independently bind and unbind with calcium. These reactions were modelled as



923 where X is the buffer concentration and Ca^{2+} is the calcium concentration. Each species
924 could therefore exist in two states: either bound with calcium or unbound. To model the

imaging process, we also added a third, excited state to the indicator. When in the calcium-bound state, the indicator could be converted to an excited state, corresponding to the absorption of a photon. The rate of this excitation process could be interpreted as the intensity of the light illuminating the sample. Once excited, the species decayed back to the unexcited state at a fixed rate, corresponding to the spontaneous emission of photons. The total emitted fluorescence signal was interpreted as proportional to this de-excitation flux. To represent experimental noise in the photon capture process, we drew a random number of captured photons at each time step from a binomial distribution, parameterised by a number p that corresponds to the mean fraction of released photons that are captured.

The model had 17 parameters in total describing the molecules' concentrations and reaction rates (Methods). We set 13 of these parameters to values from the literature. The remaining 4 parameter values we fit to publicly-available data (Berens et al., 2018), briefly explained as follows (see Methods for full details). Single neurons from acute rat cortical slices expressing GCaMP6f were imaged with two-photon microscopy while the membrane potentials of the somata of the same neurons were simultaneously recorded via whole-cell patch clamp electrophysiology. In this dataset, the electrical recordings give unambiguous information about neurons' spike times. To do the parameter fitting, we feed these spike trains as inputs to the computational model. After running, the model returns a simulated fluorescence trace. We aimed to find the model parameter values that give the best match between this simulated fluorescence trace and the real fluorescence time series recorded in the corresponding neuron. To do this we used a suite of optimisation procedures to jointly fit both the real neuron's fluorescence time series and power spectrum, which capture complementary information about the spikes-to-fluorescence mapping (Methods). We performed the fitting procedure independently for each of the 20 neurons in the spikefinder dataset (<http://spikefinder.org>). After fitting, the model produced realistic-looking fluorescence time series (Figure 2.1).

2.3.2 Spike inference algorithms perform similarly on real data compared with time series simulated from the model

Researchers often pass the fluorescence time series through a spike inference tool before performing further statistical analyses. These spike inference algorithms take the fluorescence trace as input and attempt to estimate the neuronal spike train that triggered them (Vogelstein et al., 2010; Pnevmatikakis et al., 2016; Friedrich and Paninski, 2016; Pnevmatikakis et al., 2013; Pnevmatikakis et al., 2014; Deneux et al., 2016). Part of our motivation for building

2.3. Results

this model was to allow us to investigate which properties of the cell and the calcium indicator affect the quality of spike inference? In order to trust the conclusions from our model, we should first be confident that spike inference from our simulated fluorescence traces is similar to that from the real data. To test this we passed each of the simulated fluorescence traces through three previously published spike inference algorithms, quantified their performance against the ground-truth electrophysiology data, repeated the procedure for the real calcium fluorescence time series, and compared the accuracy of the inference processes in all cases. The *true positive rate*, also known as the *recall*, the *sensitivity*, or the *probability of detection* of spike inference varied across the three inference algorithms we tried (p value and statistical test here). The constrained non-negative matrix deconvolution algorithm (Pnevmatikakis et al., 2016) (CNMD algorithm) correctly detected approximately 45% of the true spikes, the OASIS algorithm (Friedrich and Paninski, 2016) correctly detected approximately 35% of the true spikes, and the ML spike algorithm (Deneux et al., 2016) correctly detected approximately 15% of the true spikes (see figure 2.2). Notably, for two of the three inference algorithms, the quality of inference was also fairly consistent for individual spike trains, not just the group means ($p > 0.05$, paired t-test). This demonstrates that the models were generating fluorescence time series that were similarly difficult to decode as the real data, in ways that were not specific to any one inference algorithm. This is evidence that the models captured real aspects of the spikes-to-fluorescence transform.

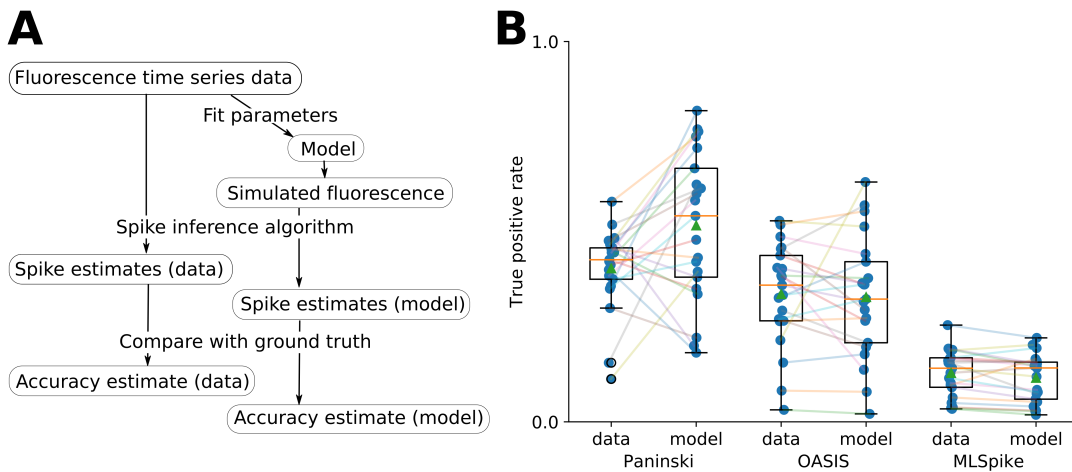


FIGURE 2.2:
A: Workflow to compare spike inference for real versus simulated fluorescence data.
B: True positive rates achieved by three different spike inference algorithms when applied to observed spike trains, and simulated spike trains. Data points overlaid as blue circles. The performance is similar from real and simulated data for each of the algorithms.

976 2.3.3 Relative effects of various buffers to the fluorescence signal

977 One of the benefits of computational models over laboratory experiments is that we can
978 observe all the variables in the simulation to gain insight into the system's dynamics, which
979 can be difficult to do in the lab. We plotted the concentrations of the various species over
980 time for a version of the model fit to one data set, in response to the same train of spikes used
981 for fitting (figure 2.3). Figure 2.3a shows the absolute values of the species concentrations,
982 summed. Consistent with experimental estimates (Maravall et al., 2000), only a small fraction
983 ($\sim 0.1\%$) of calcium is free and unbound to any buffer. Of the bound calcium, the vast
984 majority, ($\sim 96\%$) is bound to the GCaMP indicator. The two types of endogenous buffer
985 are bound to the remaining calcium ($\sim 4\%$). An influx of calcium from a single spike adds
986 very little to the total calcium, in relative terms (red line in Figure 3a).

987 When calcium entered the model neuron it was rapidly buffered (Bartol et al., 2015).
988 However the relative fractions of which buffer molecules bound to the influxed calcium was
989 dynamic, and changed over time. Figure 2.3 (b-f) shows the time course of the various species
990 over time in response to a calcium influx event from a single action potential. Crucially,
991 the indicator $[BCa]$ competed with the endogenous buffers $[ImCa]$ and $[ECa]$ – all three
992 bind calcium on similar timescales. This implies that the timescale and amplitude of the
993 $[BCa]$ variable will also depend on the binding rates and availabilities of the endogenous
994 buffers. For example if we decreased the concentration of an endogenous buffer, we might
995 expect both a faster rise time and greater peak amplitude of the $[BCa]$ signal in response to
996 a calcium influx event. The slowest component of the decay had a similar time constant for
997 $[BCa]$, $[ImCa]$ and $[ECa]$, which in turn matched the $[Ca]$ extrusion time constant in our
998 model ($\sim 6.29 \times 10^{-22} \text{Ms}^{-1}$). This implies that the buffers and the indicator had reached
999 a dynamic equilibrium and were jointly tracking the free calcium concentration as calcium
1000 was slowly extruded from the cell.

1001 Interestingly the excited bound calcium species ($[BCa^*]$) showed a qualitatively different
1002 timescale in response to a calcium influx event. This concentration is subject to the added
1003 ‘excitation and release’ dynamic, where a certain proportion of the concentration absorbs the
1004 energy from an incoming photon and goes into an ‘excited state’ at each time step. A certain
1005 proportion of the concentration releases a photon and reverts to a ‘relaxed state’ at each
1006 timestep also. This means that the excited bound calcium lags behind the bound calcium

2.3. Results

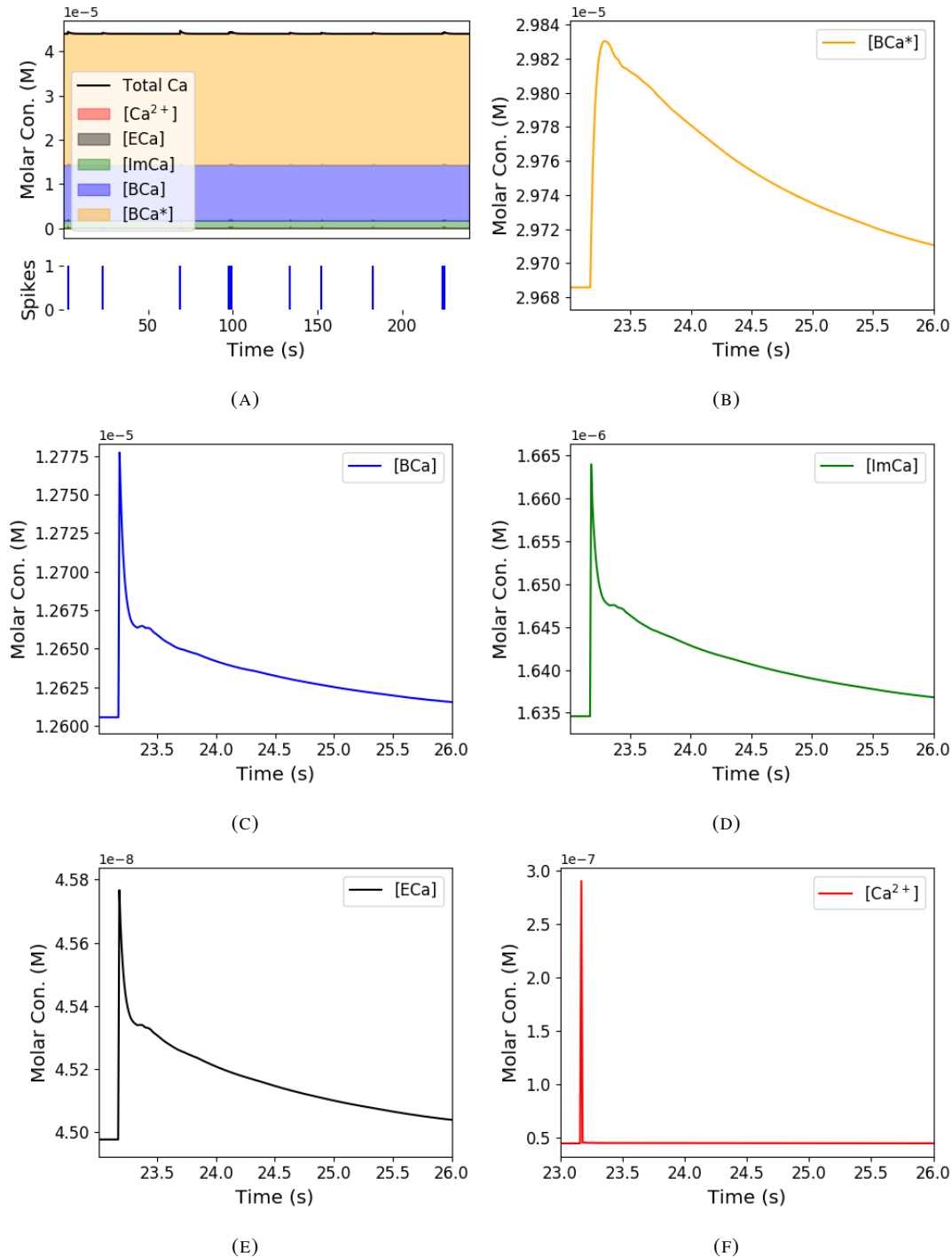


FIGURE 2.3: Calcium Buffering Dynamics (A) The proportions of bound and free calcium concentrations within a cell, with the associated spike train. (B)-(F) The dynamics of the concentration of (B) excited indicator bound calcium, (C) indicator bound calcium, (D) immobile endogenous buffer bound calcium, (E) mobile endogenous buffer bound calcium, and (F) free calcium in response to an action potential at ~ 23.2 s.

trace. We could think of the excited bound calcium trace as a low pass filtered version of the bound calcium trace.

2.3.4 Spike inference accuracy is sensitive to indicator properties, and likely varies within and between cells

The above results imply that the fluorescence signal depends on the relative properties of both GCaMP and the endogenous buffers. We next used the model to directly ask how sensitive spike inference was to these components. We focused on three key parameters that likely vary from cell to cell and experiment to experiment: GCaMP binding kinetics, GCaMP concentration, and endogenous buffer concentration.

Several variants of GCaMP itself have been made that differ in calcium binding kinetics, baseline fluorescence, fluorescence efficiency, and other factors. For example, GCaMP6f has a decay time constant of $\sim 1\text{s}$, while GCaMP6s has a decay time constant of $\sim 2\text{s}$ (Chen et al., 2013). Here we asked how these differences in binding kinetics affect spike inference. We jointly varied the calcium binding and unbinding rates of the indicator by the same factor over a range from 100-fold slower to 100-fold faster from the fitted values, and simulated the fluorescence response for each of the parameter settings in response to the same spike trains as before (figure 2.4). Notably this manipulation does not affect the indicators affinity, and therefore would not affect steady-state responses to prolonged changes in calcium. Instead it is likely to affect its sensitivity to the spike train dynamics. We computed two summary measures from the simulated fluorescence traces: the signal-to-noise ratio for a single spike (Methods, section 2.2.6), and the accuracy of spike inference for each of the spike trains. We observed a reduction in the signal-to-noise ratio and the spike inference quality when we set the binding and unbinding rates were set to one hundredth of their fitted values, and to one tenth of their fitted values. When we increased the value of both binding rates, we observed no change in these measurements. The reduction in both rates lead to smaller increases in fluorescence in response to an action potential and a longer decay time (figure 2.4a), this caused the reduction in signal-to-noise ratio. As both rates were increased, the change in $\Delta F/F_0$ in response to an action potential increased and the decay time decreased slightly, but the fluorescence trace created by these values was very similar to the trace created by the fitted values.

Second, the overall concentrations of GCaMP often varies from cell to cell. For example different cells, even of the same type in the same tissue, can express different levels of GCaMP, due to proximity to the infection site, or the cell becoming ‘nuclear-filled’ (Tian et

2.3. Results

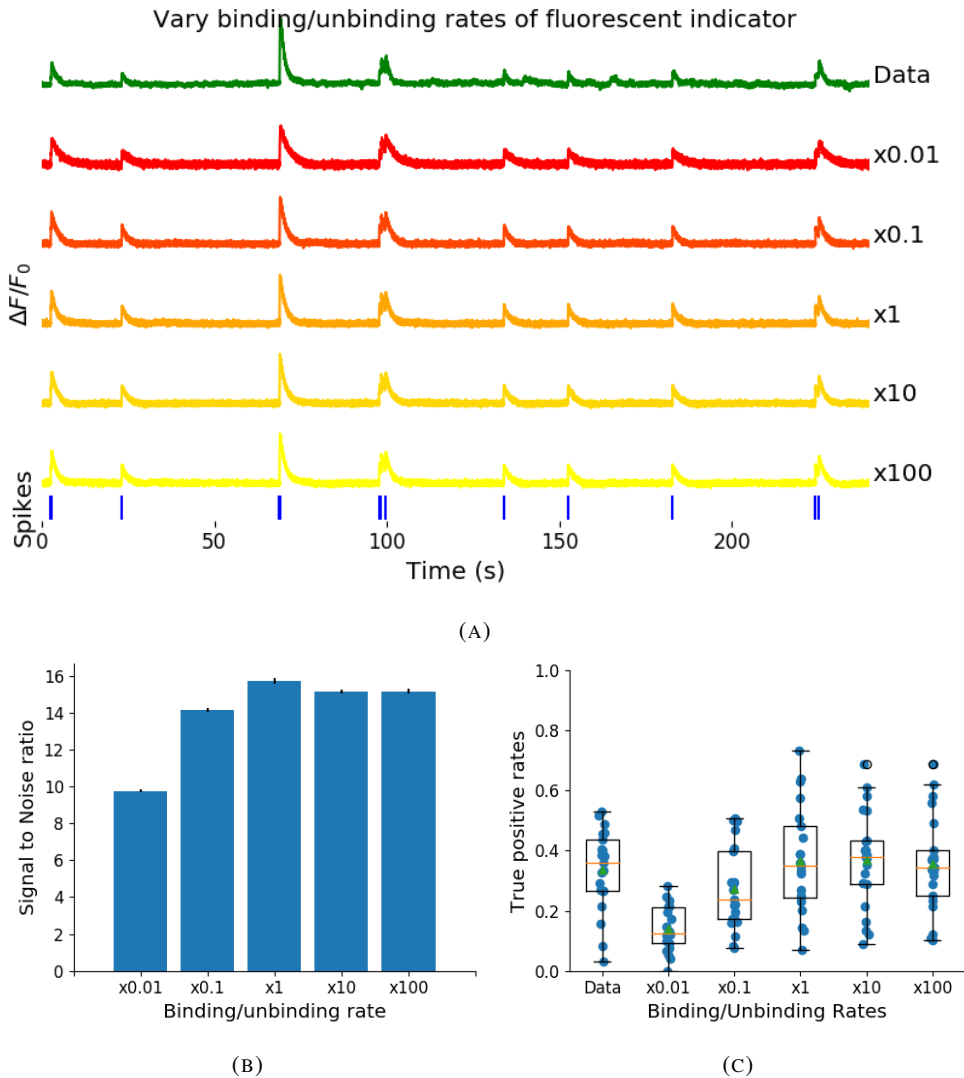


FIGURE 2.4: (A) An example trace for each of the five pairs of values used for the binding and unbinding rates of the fluorescent calcium indicator. (B) The signal-to-noise ratio of the modelled fluorescence traces using each of the four perturbed value pairs, and the experimental value. The SNRs for the value pairs perturbed downward are lower than that for the unperturbed value pair or the higher value pairs. (C) The true-positive rates of the deconvolution algorithm's predictions when inferring from the observed data, and inferring from modelled traces using the perturbed and experimental values.

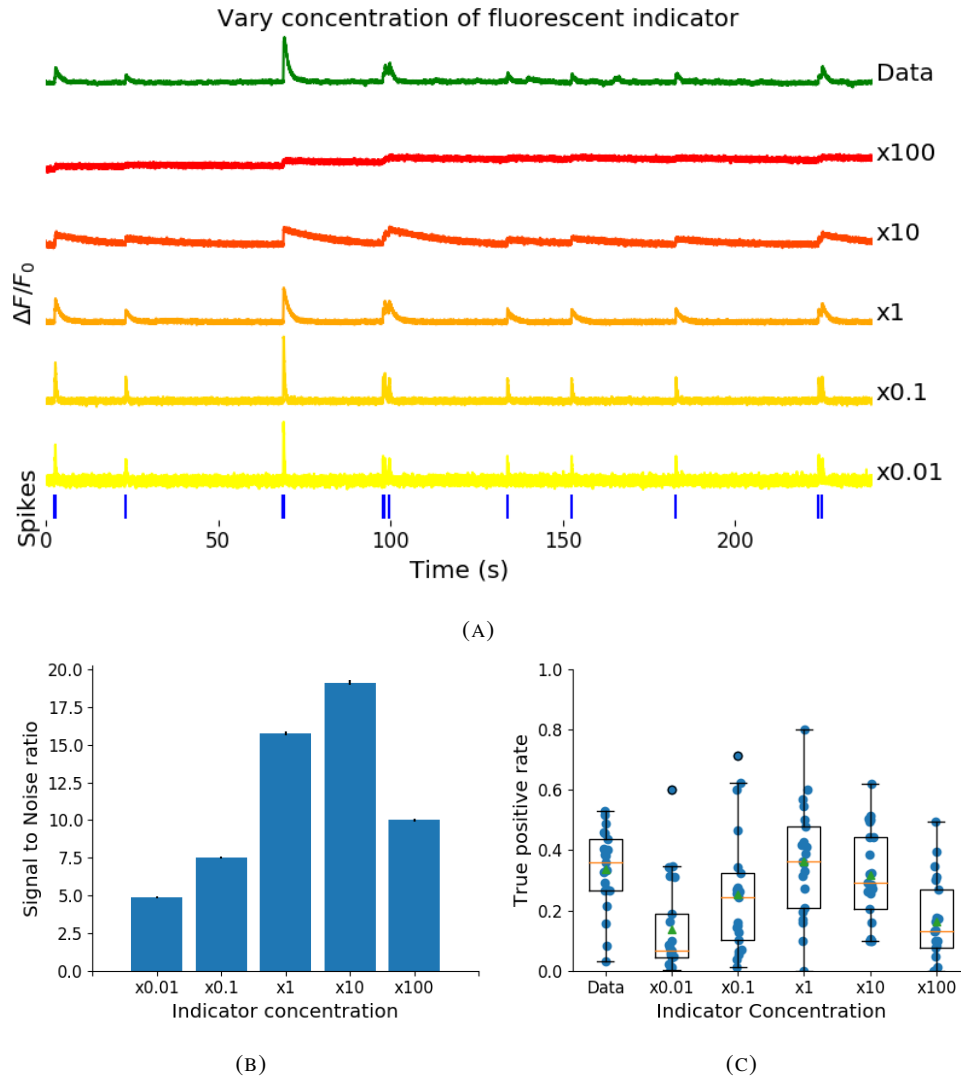


FIGURE 2.5: (A) An example trace for each of the five perturbed values for the concentration of fluorescent calcium indicator. The top two traces are produced by the lower perturbed values, the middle trace is produced by the experimental value, and the lowest two traces are produced when using the higher perturbed values. (B) The signal-to-noise ratio of the modelled fluorescence traces using each of the four perturbed values, and the experimental value. Extreme perturbations of the concentration either above or below the experimental level lowered the SNR. (C) The true-positive rates of the deconvolution algorithm's predictions when inferring from the observed data, and inferring from modelled traces using the perturbed and experimental values. We found that the algorithms performs equally badly on the two most extreme values, and performs equally well on the experimental value, and the next higher perturbed value.

2.3. Results

al., 2009; Chen et al., 2013). Also, GCaMP is often used for longitudinal experiments where the same cells are re-imaged across multiple days or weeks. However since GCaMP expression typically ramps up over time (Chen et al., 2013), the accuracy of spike inference may differ across multiple longitudinal recordings in the same cell. We addressed this by varying the concentration of calcium indicator in the model, simulating spike trains and measuring signal-to-noise ratio and spike inference accuracy on the resulting fluorescence traces. Both increasing and decreasing the concentration of the indicator had effects on the fluorescence trace, signal-to-noise ratio, and spike inference. The signal-to-noise ratio and spike inference quality decreased with decreased indicator concentration, and both showed a decrease when the indicator concentration was increased to 100 times its fitted value (figure 2.5). The signal-to-noise ratio showed an increase when the indicator concentration was increased to 10 times its fitted value, but there was no corresponding change in the spike inference quality. The decrease in indicator concentration caused a reduction in the increase in $\Delta F/F_0$ in response to an action potential, and an increase in the decay time of this increase (figure 2.5a). The increase in indicator concentration had the opposite effect, it caused an increase in the change in $\Delta F/F_0$ in response to an action potential, and a decrease in the decay time.

Third, the concentration and types of endogenous calcium buffers also vary from neuron to neuron, both within and between cell types (Bartol et al., 2015; Maravall et al., 2000; Neher and Augustine, 1992). Since the calcium buffer capacity of neurons is high, around 50-70 (Lee et al., 2000) in excitatory hippocampal pyramidal cells, around 100-250 (Lee et al., 2000) in inhibitory hippocampal pyramidal cells, and 900-200 in Purkinje cells (depending on the age of the subject), these endogenous buffers compete with GCaMP for binding to calcium, and variations in endogenous buffer concentration may affect GCaMP signal and therefore spike inference. To address this we varied the concentration of the endogenous buffer in the model neuron over five orders of magnitude from 0.8 to 8000 μM , simulated calcium fluorescence traces in response to the same set of spike trains, and performed spike inference on the resulting fluorescence time series. Increasing the endogenous buffer concentration had a substantial effect on the GCaMP fluorescence signal, both decreasing its amplitude and slowing its kinetics (figure 2.6(a)). This corresponded with a decrease in both single-spike signal-to-noise ratio (figure 2.6(b)) and spike inference accuracy (figure 2.6(c)). In contrast, decreasing endogenous buffer capacity from the fitted value had little effect on either the GCaMP signal or spike inference (figure 2.6).

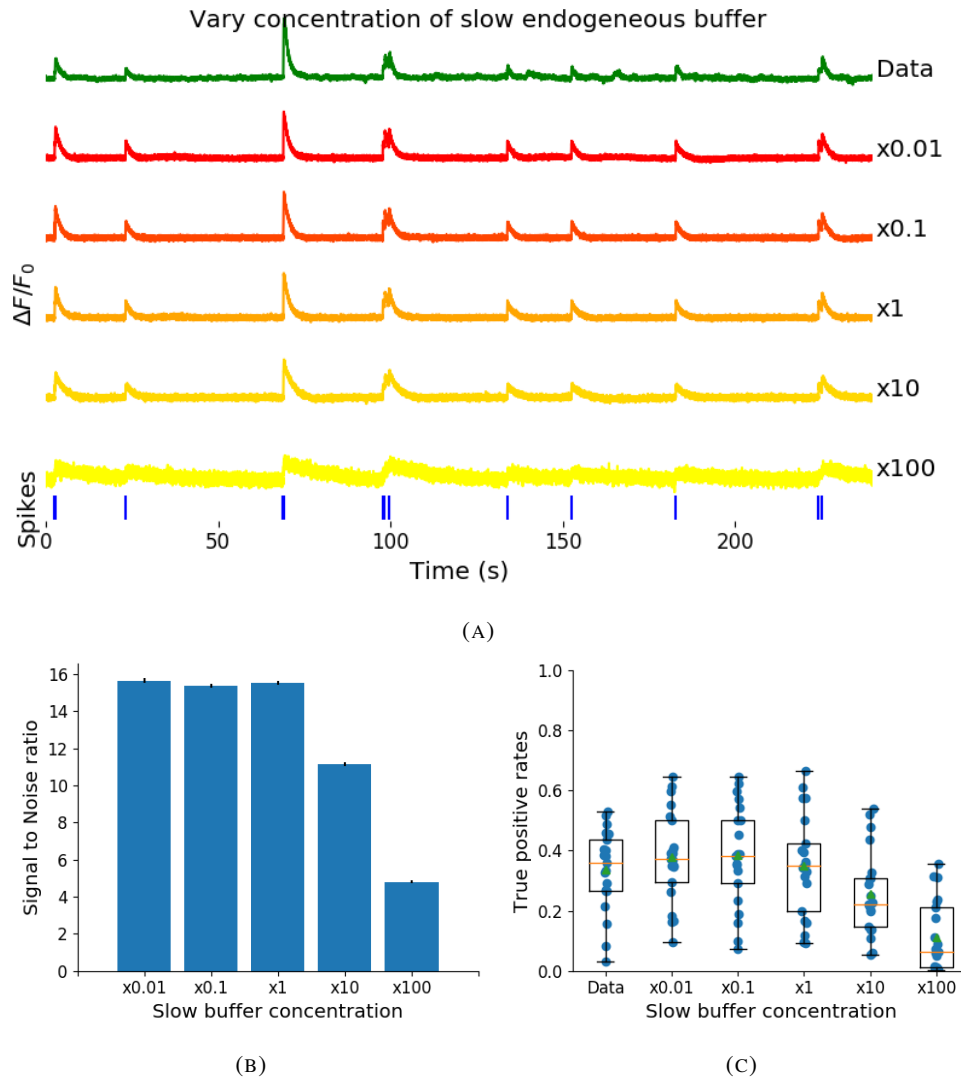


FIGURE 2.6: (A) An example trace for each of the five perturbed values for the concentration of immobile endogenous buffer. (B) The signal-to-noise ratio of the modelled fluorescence traces using each of the four perturbed values, and the experimental value. The lower values for the immobile buffer produce the same SNR as the experimental value. But the higher perturbed values produce fluorescence traces with a lower SNR. (C) The true-positive rates of the deconvolution algorithm's predictions when inferring from the observed data, and inferring from modelled traces using the perturbed and experimental values.

2.3.5 Single spike inference accuracy drops for high firing rates, but firing rate itself can be estimated from mean fluorescence amplitude

The fluorescence signal recorded from neurons using calcium indicators is typically much slower than changes in membrane potential for two reasons: first, because the calcium and the indicator have slow binding and unbinding kinetics, the signal is a low-pass filtered version of the membrane potential. Second, neuronal two-photon imaging experiments are often performed in scanning mode, which limits their frame rate to $\sim 10\text{Hz}$ or slower. This implies that multiple spike events that occur close in time might be difficult to resolve from a calcium indicator time series. Many cells, especially several types of inhibitory interneurons, fire tonically at rates higher than 10Hz . We used the model to test whether spike inference accuracy depended on the neuron's firing frequency by driving the cell with spike trains sampled from a Poisson processes of varying frequency. We simulated a variable firing rate using an Ornstein-Uhlenbeck process, and simulated the spike trains using a Poisson distribution with its rate taken from this process. Because of the high frequency firing rate of these spike trains, we used the accuracy as the measure of spike inference quality. We simulated 30 spike trains at average firing rate of 1, 5, and 10Hz , and measured the spike inference quality of all these traces. Spike inference accuracy decreased with increasing firing rate, for up to 10Hz Poisson spike trains (figure 2.8(left)). Although the accuracy remained above 90% for each of the three frequencies. We also plotted the average $\Delta F / F_0$ as a function of stimulation firing rate. We found that it increased monotonically as a function of firing rate (figure 2.8(right)).

We expected lower spike inference quality as the average spiking frequency increased. Since the fluorescence trace, in some sense, is a low pass filtered version of the spike train, a tightly packed groups of spikes will be more difficult to infer than isolated spikes. However, the increasing amplitude of the fluorescence trace with increasing frequency suggests that some spike inference algorithm could be developed based on this amplitude.

2.4 Discussion

We designed a biophysical model for the changes in free calcium and bound calcium concentrations within a cell soma with a fluorescent calcium indicator. We used this model to model the fluorescence trace resulting from a spike train in this cell. We fit the free parameters of the model by matching the power spectrum and amplitude of fluorescence traces with simultaneously measured spike trains. We inferred spikes from real fluorescence traces and

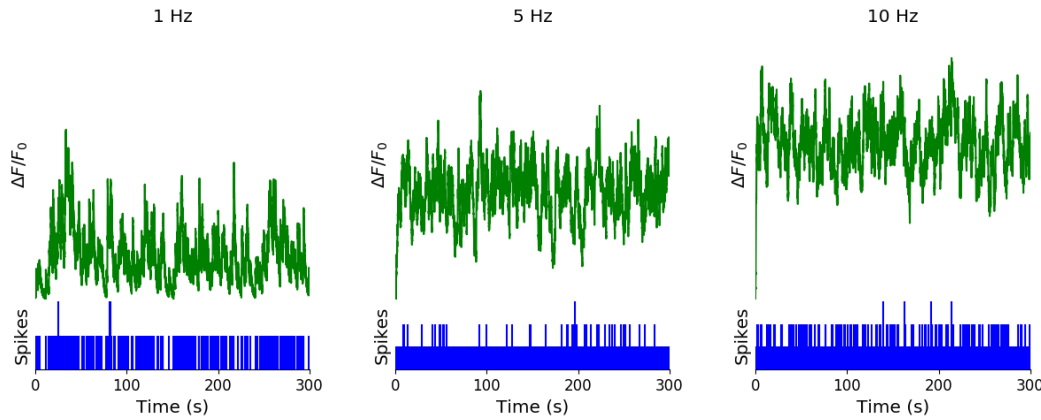


FIGURE 2.7: Simulating fluorescence traces at different firing rates Example modelled traces created using simulated spike trains with a mean firing rate of 1Hz (left column), 5Hz (middle column), and 10Hz (right column). Note the difference in amplitude with different mean firing rates.

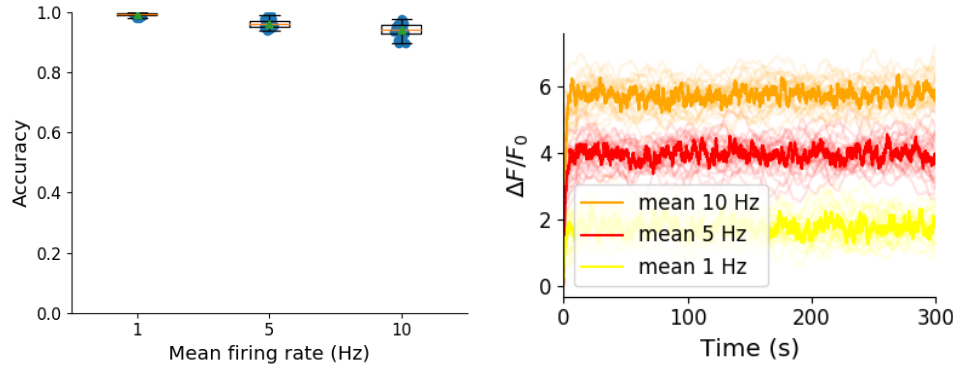


FIGURE 2.8: Inference quality and $\Delta F/F_0$ vs Firing rate (left) The spike inference accuracy when applied to 30 traces created using simulated spike trains with mean firing rates of 1, 5, and 10 Hz. (right) The mean $\Delta F/F_0$ across those 30 traces for each frequency.

1104 modelled fluorescence traces, and measured the quality of the spike inference in both cases.
 1105 We found that the spike inference quality was similar in both cases. We perturbed the concen-
 1106 tration of the calcium buffers in the model, and the binding/unbinding rates of those buffers
 1107 in the model, and measured the effect on the signal-to-noise ratio (SNR) of the modelled
 1108 fluorescence traces and the spike inference quality.

1109 For the fluorescent calcium indicator, we found that any large perturbation away from
 1110 the taken from the literature led to a reduction in SNR, and spike inference quality. For the
 1111 binding/unbinding rates, we kept the ratio of these rates constant, but altered their values in
 1112 parallel. The lower values caused a reduction in SNR, and a reduction in spike inference
 1113 quality. For the endogenous buffer concentration, an increase above the experimental value
 1114 caused a reduction in SNR and spike inference quality.

2.4. Discussion

1115 Although the model produced visually similar time series to the real data, there were a
1116 few aspects it did not capture. First, the real data featured some low-frequency components
1117 that did not appear related to the spike events. These were not captured by the models we
1118 used in this study, but could be added in future by adding a suitable low-frequency term to
1119 the resulting time series. Second, the real data seemed to have some non-linearities not cap-
1120 tured in the model, for example the response to two nearby spikes was greater than expected
1121 from the linear sum of two single spikes. This may be due to the co-operative binding of
1122 calmodulin to calcium, which gives calmodulin a supra-linear sensitivity to calcium concen-
1123 tration (Faas et al., 2011). The non-linear dynamics of this binding have been included in a
1124 recently developed spike inference model (Greenberg et al., 2018). Our model, in contrast,
1125 behaved much more linearly but could be extended in future to include such non-linearities.
1126 Third, in the real data the fluorescence peak amplitude seemed to vary from spike to spike,
1127 even for well-isolated spike events. Recent research has shown that calcium influx due to a
1128 single action potential was quite variable in pyramidal cells, and that this variability had a
1129 effect on spike inference (Éltes et al., 2019). However in our model we assumed each spike
1130 leads to the same fixed-amplitude injection of calcium to the cell, leading to much greater
1131 regularity in fluorescence peak amplitudes. This variability could be added in future versions
1132 of the model by making the injected calcium peak a random variable. Fourth, we modelled
1133 the soma as a single compartment, but in reality there is likely a non-uniform spatial profile
1134 of calcium concentration. This may matter because some endogenous buffers might access
1135 calcium right as it influxes from the extracellular space, whereas the majority of the fluo-
1136 rescence signal is more likely coming from the bulk of the cytoplasm. Future models could
1137 attempt to model these spatial dependencies to assess whether they affect the overall spike
1138 inference procedure.

1139 As well as the optimised parameters, the model has 13 fixed parameters than can be
1140 changed to simulate different types of calcium indicators. This model could be used to test
1141 the theoretical performance of proposed new types of calcium indicator. The model could
1142 also be used by developers of spike inference algorithms to test the effects of changing cal-
1143 cium indicator parameters on spike inference, or to test the affects of changing spiking char-
1144 acteristics on spike inference. For example, high firing rate vs low firing rate, or bursting vs
1145 no bursting. Given the increasing amplitude of the fluorescence trace with increasing mean
1146 firing rate, it would be possible to build a spike inference algorithm on this principle at least
1147 in part.

1148 Our model has already been used as a tool by our colleagues, for simulating fluorescence

traces in response to cells that can fire with a continuous rate between 10 and 20Hz, but do not always do so. Our colleagues found that a combination of the amplitude and the variance of the simulated fluorescence trace was the best indicator of firing rate. For example, when a cell was not firing, the amplitude and variance of the fluorescence trace was relatively low. When the cell fired with a low firing rate $\sim 1\text{Hz}$, the mean amplitude was still low but the variance of the fluorescence trace was high, and for high firing rate $10 - 20\text{Hz}$, the fluorescence amplitude was high, and the variance was low. In this way, our model may be useful for investigating firing rates underlying real fluorescence traces in response to cells which can fire in these rage ranges.

A recent paper by Greenberg et al (2018) described a biophysical model for spike train inference called the ‘Sequential binding model’. Their model for spike inference was similar to our model for fluorescence traces in that their model included parameters for two types of endogenous buffer. But this model also included dynamics for calcium binding to and unbinding from these endogenous buffers. Furthermore, this model included dynamics for calcium binding to and unbinding from the four binding sites present on a GCaMPs6 molecule. In the accuracy measurements specified in that paper, this model performed better than the MLspike algorithm, which is also partially a biophysically model, and it performed better than the constrained non-negative deconvolution algorithm. The sequential binding model also has biophysically interpretable parameters, and its fitted parameters for quantities such as buffering capacity and calcium influx upon action potential firing fall in line with experimental values (Greenberg et al., 2018). Biophysical models like this appear to be the way forward for spike inference algorithms, and would make a good complimentary tool to our fluorescence model.

1172 **Chapter 3**

1173 **Functional networks expand across
1174 anatomical boundaries as correlation
1175 time-scale increases**

1176 *Abstract*

1177 Decades of research has established that correlated spiking plays a crucial role in represent-
1178 ing sensory information. One drawback associated with the recent improvement in recording
1179 technology and consequent large datasets is the difficulty in analysing higher order correla-
1180 tions in large neuronal ensembles. One benefit of these datasets that has not yet been explored
1181 is the opportunity to compare correlations within anatomical regions to correlations across
1182 anatomical regions. In this work, we measured correlations between neurons residing in
1183 nine different brains regions in three awake and behaving mice. Using the these correlation
1184 measurements, we created weighted undirected graph networks and applied network science
1185 methods to detect functional communities in our neural ensembles. We compared these func-
1186 tional communities to their anatomical distribution. We repeated the analysis, using different
1187 timescales for our correlation measurements, and found that functional communities were
1188 more likely to be dominated by neurons from a single brain region at shorter timescales
1189 (< 100ms).

1190

3.1 Introduction

1191 Decades of research has established that correlations play a crucial role in representing sen-
1192 sory information. For example, the onset of visual attention has been shown to have a greater
1193 affect on the correlations in the macaque V4 region than on the firing rates in that region
1194 (Cohen and Maunsell, 2009). Recent findings show that spontaneous behaviours explain cor-
1195 relations in parts of the brain not associated with motor control (Stringer et al., 2019), that
1196 satiety state appears to have a brain wide representation (Allen et al., 2019), and that subject
1197 exploratory and non-exploratory states are represented in the amygdala (Gründemann et al.,
1198 2019). So, behavioural states are likely represented across many regions of the brain, not just
1199 motor related areas. In order to understand the brain, we must understand the interactions
1200 between neurons and regions.

1201 Because of limitations in recording technology almost all research has explored corre-
1202 lations between neurons within a given brain region, or within only two regions at most
1203 (Wierzynski et al., 2009; Patterson et al., 2014; Girard, Hupé, and Bullier, 2001). Rela-
1204 tively little is known about correlations between neurons in many different brain regions.
1205 However, the recent development of ‘Neuropixels’ probes (Jun et al., 2017) has allowed
1206 extracellular voltage measurements to be collected from multiple brain regions simultane-
1207 ously routinely, and in much larger numbers than traditional methods. In this project we
1208 used a publicly-available Neuropixels dataset to analyse correlations between different brain
1209 regions (Stringer et al., 2019).

1210 A drawback associated with the improvement in recording technology is an increase in
1211 the difficulty in analysing these data. For example, analysing the i th order interactions of
1212 N neurons generally requires estimation of N^i parameters. A number that becomes astro-
1213 nomical for large N . New methods are required for analysing these new large datasets. We
1214 attempted to address this requirement in this piece of research by applying a cutting-edge
1215 network science community detection method to neural data.

1216 Another unexplored area of research is the changes in cell interactions at different timescales.
1217 Studies have shown different timescales for fluctuations in spiking activity (Murray et al.,
1218 2014), and different time scales for event representation (Baldassano et al., 2017) across dif-
1219 ferent brain regions. Still most studies focus on quantifying interactions at a given timescale.
1220 But neurons may interact differently, or may interact with different neurons at different
1221 timescales. Here we explore correlated communities of neurons at different timescales.

1222 In this work, we measured correlations between binned spike counts from neurons from

3.2. Data

1223 nine different regions of the mouse brain. These measurements induced a weighted undi-
1224 rected graph or network where each neuron is represented by a node, and the strength of
1225 the connection between these nodes/neurons is the strength of the correlation between their
1226 spike counts. We then applied newly invented network methods (Humphries et al., 2019)
1227 to this network to find any community structure, and place the neurons in these correlation
1228 based communities. Finally, we compared these functional communities to the anatomical
1229 membership of the neurons.

1230 To investigate the functional communities and their relationship with anatomy at different
1231 time scales, we repeated these analyses using different length bin widths when binning spike
1232 times.

1233 To find and analyse functional networks while controlling for the subject’s behaviour, we
1234 conditioned the binned spike counts on data from a video of the subject’s face, and repeated
1235 our analysis for spike count correlations (or noise correlations) and signal correlations.

1236 3.2 Data

1237 The data that we used in this project were collected by Nick Steinmetz and his lab members
1238 (Stringer et al., 2019; Steinmetz et al., 2019).

1239 3.2.1 Brain regions

1240 Neuropixels probes were used to collect extracellular recordings (Jun et al., 2017) from three
1241 different mice. The mice were awake, headfixed, and engaging in spontaneous behaviour.
1242 The mice were of different sexes and different ages. One mouse was ‘wild-type’, the others
1243 were mutants. Details as follows:

- 1244 1. male, wild type, P73.
- 1245 2. female, TetO-GCaMP6s, Camk2a-tTa, P113
- 1246 3. male, Ai32, Pvalb-Cre, P99

1247 Eight probes were used to collect readings from 2296, 2668, and 1462 cells respectively.
1248 Data were collected from nine brain regions in each mouse:

- 1249 • Caudate Putamen (CP)
- 1250 • Frontal Motor Cortex (Frmocxt)
- 1251 • Hippocampal formation (Hpf)

- 1252 ● Lateral Septum (Ls)
 - 1253 ● Midbrain (Mb)
 - 1254 ● Superior Colliculus (Sc)
 - 1255 ● Somatomotor cortex (Sommotcx)
 - 1256 ● Thalamus (Th)
 - 1257 ● Primary visual cortex (V1)
- 1258 Readings were continuous and lasted for about 1 hour (Stringer et al., 2019; Steinmetz et al.,
1259 2019). Locations of each of the probes can be seen in figure 3.1.

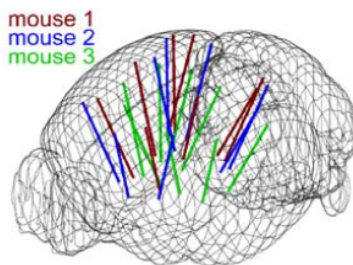


FIGURE 3.1: **Probe Locations:** The locations of the probes in each of the three mouse brains (Stringer et al., 2019).

1260 3.2.2 Video recordings

1261 Video recordings of the mouse's face were taken during the spontaneous behaviour. We
1262 had access to the top 500 principal components and top 500 eigenvectors of the processed
1263 videos. The frequency of recording was slightly less than 40Hz. Each frame contained
1264 327×561 pixels (Stringer et al., 2019; Steinmetz, Carandini, and Harris, 2019). These
1265 principal components were used as behavioural data. We controlled for these components
1266 when taking measurements conditioned on behaviour.

1267 3.3 Methods

1268 3.3.1 Binning data

1269 We transformed the spike timing data into binned spike count data by dividing the experi-
1270 mental period into time bins and counting the spikes fired by each cell within the time period
1271 covered by each of those bins. The data were divided into time bins of various widths ranging
1272 from 0.005s to 4s.

3.3. Methods

If the total length of the recording period was not an integer multiple of the time bin width, we cut off the remaining time at the end of the recording period. This period was at most 3.99s. This is far less than the total recording time of around 1 hour. So, this detail would not affect our results.

3.3.2 Correlation coefficients

We calculated Pearson's correlation coefficient for pairs of spike counts from pairs of neurons. For jointly distributed random variables X and Y , Pearson's correlation coefficient is defined as:

$$\rho_{XY} = \frac{\text{cov}(X, Y)}{\sigma_X \sigma_Y} \quad (3.1)$$

$$= \frac{E[(X - \mu_X)(Y - \mu_Y)]}{\sigma_X \sigma_Y} \quad (3.2)$$

where E denotes the expected value, μ denotes the mean, and σ denotes the standard deviation. The correlation coefficient is a normalised measure of the covariance. It can take values between 1 (completely correlated) and -1 (completely anti-correlated). Two independent variables will have a correlation coefficient of 0, but having 0 correlation does not imply independence.

If we do not know the means and standard deviations required for equation 3.1, but we have samples from X and Y , Pearson's sample correlation coefficient is defined as:

$$r_{XY} = \frac{\sum_{i=1}^n (x_i - \bar{x})(y_i - \bar{y})}{\sqrt{\sum_{i=1}^n (x_i - \bar{x})^2} \sqrt{\sum_{i=1}^n (y_i - \bar{y})^2}} \quad (3.3)$$

where $\{(x_i, y_i)\}$ for $i \in \{1, \dots, n\}$ are the paired samples from X and Y , and $\bar{x} = \frac{1}{n} \sum_{i=1}^n x_i$, and $\bar{y} = \frac{1}{n} \sum_{i=1}^n y_i$ are the sample means.

In practice we used the Python function `scipy.stats.pearsonr` to calculate the correlation coefficients.

1287 Total correlations, r_{SC}

In this context, we defined the total correlation (r_{SC}) of two cells to be the correlation between the spike counts of those cells across the entire period of spontaneous behaviour.

1290 **Shuffled total correlations**

1291 We measured the shuffled total correlations between two neurons by randomly permuting one
 1292 of the neuron's spike counts and measuring the total correlations. These shuffled correlations
 1293 were useful when measuring the effect of time bin width on correlations, and when decid-
 1294 ing which correlations should be preserved when creating correlation networks (see section
 1295 3.3.5).

1296 **Separating Correlations & Anti-correlations**

1297 In order to compare the effect of bin width on measures of negative r_{SC} (anti-correlation) and
 1298 positive r_{SC} separately, we had to separate correlated and anti-correlated pairs. To do this, we
 1299 simply measured the mean r_{SC} , taking the mean across all the bin widths. If this quantity was
 1300 positive or zero we regarded the pair as positively correlated. If this quantity was negative
 1301 we regarded the pair as anti-correlated.

1302 **3.3.3 Conditioning on behavioural data**

Our behavioural data consisted of the top 500 principal components (PCs) of a processed video recording of the mouse's face (see section 3.2.2). Denoting the spike count of a given cell by X , and the PCs by Z_1, \dots, Z_{500} , we wanted to model X as a function of Z_1, \dots, Z_{500} in order to estimate

$$E[X|Z_1, \dots, Z_{500}] = \int_{x \in X} x P(X = x|Z_1, \dots, Z_{500}) dx \quad (3.4)$$

$$= \int_{x \in X} x \frac{P(X = x, Z_1, \dots, Z_{500})}{P(Z_1, \dots, Z_{500})} dx \quad (3.5)$$

1303 Given the 500 components, a naïve estimation of $P(Z_1, \dots, Z_{500})$ or $P(X, Z_1, \dots, Z_{500})$ by
 1304 histogramming was impossible. Therefore we modelled X as a linear combination of the
 1305 PCs.

1306 **Linear regression**

1307 We modelled the spike count of a given cell, X , as a linear combination of the PCs of the
 1308 video of the mouse's face, $\mathbf{Z} = Z_1, \dots, Z_{500}$. We tried three different types of regularization

1309 • L1 or 'Lasso'

1310 • L2 or 'Ridge regression'

3.3. Methods

- 1311 • ‘Elastic net’ regularisation (a linear combination of both $L1$ and $L2$ regularisation
1312 penalties)

1313 The elastic net regularisation performed the best, so we stuck with that.

1314 **Elastic net regularisation**

Suppose we wish to model n observations of a random variable X , $\mathbf{x} = (x_1, \dots, x_n)$ using n instances of m predictors $\mathbf{Z} = (Z_1, \dots, Z_m)$. The naïve elastic net criterion is

$$L(\lambda_1, \lambda_2, \boldsymbol{\beta}) = |\mathbf{x} - \mathbf{Z}\boldsymbol{\beta}|^2 + \lambda_2|\boldsymbol{\beta}|_2 + \lambda_1|\boldsymbol{\beta}|_1 \quad (3.6)$$

where

$$|\boldsymbol{\beta}|_2 = \sum_{j=1}^m \beta_j^2 \quad (3.7)$$

$$|\boldsymbol{\beta}|_1 = \sum_{j=1}^m |\beta_j| \quad (3.8)$$

The naïve elastic net estimator $\hat{\boldsymbol{\beta}}$ is the minimiser of the system of equations 3.6 (Zou and Hastie, 2005)

$$\hat{\boldsymbol{\beta}} = \arg \min_{\boldsymbol{\beta}} L(\lambda_1, \lambda_2, \boldsymbol{\beta}) \quad (3.9)$$

1315 We implemented the model using the `ElasticNetCV` method of Python’s
1316 `sklearn.linear_models` package. We chose to put equal weighting on the $L1$ and $L2$
1317 regression parts of equation 3.6. We used 10-fold cross validation to set an optimised value
1318 for $\lambda_1 = \lambda_2$.

1319 As well as using the PCs, we also tried fitting the models using the raw video data recon-
1320 structed from the PCs and eigenvectors. These models performed worse than those using the
1321 PCs. We expected this because each representation contains the same amount of information,
1322 but the raw video representation spreads this information across many more components.
1323 This requires more parameter fitting, but given the same information.

1324 **Conditional covariance**

We calculated the expected value of the conditional covariance using the law of total covariance.

$$\text{cov}(X, Y) = E[\text{cov}(X, Y|Z)] + \text{cov}(E[X|Z], E[Y|Z]) \quad (3.10)$$

1325 where these expected values are calculated with respect to the distribution of Z as a random
1326 variable.

1327 The law of total covariance breaks the covariance into two components. The first com-
1328 ponent $E[\text{cov}(X, Y|Z)]$ is the expected value, under the distribution of Z , of the conditional
1329 covariance $\text{cov}(X, Y|Z)$. This covariance could be interpreted as the unnormalised version
1330 of what Cohen et al. (2011) call the spike count correlation (Cohen and Kohn, 2011), aka.
1331 the noise correlation. In particular, this is the covariance of the spike counts in response to
1332 repeated presentation of identical stimuli.

1333 The second component is analogous to what Cohn et al. (2011) call the *signal correlation*
1334 (Cohen and Kohn, 2011). In particular, $\text{cov}(E[X|Z], E[Y|Z])$ is the covariance between
1335 spike counts in response to different stimuli.

1336 Using our linear model, we calculated $E[X|Z_1, \dots, Z_{500}]$ for each cell X . Then we pro-
1337 ceeded to calculate

$$E[\text{cov}(X, Y|Z_1, \dots, Z_{500})] = \text{cov}(X, Y) - \text{cov}(E[X|Z_1, \dots, Z_{500}], E[Y|Z_1, \dots, Z_{500}]) \quad (3.11)$$

1338 **Measures of conditional correlation**

As a measure of expected correlation, we measured the ‘event conditional correlation’ (Maugis,
2014)

$$\rho_{XY|Z} = \frac{E[\text{cov}(X, Y|Z)]}{\sqrt{E[\text{var}(X|Z)]} \sqrt{E[\text{var}(Y|Z)]}} \quad (3.12)$$

1339 Although this is not an actual correlation, it is an intuitive analogue to the correlation as a
1340 normalised version of the covariance.

For comparison, we also measured the ‘signal correlation’

$$\rho_{\text{signal}} = \frac{\text{cov}(E[X|Z], E[Y|Z])}{\sqrt{\text{var}(E[X|Z])} \sqrt{\text{var}(E[Y|Z])}} \quad (3.13)$$

3.3. Methods

1341 this is an actual correlation.

3.3.4 Information Theory

1343 **Entropy $H(X)$**

The entropy of a random variable X , with outcomes x_1, \dots, x_N , and corresponding probabilities p_1, \dots, p_N is defined as

$$H(X) = - \sum_{n=1}^N p_n \log_2 p_n \quad (3.14)$$

1344 This quantity is also known as the information entropy or the ‘surprise’. It measures the
1345 amount of uncertainty in a random variable. For example, a variable with a probability of 1
1346 for one outcome, and 0 for all other outcomes will have 0 bits entropy, because it contains no
1347 uncertainty. But a variable with a uniform distribution will have maximal entropy as it is the
1348 least predictable. This quantity is analogous to the entropy of a physical system (Shannon,
1349 1948). Note that any base may be used for the logarithm in equation 3.14, but using base 2
1350 means that the quantity will be measured in ‘bits’.

The joint entropy of two jointly distributed random variables X and Y , where Y has outcomes y_1, \dots, y_M , is defined as

$$H(X, Y) = - \sum_{n=1}^N \sum_{m=1}^M P(X = x_n, Y = y_m) \log_2 P(X = x_n, Y = y_m) \quad (3.15)$$

1351 If X and Y are independent then $H(X, Y) = H(X) + H(Y)$. Otherwise $H(X, Y) <$
1352 $H(X) + H(Y)$. When X and Y are completely dependent and the mapping from X to Y
1353 is one-to-one, $H(X, Y) = H(X) = H(Y)$.

The conditional entropy of Y conditioned on X is defined as

$$H(Y|X) = - \sum_{n=1}^N \sum_{m=1}^M P(X = x_n, Y = y_m) \log_2 \frac{P(X = x_n, Y = y_m)}{P(X = x_n)} \quad (3.16)$$

1354 When X and Y are independent $H(Y|X) = H(Y)$. Intuitively, we learn nothing of Y by
1355 knowing X , so Y is equally uncertain whether we know X or not. If Y is totally dependent
1356 on X , then the fraction in the logarithm is 1, which gives $H(Y|X) = 0$.

1357 These entropy measures are the basis of the mutual information measure.

1358 **Maximum entropy limit**

When spiking data is binned into spike counts there is an upper limit on the entropy of these data. The maximum entropy discrete distribution is the discrete uniform distribution. A random variable with this distribution will take values from some finite set with equal probabilities. Binned spike count data will take values between 0 and some maximum observed spike count n_{\max} . A neuron with responses that maximises entropy will take these values with equal probability, i.e. if $i \in \{0, \dots, n_{\max}\}$ then $P(X = i) = \frac{1}{n_{\max} + 1}$. The entropy of this neuron will be

$$\begin{aligned} H(X) &= - \sum_{i=0}^{n_{\max}} P(X = i) \log_2 P(X = i) \\ &= - \sum_{i=0}^{n_{\max}} \frac{1}{n_{\max} + 1} \log_2 \left(\frac{1}{n_{\max} + 1} \right) \\ &= - \log_2 \left(\frac{1}{n_{\max} + 1} \right) \\ &= \log_2 (n_{\max} + 1) \end{aligned}$$

1359 Therefore, the maximum entropy of the binned spike counts of a neuron is $\log_2 (n_{\max} + 1)$.
 1360 Of course, it would be very unusual for a neuron to fire in accordance with the discrete
 1361 uniform distribution. Most measurements of entropy taken on binned spiking data will be
 1362 much lower than the maximum. See figure 3.2 to see the maximum entropy as a function of
 1363 the maximum observed spike count.

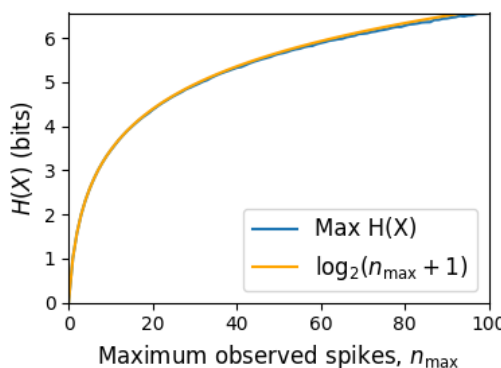


FIGURE 3.2: **Entropy Limit:** The upper limit on entropy of binned spike count data as a function of the maximum observed spike count. The orange line is the analytical maximum. The blue line is the entropy of samples with $N = 1000$ data points taken from the discrete uniform distribution.

3.3. Methods

1364 Mutual Information $I(X;Y)$

1365 The mutual information can be defined mathematically in a number of ways, all of which are
1366 equivalent. These definitions illustrate the different ways of interpreting the mutual informa-
1367 tion.

For two jointly distributed random variables X and Y , the mutual information $I(X;Y)$ is defined as

$$I(X;Y) = H(Y) - H(Y|X) \quad (3.17)$$

$$= H(X) - H(X|Y) \quad (3.18)$$

1368 Equation 3.17 fits with the following intuition: The mutual information between X and Y is
1369 the reduction in uncertainty about X gained by knowing Y , or vice versa. We could also say
1370 the mutual information is the amount of information gained about X by knowing Y , or vice
1371 versa.

Another useful entropy based definition for the mutual information is

$$I(X;Y) = H(X) + H(Y) - H(X,Y) \quad (3.19)$$

1372 This definition is useful because it does not require the calculation of conditional probabili-
1373 ties.

The mutual information can also be defined in terms of marginal, joint, and conditional distributions. For example,

$$I(X;Y) = - \sum_{n=1}^N \sum_{m=1}^M P(X = x_n, Y = y_m) \log_2 \frac{P(X = x_n, Y = y_m)}{P(X = x_n)P(Y = y_m)} \quad (3.20)$$

Notice that this can be rewritten as a Kullback–Leibler divergence.

$$I(X;Y) = D_{KL}(P(X,Y) || P(X)P(Y)) \quad (3.21)$$

1374 So, we can also think of the mutual information as a measure of the difference between
1375 the joint distribution of X and Y , and the product of their marginal distributions. Since the
1376 product of the marginal distributions is the joint distribution for independent variables, we
1377 can think of the mutual information as a measure of the variables' dependence on one another.

1378 The minimum value that $I(X;Y)$ can take is 0. This occurs when the random variables
1379 X and Y are independent. Then we have $H(X|Y) = H(X)$, and $H(Y|X) = H(Y)$, which

according to equation 3.17, gives $I(X;Y) = 0$. We also have that $H(X,Y) = H(X) + H(Y)$ in this case, which according equation 3.19, gives $I(X;Y) = 0$. Finally, we also have $P(X,Y) = P(X)P(Y)$, which leaves us with 1 in the argument for the logarithm in equation 3.20, which again gives $I(X;Y) = 0$.

The mutual information reaches its maximum value when one of the variables X and Y is completely determined by knowing the value of the other. In that case $I(X;Y) = \min\{H(X),H(Y)\}$.

1387 Variation of Information $VI(X,Y)$

The variation of information is another information theoretical quantity based on the mutual information. It is defined as

$$VI(X;Y) = H(X) + H(Y) - 2I(X;Y) \quad (3.22)$$

We can rewrite this as the summation of two positive quantities

$$VI(X;Y) = [H(X) - I(X;Y)] + [H(Y) - I(X;Y)] \quad (3.23)$$

In English, the variation of information is the summation of the uncertainty in the random variables X and Y excluding the uncertainty shared by those variables.

This measure will become more relevant when we go on to talk about clusterings because $VI(X;Y)$ forms a metric on the space of clusterings.

1392 Measuring entropies & mutual information

In practice, we measured the mutual information between spike counts using Python and the python package `pyitlib`. We used the PT-bias correction technique to estimate the bias of our measurements when measuring the mutual information between the spike counts of two cells (Treves and Panzeri, 1995).

When measuring the mutual information between clusterings we used Python, but we used the `mutual_info_score`, `adjusted_mutual_info_score`, and `normalized_mutual_info_score` functions from the `sklearn.metrics` part of the `sklearn` package.

3.3. Methods

3.3.5 Network analysis

Correlation networks

In order to analyse functional networks created by the neurons in our ensemble, we measured the total correlation between each pair of neurons. These measurements induced an undirected weighted graph/network between the neurons. The weight of each connection was equal to the total correlation between each pair of neurons.

We followed the same procedure for total correlations 3.3.2, spike count correlations, and signal correlations 3.3.3.

Rectified correlations

At the time of writing, the community detection method outlined in (Humphries et al., 2019) could only be applied to networks with positively weighted connections. But many neuron pairs were negatively correlated. To apply the community detection method, we *rectified* the network, by setting all the negative weights to zero.

We also looked for structure in the network created by negative correlations by reversing the signs of the correlations, and rectifying these correlations before applying our network analysis.

Finally, we used the absolute value of the correlations as the weights for the graph/network. By doing this, we hoped to identify both correlated and anti-correlated functional communities of neurons.

Sparsifying data networks

When creating our correlation networks, we wanted to exclude any correlations that could be judged to exist ‘by chance’. To do this, we measured the 5th and 95th percentile of the shuffled correlations (see section 3.3.2) for the given mouse and time bin width. We then set all the data correlations between these two values to 0. This excluded any ‘chance’ correlations from our network, and created a sparser network. This allowed us to make use of the ‘sparse weighted configuration model’ as described in section 3.3.5.

Communities

Given some network represented by an adjacency matrix \mathbf{A} , a community within that network is defined as a collection of nodes where the number of connections within these nodes

1430 is higher than the expected number of connections between these nodes. In order to quan-
1431 tify the ‘expected’ number of connections, we need a model of expected networks. This is
1432 analogous to a ‘null model’ in traditional hypothesis testing. We test the hypothesis that our
1433 data network departs from the null network model to a statistically significant degree. For
1434 undirected unweighted networks, the canonical model of a null network is the configuration
1435 model (Fosdick et al., 2016). Since we are working with weighted sparse networks, we used
1436 more suitable null models, described below.

1437 **Weighted configuration model**

1438 The *weighted configuration model* is a canonical null network model for weighted networks.
1439 Given some data network, the weighted configuration model null network will preserve the
1440 degree sequence and weight sequence of each node in the data network. But the edges will
1441 be distributed randomly (Fosdick et al., 2016). Any structure in the data network beyond
1442 its degree sequence and weight sequence will not be captured in the weighted configuration
1443 model. So, this model can be used in testing the hypothesis that this extra structure exists.

1444 **Sparse weighted configuration model**

1445 The *sparse weighted configuration model* is another null network model. Similar in nature to
1446 the weighted configuration model (see section 3.3.5), but the sparsity of the data network is
1447 preserved in the null network. This is achieved by sampling from a probability distribution
1448 for the creation or non-creation of each possible connection, then distributing the weight of
1449 the data network randomly in this sparse network (Humphries et al., 2019). This is the null
1450 network that we used when searching for additional structure in our data networks.

1451 **Spectral rejection**

1452 We made use of the spectral rejection algorithm as outlined in (Humphries et al., 2019). The
1453 spectral rejection algorithm is a method for finding structure in a network not captured by a
1454 supposed null model, if such structure exists.

To describe the method, we denote our data network matrix \mathbf{W} , we denote the expected
network of our null network model as $\langle \mathbf{P} \rangle$. Then the departure of our data network from the
null network can be described by the matrix

$$\mathbf{B} = \mathbf{W} - \langle \mathbf{P} \rangle \quad (3.24)$$

3.3. Methods

1455 a common choice for $\langle \mathbf{P} \rangle$ in community detection is the ‘configuration model’ (Fosdick et
1456 al., 2016; Humphries, 2011). The matrix \mathbf{B} is often called the configuration matrix, in this
1457 context we will use the term ‘deviation matrix’ as it captures the deviation of \mathbf{W} from the
1458 null model.

1459 To test for structure in the network represented by \mathbf{W} , we examine the eigenspectrum of \mathbf{B}
1460 and compare it to the eigenspectrum of our null model. Firstly, note that since our data model
1461 doesn’t allow self loops, and is not directed, the matrix representing the network will be
1462 symmetric and positive semi-definite, and will therefore be invertible with real eigenvalues.
1463 We selected a null model with the same characteristics.

1464 To find the eigenspectrum of the null model, we generated N samples from our null
1465 model P_1, \dots, P_N , and we measured their deviation matrices B_1, \dots, B_N . We then calculated
1466 the eigenspectrum of each of those samples. We calculated the upper bound of the null model
1467 eigenspectrum by taking the mean of the largest eigenvalues of B_1, \dots, B_N . We calculated a
1468 lower bound on the null model eigenspectrum by taking the mean of the smallest eigenvalues
1469 of B_1, \dots, B_N .

1470 We then calculated the eigenspectrum of \mathbf{B} , our data network deviation matrix. If any of
1471 those eigenvalues lay outside of the upper or lower bounds of the null model eigenspectrum,
1472 this is evidence of additional structure not captured by the null model. If we chose the sparse
1473 weighted configuration model (see section 3.3.5) as our null network model, then eigenvalues
1474 lying below the lower bound indicate k -partite structure in the network. For example, if one
1475 eigenvalue lay below the lower bound, this would indicate some bipartite structure in the data
1476 network. If any eigenvalues lay above the upper bound of the null model eigenspectrum, this
1477 is evidence of community structure in the data network. For example, one eigenvalue of \mathbf{B}
1478 lying above the upper bound of the null model eigenspectrum indicates the presence of two
1479 communities in the network (Humphries, 2011).

1480 Node rejection

1481 If there are d data eigenvalues lying outside of the null network eigenspectrum, the d eigen-
1482 vectors corresponding to these eigenvalues will form a vector space. If we project the nodes
1483 of our network into this vector space, by projecting either rows or columns of the data ma-
1484 trix, we can see how strongly each node contributes to the vector space. Nodes that contribute
1485 strongly to the additional structure will project far away from the origin, nodes that do not
1486 contribute to the additional structure will project close to the origin. We want to use this
1487 information to discard those nodes that do not contribute.

1488 We can test whether a node projects *far* away from the origin or *close* to the origin
 1489 using the eigenvalues and eigenvectors of B_1, \dots, B_N . The j th eigenvector and eigenvalue
 1490 of B_i gives a value for a null network's projection into the j th dimension of the additional
 1491 structure vector space. The matrices B_1, \dots, B_N give N projections into that dimension.
 1492 These projections are a distribution of the null networks' projections. If the data node's
 1493 projection exceeds that of the null network projections this node is judged to project *far* from
 1494 the origin, and therefore contribute to the additional structure. Otherwise, the node is judged
 1495 to project *close* to the origin, and is therefore rejected (Humphries et al., 2019).

1496 **Community detection**

1497 Another application for this d dimensional space is community detection. We first project
 1498 all of the nodes into this d -dimensional space, then perform the clustering in this space. The
 1499 clustering and community detection procedure is described in (Humphries, 2011).

1500 In practice, the procedure is carried out n times (we chose $n = 100$ times), this returns n
 1501 clusterings. We resolve these n clusterings to one final clustering using *consensus clustering*.
 1502 We used the consensus clustering method that uses an explicit null model for the consensus
 1503 matrix, as outlined in (Humphries et al., 2019).

1504 **3.3.6 Clustering Comparison**

A clustering \mathcal{C} is a partition of a set D into sets C_1, C_2, \dots, C_K , called clusters, that satisfy the following for all $k, l \in \{1, \dots, K\}$:

$$C_k \cap C_l = \emptyset \quad (3.25)$$

$$\bigcup_{k=1}^K C_k = D \quad (3.26)$$

1505 If we consider two clusterings, \mathcal{C} with clusters C_1, C_2, \dots, C_K and \mathcal{C}' with clusters
 1506 C'_1, C'_2, \dots, C'_K . There are a number of measurements we can use to compare \mathcal{C} and \mathcal{C}' . In
 1507 the following, the number of elements in D is denoted by n , and the number of elements in
 1508 cluster C_k is n_k .

1509 **Adjusted Rand Index**

1510 The *adjusted Rand Index* is a normalised similarity measure for clusterings based on pair
 1511 counting.

3.3. Methods

If we consider the clusterings \mathcal{C} and \mathcal{C}' , and denote

- the number of pairs in the same cluster in \mathcal{C} and \mathcal{C}' by N_{11}

- the number of pairs in different clusters in \mathcal{C} and \mathcal{C}' by N_{00}

- the number of pairs in the same cluster in \mathcal{C} and different clusters in \mathcal{C}' by N_{10}

- the number of pairs in different clusters in \mathcal{C} and the same cluster in \mathcal{C}' by N_{01}

then the *Rand Index* is defined as

$$RI = \frac{N_{11} + N_{00}}{N_{11} + N_{00} + N_{10} + N_{01}} = \frac{N_{11} + N_{00}}{\binom{n}{2}} \quad (3.27)$$

The Rand Index is 1 when the clusterings are identical, and 0 when the clusterings are com-

pletely different.

The *adjusted Rand Index* intends on correcting the Rand Index for chance matching pairs.

This is defined as

$$ARI = \frac{2(N_{00}N_{11} - N_{01}N_{10})}{(N_{00} + N_{01})(N_{01} + N_{11}) + (N_{00} + N_{10})(N_{10} + N_{11})} \quad (3.28)$$

The adjusted Rand Index is 1 when the clusterings are identical, and 0 when the Rand Index

is equal to its expected value.

1521 Clustering as random variables

If we take any random element of D , the probability that this element is in cluster C_k of clustering \mathcal{C} is

$$P(K = k) = \frac{n_k}{n} \quad (3.29)$$

this defines a probability distribution, which makes the clustering a random variable. Any

clustering can be considered as a random variable this way.

This means that we can measure any of the information theoretic quantities defined in section 3.3.4 with respect to clusterings. For example, the entropy of a clustering is

$$H(\mathcal{C}) = - \sum_{k=1}^K \frac{n_k}{n} \log \frac{n_k}{n} \quad (3.30)$$

If we have two clusterings, the joint probability distribution of these clusterings is defined as

$$P(K = k, K' = k') = \frac{|C_k \cap C'_{k'}|}{n} \quad (3.31)$$

- 1524 The joint distribution allows us to define the mutual information between two clusterings,
1525 $I(\mathcal{C}; \mathcal{C}')$ (Meilă, 2007).

1526 **Information based similarity measures**

The mutual information between two clusterings is a similarity measure, with $I(\mathcal{C}; \mathcal{C}') = 0$ if \mathcal{C} and \mathcal{C}' are completely different, and $I(\mathcal{C}; \mathcal{C}') = H(\mathcal{C}) = H(\mathcal{C}')$ if \mathcal{C} and \mathcal{C}' are identical. This can be normalised in a number of different ways to make more similarity measures (Vinh, Epps, and Bailey, 2010)

$$NMI_{joint} = \frac{I(\mathcal{C}; \mathcal{C}')}{H(\mathcal{C}, \mathcal{C}')} \quad (3.32)$$

$$NMI_{max} = \frac{I(\mathcal{C}; \mathcal{C}')}{\max\{H(\mathcal{C}), H(\mathcal{C}')\}} \quad (3.33)$$

$$NMI_{sum} = \frac{2I(\mathcal{C}; \mathcal{C}')}{H(\mathcal{C}) + H(\mathcal{C}')} \quad (3.34)$$

$$NMI_{sqrt} = \frac{I(\mathcal{C}; \mathcal{C}')}{\sqrt{H(\mathcal{C})H(\mathcal{C}')}} \quad (3.35)$$

$$NMI_{min} = \frac{I(\mathcal{C}; \mathcal{C}')}{\min\{H(\mathcal{C}), H(\mathcal{C}')\}} \quad (3.36)$$

We can control for chance similarities between the two clusterings by measuring the *adjusted mutual information* between the clusterings. This is defined as

$$AMI_{sum} = \frac{I(\mathcal{C}; \mathcal{C}') - E\{I(\mathcal{C}; \mathcal{C}')\}}{\frac{1}{2}[H(\mathcal{C}) + H(\mathcal{C}')] - E\{I(\mathcal{C}; \mathcal{C}')\}} \quad (3.37)$$

- 1527 The first term in the denominator, taking the average of the marginal entropies, can be re-
1528 placed by taking the maximum, minimum, or the geometric mean (Vinh, Epps, and Bailey,
1529 2010).

3.3. Methods

1530 Information based metrics

The variation of information between two clusterings $VI(\mathcal{C}; \mathcal{C}')$ (see section 3.3.4) is a metric on the space of clusterings (Meilă, 2007). That is,

$$VI(\mathcal{C}; \mathcal{C}') \geq 0 \quad (3.38)$$

$$VI(\mathcal{C}; \mathcal{C}') = 0 \iff \mathcal{C} = \mathcal{C}' \quad (3.39)$$

$$VI(\mathcal{C}; \mathcal{C}') = VI(\mathcal{C}'; \mathcal{C}) \quad (3.40)$$

$$VI(\mathcal{C}; \mathcal{C}'') \leq VI(\mathcal{C}; \mathcal{C}') + VI(\mathcal{C}'; \mathcal{C}'') \quad (3.41)$$

Another metric is the *information distance* (Vinh, Epps, and Bailey, 2010)

$$D_{max} = \max\{H(\mathcal{C}), H(\mathcal{C}')\} - I(\mathcal{C}; \mathcal{C}') \quad (3.42)$$

Both of these can be normalised

$$NVI(\mathcal{C}; \mathcal{C}') = 1 - \frac{I(\mathcal{C}; \mathcal{C}')}{H(\mathcal{C}, \mathcal{C}')} \quad (3.43)$$

$$d_{max} = 1 - \frac{I(\mathcal{C}; \mathcal{C}')}{\max\{H(\mathcal{C}), H(\mathcal{C}')\}} \quad (3.44)$$

1531 Comparing detected communities and anatomical divisions

1532 In order to quantify the difference or similarity between the communities detected in our cor-
 1533 relation network and the anatomical classification of the cells in that network, we considered
 1534 the communities and the anatomical regions as clusters in two different clusterings, \mathcal{C}_{comm}
 1535 and \mathcal{C}_{anat} , respectively. We then measured the similarity between the clusterings using the
 1536 mutual information, the adjusted mutual information, and the normalised mutual informa-
 1537 tion. We measured the difference between, or the distance between, the clusterings using the
 1538 variation of information, the normalised variation of information, and the normalised infor-
 1539 mation distance. We also measured the difference between the clusterings using the adjusted
 1540 Rand Index, just to use a non-information based measure.

1541 We took all of these measures for communities detected using different time bin widths.

1542 This gave us an idea of the effect of time bin width on correlation networks in neural ensem-
 1543 bles relative to anatomical regions within those ensembles.

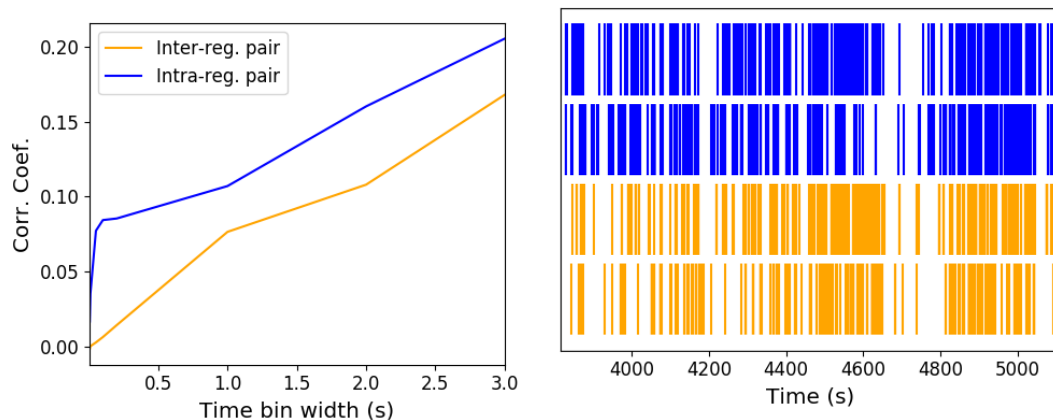
1544 3.4 Results

1545 Note that in the following text, we refer to the correlation coefficient between two sequences
 1546 of spike counts from two different cells as the *total correlation*. We refer to the correlation
 1547 between spike counts in response to a certain stimulus as the *spike count correlation* aka
 1548 *noise correlation*, and we refer to the correlation between mean or expected responses to
 1549 different stimuli as the *signal correlation* (Cohen and Kohn, 2011).

1550 The nine different brain regions from which we had data were the caudate putamen (CP),
 1551 frontal motor cortex (FrMoCtx), hippocampus (HPF), lateral septum (LS), midbrain (MB),
 1552 primary visual cortex (V1), superior colliculus (SC), somatomotor cortex (SomMoCtx), and
 1553 thalamus (TH).

1554 3.4.1 Average correlation size increases with increasing time bin width

1555 First we inspected the affect of time bin width on total correlations. We know that using short
 1556 time bins results in artificially small correlation measurements (Cohen and Kohn, 2011), so
 1557 we expected to see an increase in correlation amplitude with increasing time bin width. That
 1558 is exactly what we observed. Taking 50 cells at random, we calculated the total correla-
 1559 tion between every possible pair of these cells, using different time bin widths ranging from
 1560 0.005s to 3s. We found that the longer the time bin width, the greater the correlations (see
 1561 figure 3.4a).



(A) Correlation coefficient as a function of bin width. (B) Raster plots for the four cells making up our example pairs.

FIGURE 3.3: (A) An example of the correlation coefficients between two different pairs of cells, one where both cells are in the same brain region (intra-regional pair), and one where both cells are in different brain regions (inter-regional pair). The correlation coefficients have been measured using different time bin widths, ranging from 5ms to 3s. Note the increasing amplitude of the correlations with increasing bin width. (B) A raster plot showing the spike times of each pair of cells.

3.4. Results

1562 We also separated the positively correlated pairs from the negatively correlated pairs
1563 using the mean correlation of each pair across all bin widths (see section 3.3.2). We found
1564 that the positively correlated pairs become more positively correlated with increasing time bin
1565 width, and the negatively correlated pairs become more negatively correlated with increasing
1566 time bin width (see figures 3.4b and 3.4c).

1567 In figure 3.3a we plot correlations from two example pairs, one pair from within a region,
1568 and one pair between regions. It can be seen that the correlation coefficient increases with
1569 bin width. The correlations can be observed by eye in the raster plot for these cells in figure
1570 3.3b.

1571 When taking the mean across all pairs, the positively correlated pairs dominate in terms
1572 of both number of pairs, and amplitude of correlations. Therefore the mean across all pairs
1573 is positive.

1574 These results were observed in each of the three mouse subjects from which we had data.

1575 3.4.2 Goodness-of-fit for Poisson and Gaussian distributions across increasing 1576 time bin widths

1577 We wanted to investigate if the width of the time bin used to bin spike times into spike counts
1578 had an effect on the distribution of spike counts. We used the χ^2 statistic as a goodness-of-fit
1579 measure for Poisson and Gaussian (normal) distributions to the spike count of 100 randomly
1580 chosen neurons for a number of bin widths ranging from 0.01s to 4s. For the χ^2 statistic, the
1581 higher the value, the worse the fit.

1582 We expected a Poisson distribution to be a better fit for shorter time bin widths because
1583 spike counts must be non-negative, therefore any distribution of spike counts with mass dis-
1584 tributed at or close to 0 will be skewed. The distribution of spike counts is more likely to be
1585 distributed close to 0 when the time bin widths used to bin spike times into spike counts are
1586 small relative to the amount of time it takes for a neuron to fire an action potential ($\sim 1\text{ms}$ in
1587 the case of non-burst firing neurons).

1588 We expected a Gaussian distribution to be a better fit for longer time bin widths, because
1589 a Poisson distribution with a large rate is well approximated by a Gaussian distribution with
1590 mean and variance equal to the Poisson rate. Therefore, a Gaussian distribution would ap-
1591 proximate the mean of a collection of large spike counts, and have more flexibility than a
1592 Poisson distribution to fit the variance.

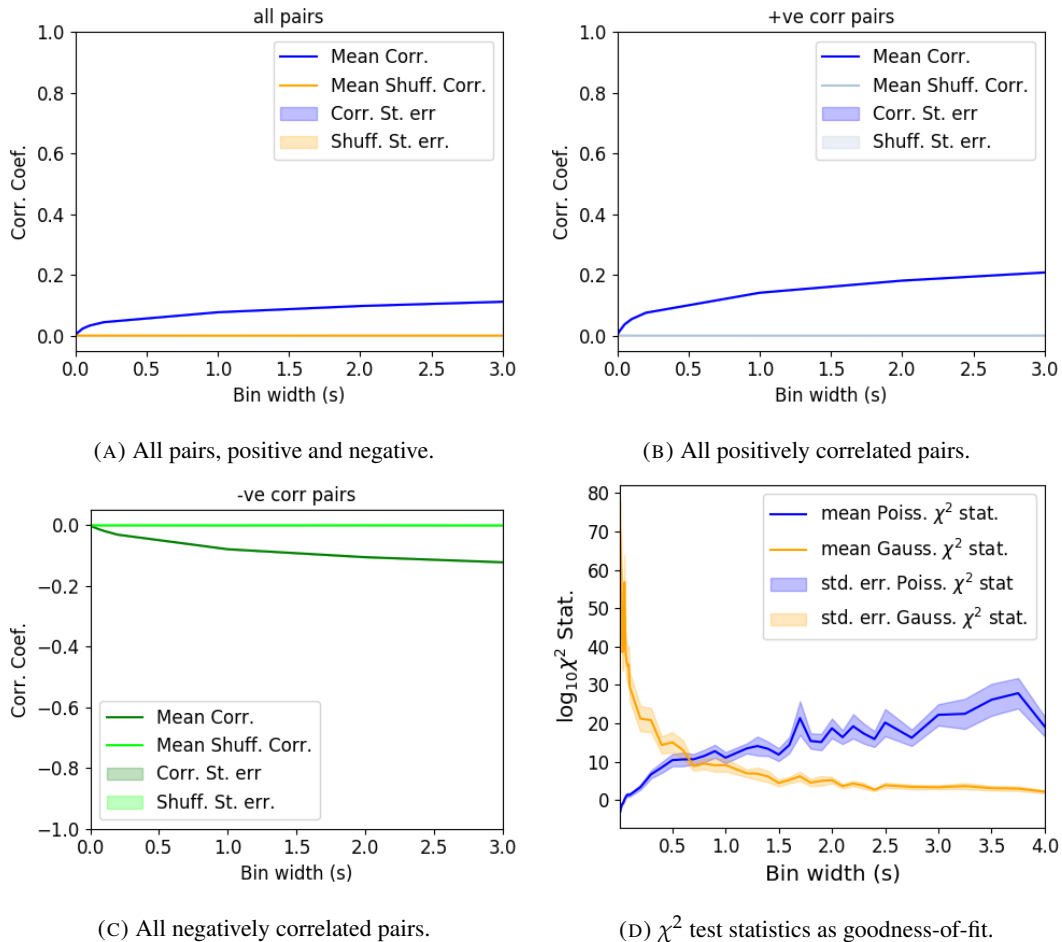


FIGURE 3.4: Mean correlation coefficients measured from pairs of 50 randomly chosen neurons. (A) All possible pairs, (B) positively correlated pairs, and (C) negatively correlated pairs. (D) Mean and standard error of χ^2 test statistics for Poisson and Gaussian distributions fitted to neuron spike counts.

3.4. Results

We found that that a Poisson distribution is the best fit for shorter time bins less than 0.7s in length. Then a Gaussian distribution is a better fit for time bins greater than 0.7s in length (see figure 3.4d).

3.4.3 Differences between and inter- and intra- regional correlations decrease with increasing bin width

We investigated the differences in distribution between inter-regional correlations, i.e. correlations between neurons in different brain regions, and intra-regional correlations, i.e. correlations between neurons in the same brain region.

Firstly, we investigated these quantities for all possible pairs of ~ 500 neurons taken from across all the 9 brain regions from which we had data. We distributed these neurons as evenly as possible across all of the regions, so that cells from one region would not dominate our data. We observed that the mean intra-regional correlations were always higher than the mean inter-regional correlations for every value of time bin width used. We also observed that as the time bin width increased these mean correlations increased and the difference between the mean inter-regional and intra-regional correlations grew (see figure 3.5 (Left)).

Stringer et al. (2019) had a similar finding using the same data. They used only one value for the time bin width, 1.2s. Using this time bin width to bin spike times and measure total correlations, they found that the mean ‘within-region’ correlations were always greater than the ‘out-of-region’ correlations (Stringer et al., 2019). The figure from their paper showing this result can be seen in figure 3.5 (Right).

Examples of the correlations of one intra-regional pair and one inter-regional pair can be seen in figure 3.3.

Secondly, we separated those pairs into intra-regional and inter-regional groups. We noted that the mean intra-regional correlations (coloured dots in figures 3.6a and 3.6b) for a given region tended to be higher than the mean inter-regional correlations (black dots in figures 3.6a and 3.6b) involving cells from that region. However, in contrast with our previous result, we noted that the difference between the mean intra-regional correlations and most highly correlated inter-regional correlations reduced as we increased the time bin width (see figures 3.6a and 3.6b). This shows that the mean correlations showin in figure 3.5 are not distributed evenly across all region pair combinations.

Finally, to see these regional mean correlations in a bit more detail, to examine the individual pair combinations in particular, we displayed these data in a matrix of mean correlations (see figure 3.7), showing the mean intra-regional correlations on the main diagonal, and

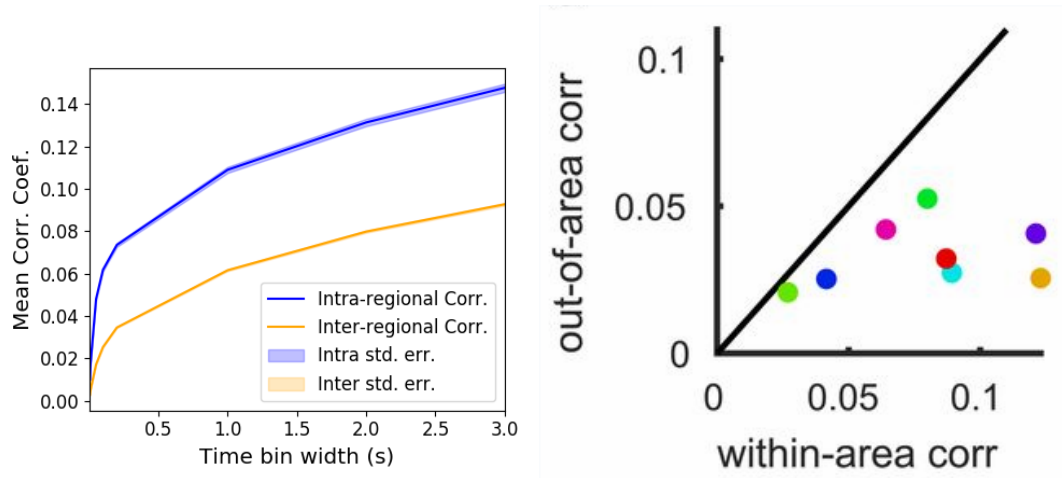


FIGURE 3.5: (Left) The mean intra-region and inter-region correlations using all possible pairs of ~ 500 neurons, spread across 9 different brain regions. (Right) Courtesy of Stringer et al. (2019), mean inter-regional (out-of-area) correlation coefficients vs mean intra-regional (within-area) correlation coefficients for a bin width of 1.2s. Note that the intra-regional coefficients are higher in each case.

1626 the mean inter-regional correlations off diagonal. Comparing a version of this figure created
 1627 using a short time bin width of 5ms (figure 3.7a) and a version using a longer time bin width
 1628 of 1s (figure 3.7b) we observed that the mean intra-regional correlations are always relatively
 1629 high in comparison to the mean inter-regional correlations, but the mean correlations in some
 1630 inter-regional pairs are relatively much higher when using the longer time bin width.

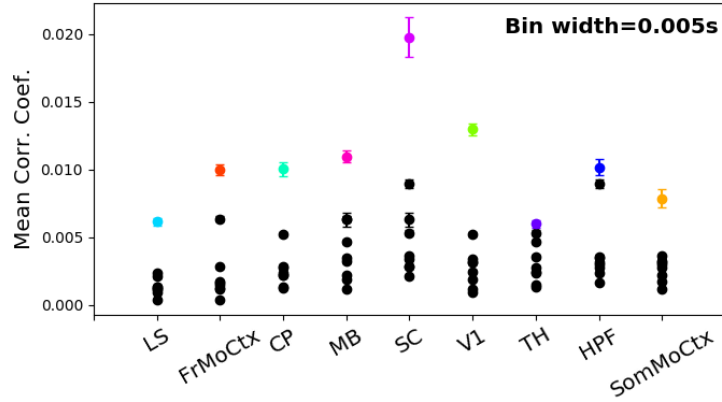
1631 This could indicate information being processed quickly at a local or within-region level,
 1632 and the local representations of this information spreading between regions at longer timescales.

1633 These results were consistent across the three mouse subjects. But, the relative magni-
 1634 tudes of the mean intra-regional and inter-regional correlations were not consistent. For ex-
 1635 ample, the region with the highest mean intra-regional correlations when using 1s bin widths
 1636 for subject one is the superior colliculus (SC), but for subject two it is the midbrain (MB).

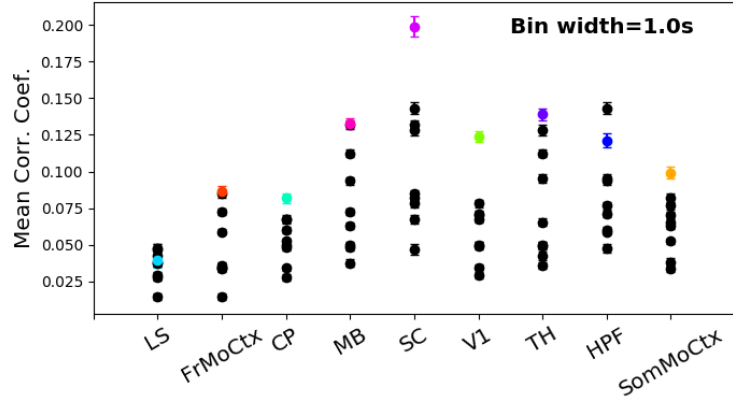
1637 3.4.4 Connected and divided structure in correlation based networks reduces 1638 in dimension with increasing bin width

1639 We used the correlation measurements to create weighted undirected graphs/networks where
 1640 each node represents a neuron, and the weight of each edge is the pairwise correlation be-
 1641 tween those neurons represented by the nodes at either end of that edge. We aimed to find
 1642 communities of neurons within these networks, and compare the structure of these commu-
 1643 nities to the anatomical division of those neurons. The first step of this process involved
 1644 applying the ‘spectral rejection’ technique developed by Humphries et al (2019) (Humphries

3.4. Results

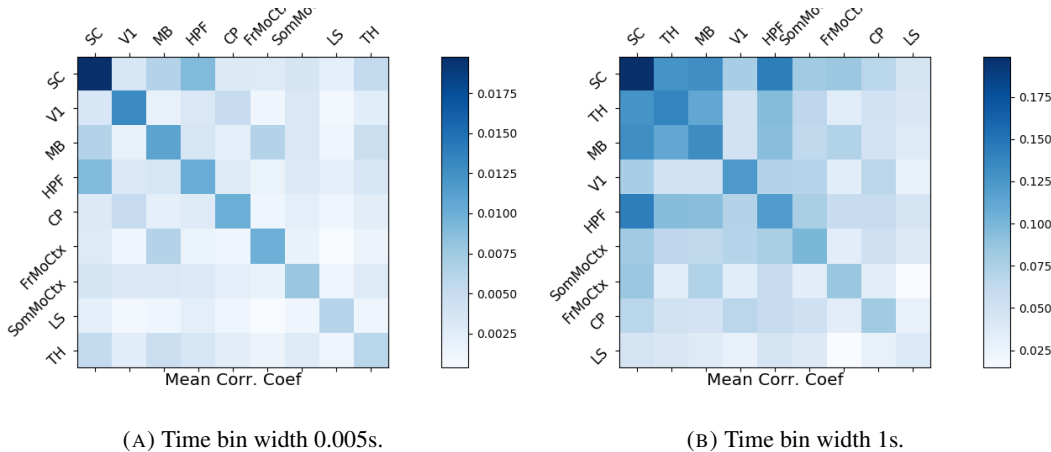


(A) Mean inter-regional and intra-regional correlations using a time bin width of 5ms.



(B) Mean inter-regional and intra-regional correlations using a time bin width of 1s.

FIGURE 3.6: The mean intra-regional correlations (coloured dots) and mean inter-regional correlations (black dots) for a given region, indicated on the x-axis, for different time bin widths. Each black dot represents the mean inter-regional correlations between the region indicated on the x-axis and one other region. (A) shows these measurements when we used a time bin width of 5ms. (B) shows these measurements when we used a time bin width of 1s. Note that the difference between the mean inter-regional correlations and mean intra-regional correlations is smaller for 1s bins.



(A) Time bin width 0.005s.

(B) Time bin width 1s.

FIGURE 3.7: Mean inter-regional (main diagonal) and intra-regional (off diagonal) correlation coefficients. (A) Shows these measurements when spike times were binned using 5ms time bins. (B) Shows the same, using 1s time bins. Note that the matrices are ordered according to the main diagonal values, therefore the ordering is different in each subfigure.

et al., 2019). This technique compares our data network to a chosen null network model, and finds any additional structure in the data network beyond that which is captured in the null network model (if there is any such structure).

By comparing the eigenspectrum of the data network to the eigenspectrum of many samples from the null network model, this technique allows us to estimate the dimensionality of the additional structure in the data network, and gives us a basis for that vector space. It also divides the additional structure into connected structure, and k -partite (or divided) structure. For example, if our algorithm found two dimensions of additional connected structure, and one dimension of additional divided structure. We might expect to find three communities, that is groups more strongly connected within group than without, and we might expect to find bi-partite structure, that is two sets that are more strongly connected between groups than within groups.

The technique also finds which nodes contribute to this additional structure, and divides our data network into signal and noise networks. The details of spectral rejection and node rejection can be found in sections 3.3.5 and 3.3.5 respectively, and a full overview can be found in (Humphries et al., 2019).

We chose the sparse weighted configuration model (see section 3.3.5) as our null network model. This model matches the sparsity and the total weight of the original network but distributes the weight at random across the sparse network.

We applied the spectral rejection method to our networks based on total correlations using different values for the time bin width. We observed that for smaller time bin widths, our data

3.4. Results

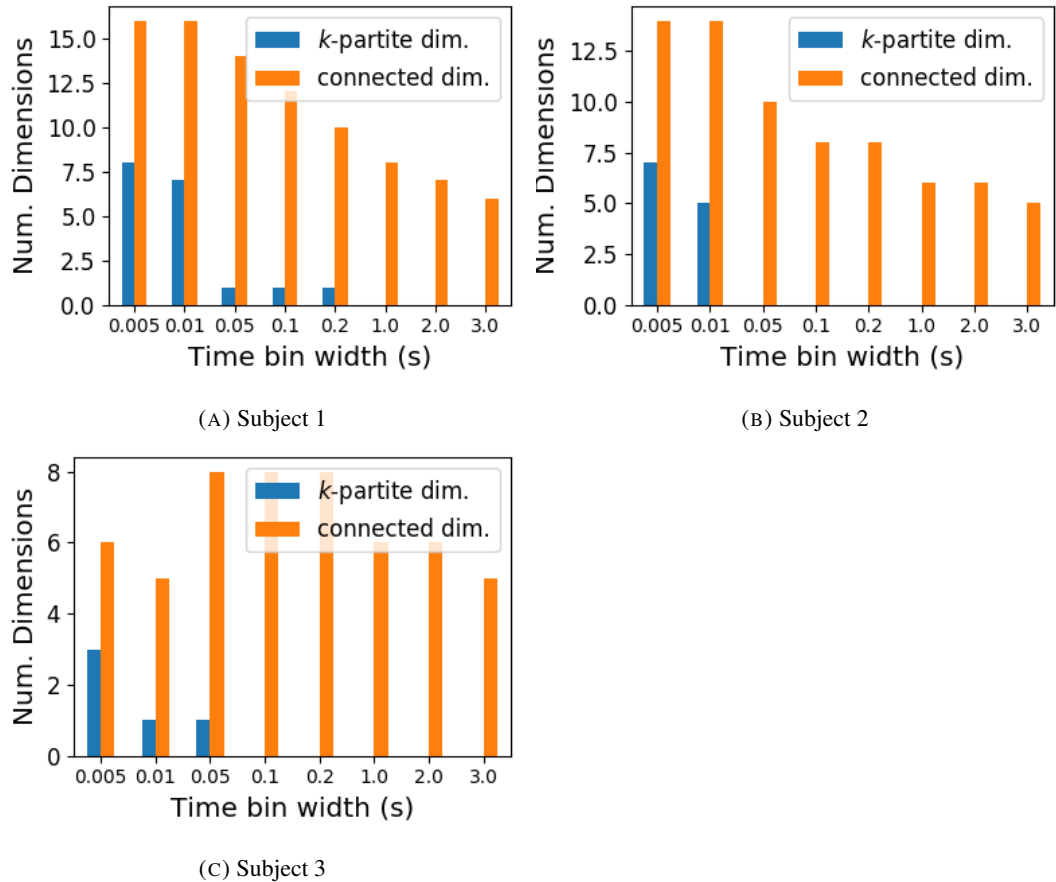


FIGURE 3.8: The number of dimensions in the *k*-partite and connected structure in the correlation based networks beyond the structure captured by a sparse weighted configuration null network model (see section 3.3.5), shown for different time bin widths. Note that the *k*-partite structure disappears for time bin width greater than 200ms for all three subjects. The dimension of the connected structure reduces with increasing bin width for 2 of the 3 subjects (top row).

1666 networks had both k -partite structure, and community structure. As the width of the time bin
1667 increased, we found that the k -partite structure disappeared from our data networks, and the
1668 dimension of the community structure reduced in two of the three mice from which we had
1669 data (see figure 3.8).

1670 **3.4.5 Detecting communities in correlation based networks**

1671 We applied the community detection procedure described in section 3.3.5 to our signal net-
1672 works for our various time bin widths. We detected a greater number of smaller communities
1673 at shorter time bin widths, and a smaller number of larger communities for longer time bin
1674 widths (see figure 3.9). This was expected after the results found in section 3.4.4. We found
1675 more dimensions of additional structure at shorter time bin widths, therefore we found more
1676 communities at shorter time bin widths.

1677 We also noticed that at short time bin widths the communities detected tended to be
1678 dominated by cells from one region. Whereas communities existing in networks created
1679 using wider time bin widths tended to contain cells from many different brain regions. More
1680 on this in the next section.

1681 **3.4.6 Functional communities resemble anatomical division at short timescales**

1682 In order to quantify the similarity of the communities detected to the anatomical division of
1683 the cells. We treated both the anatomical division and the communities as clusterings of these
1684 cells. We then used measures for quantifying the difference or similarity between clusterings
1685 to quantify the difference or similarity between the detected communities and the anatomical
1686 division. Details of these measures can be found in section 3.3.6 or in (Vinh, Epps, and
1687 Bailey, 2010).

1688 We used two different types of measures for clustering comparison; information based
1689 measures (see section 3.3.6) and pair counting based measures (see section 3.3.6). We include
1690 one example of each in figure 3.10.

1691 The variation of information is the information based measure included in figure 3.10a.
1692 This measure forms a metric on the space of clusterings. The larger the value for the variation
1693 of information, the more different the clusterings.

1694 The adjusted Rand index is the pair counting based measure included in figure 3.10b. In
1695 contrast with the variation of information, the adjusted Rand index is a normalised similarity
1696 measure. The adjusted Rand index takes value 1 when the clusterings are identical, and takes
1697 value 0 when the clusterings are no more similar than chance.

3.4. Results

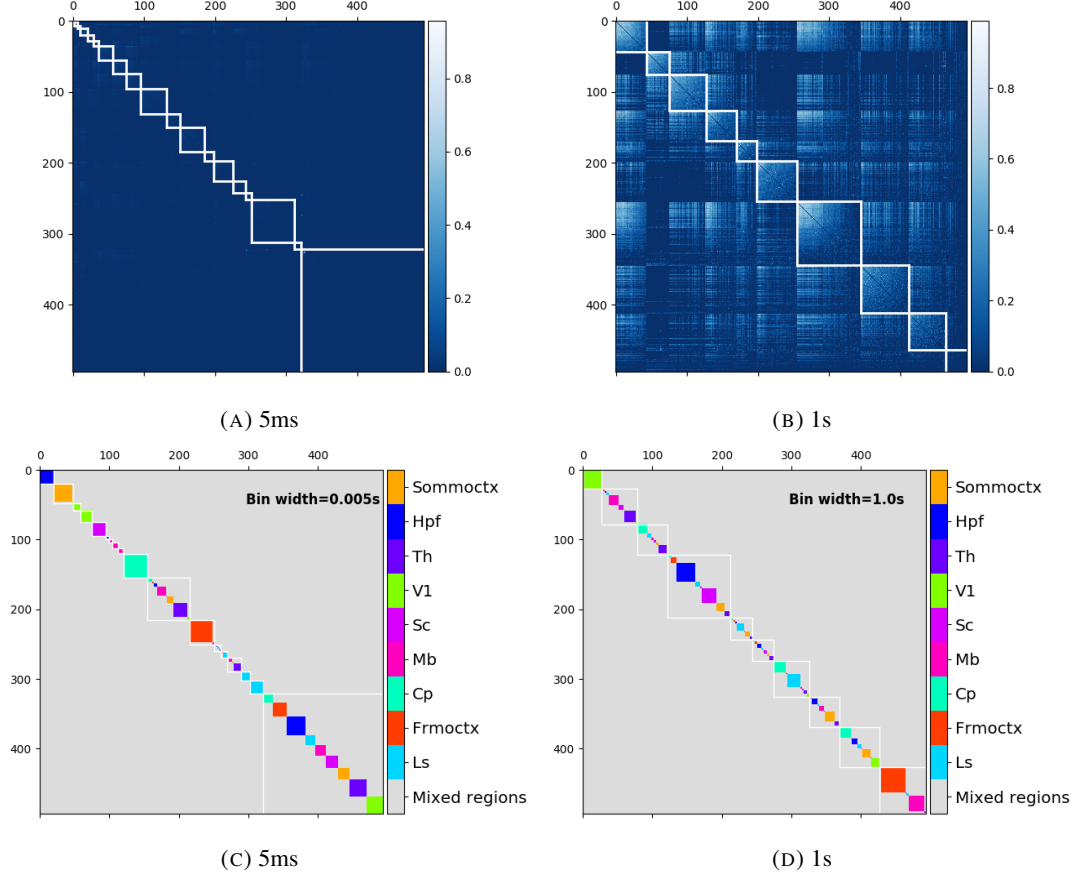
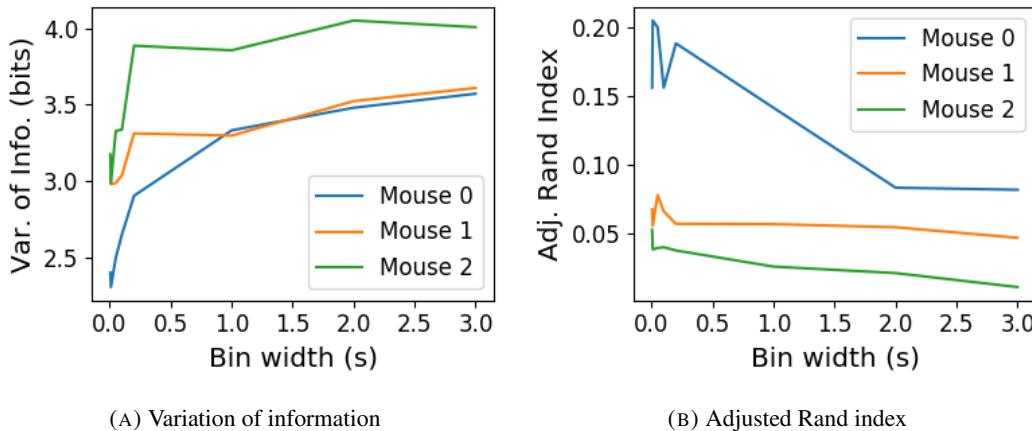


FIGURE 3.9: (A-B) Correlation matrices with detected communities indicated by white lines. Each off main diagonal entry in the matrix represents a pair of neurons. Those entries within a white square indicate that both of those neurons are in the same community as detected by our community detection procedure. Matrices shown are for 5ms and 1s time bin widths respectively. Main diagonal entries were set to 0. (C-D) Matrices showing the anatomical distribution of pairs along with their community membership. Entries where both cells are in the same region are given a colour indicated by the colour bar. Entries where cells are in different regions are given the grey colour also indicated by the colour bar.



(A) Variation of information

(B) Adjusted Rand index

FIGURE 3.10: (A) The variation of information is a measure of distance between clusterings. The distance between the anatomical ‘clustering’ and community detection ‘clustering’ increases with increasing time bin width. (B) The adjusted Rand index is a normalised similarity measure between clusterings. The anatomical and community detection clusterings become less similar as the time bin width increases.

1698 Both measures indicated that the detected communities and the anatomical division of
 1699 the cells were more similar when we used shorter time bins widths (see figure 3.10). This
 1700 indicates that correlated behaviour in neuronal ensembles is more restricted to individual
 1701 brain regions at short timescales (< 250ms), and the correlated activity spreads out across
 1702 brain regions over longer time scales.

1703 3.4.7 Conditional correlations & signal correlations

1704 In light of the excellent research of Stringer et al (2019) showing that spontaneous behaviours
 1705 can drive activity in neuronal ensembles across the visual cortex and midbrain (Stringer et
 1706 al., 2019), we decided to control for the mouse’s behaviour when performing our analyses.
 1707 It is possible that our community detection process may be detecting communities across
 1708 multiple brain regions at longer time scales due to aggregating neuronal activity driven by
 1709 several spontaneous behaviours occurring during the time interval covered by a given time
 1710 bin. A time bin of 1s, for example, could contain a spike count where those spikes were driven
 1711 by different spontaneous behaviours. We aimed to investigate this possibility by applying our
 1712 community detection analysis to conditional correlation measures.

1713 We used the top 500 principal components of a video of the mouse’s face as a measure of
 1714 the mouse’s behaviour (see section 3.2.2). We modelled the spike counts as a linear combi-
 1715 nation of the principal components using linear regression with ElasticNet regularisation (see
 1716 section 3.3.3). Using this model, we quantified the expected spike count given the mouse’s
 1717 behaviour $E[X|Z_1, \dots, Z_{500}]$.

3.4. Results

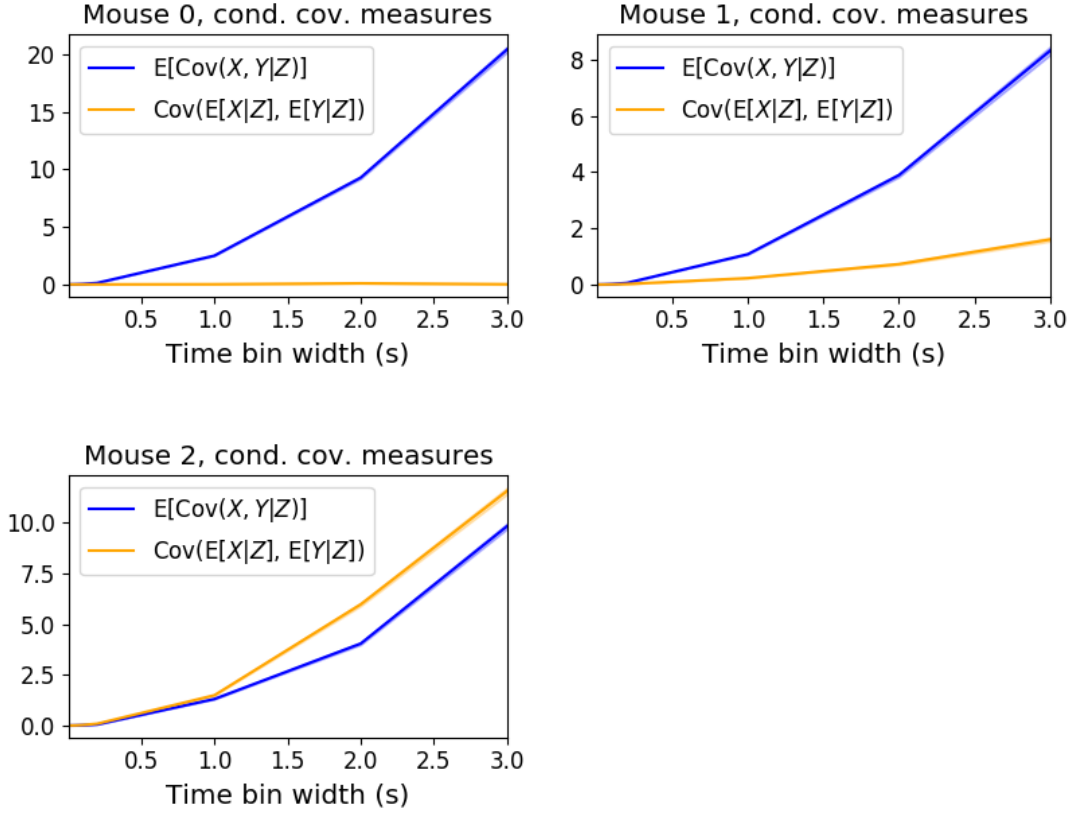


FIGURE 3.11: Comparing the components of the total covariance across different values for the time bin width. We observed a consistent increase in $E[\text{cov}(X, Y|Z)]$ as the time bin width increased. But we saw different trends for $\text{cov}(E[X|Z], E[Y|Z])$ for each mouse.

1718 We used these expected values to measure $\text{cov}(E[X|Z], E[Y|Z])$, and we used that value,
 1719 the covariance $\text{cov}(X, Y)$, and the *law of total covariance* (see section 3.3.3) to measure
 1720 $E[\text{cov}(X, Y|Z)]$. Here X and Y represent spike counts from individual cells, and Z is short-
 1721 hand for the 500 principal components mentioned above. The two components of the co-
 1722 variance, $\text{cov}(E[X|Z], E[Y|Z])$ and $E[\text{cov}(X, Y|Z)]$, represent a ‘signal covariance’ and ex-
 1723 pected value of a ‘spike count covariance’ respectively, analogous to the signal correlation
 1724 and spike count correlation (Cohen and Kohn, 2011).

1725 We examined the means of these components for different values of the time bin width
 1726 (see figure 3.11). We observed a consistent increase in $E[\text{cov}(X, Y|Z)]$ as the time bin width
 1727 increased. But we saw different trends for $\text{cov}(E[X|Z], E[Y|Z])$ for each mouse.

1728 Using $\text{cov}(E[X|Z], E[Y|Z])$ we measured the signal correlation, ρ_{signal} , and using $E[\text{cov}(X, Y|Z)]$
 1729 we measured the event conditional correlation, $\rho_{X,Y|Z}$ (see section 3.3.3 for more details).
 1730 We saw a consistent increase in $\rho_{X,Y|Z}$ as the time bin width increased, this corresponds to
 1731 the result for $E[\text{cov}(X, Y|Z)]$. We observed different trends for ρ_{signal} for each mouse, this

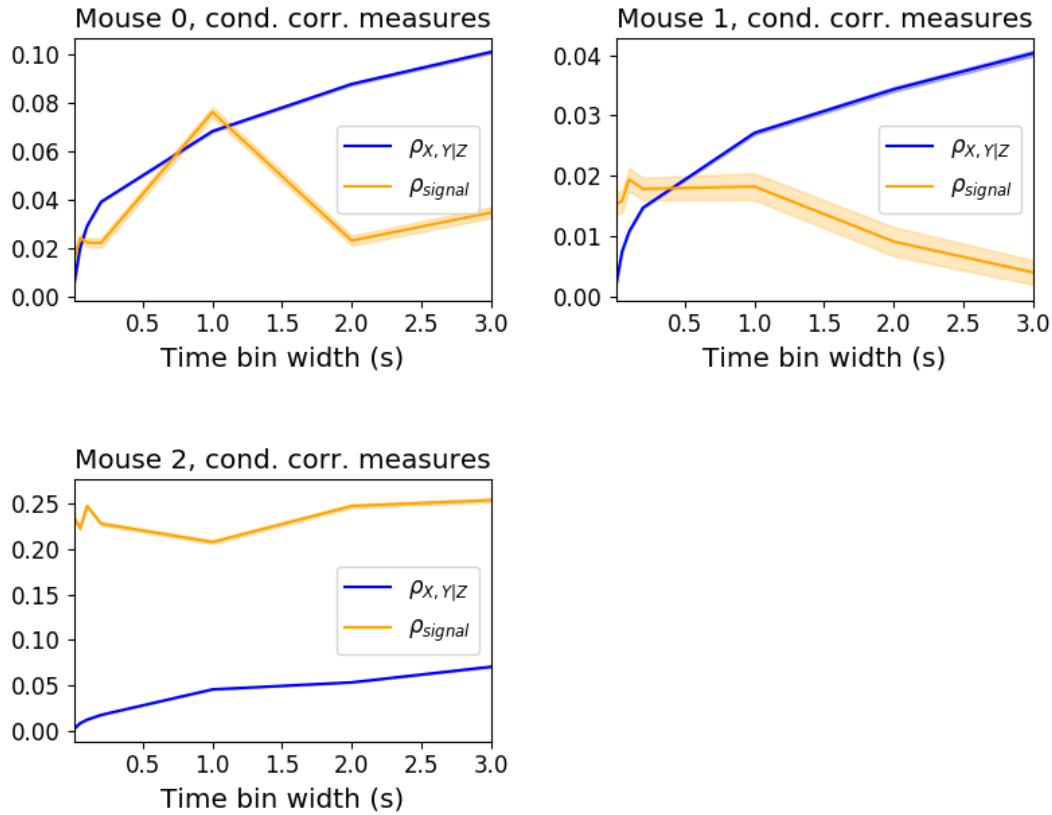


FIGURE 3.12: Comparing the components of the total covariance across different values for the time bin width. We saw a consistent increase in $\rho_{X,Y|Z}$ as the time bin width increased in all three subjects. But we saw different trends in ρ_{signal} for each of the subjects.

1732 corresponds to the result for $\text{cov}(E[X|Z], E[Y|Z])$.

1733 We applied our network noise rejection and community detection process to networks
 1734 based on the spike count correlations $\rho_{X,Y|Z}$ and the signal correlations ρ_{signal} . We noted that
 1735 the community detection on $\rho_{X,Y|Z}$ behaved similarly to the community detection on the total
 1736 correlation. We can see this in figures 3.13a and 3.13b. At very short time bin widths, we
 1737 detect more communities, and those communities often contain cells from one brain region
 1738 only. At longer time bin widths, we detect fewer communities, and those communities tend
 1739 to contain cells from multiple brain regions. When we examine the distance between (or
 1740 similarity between) the anatomical division of the cells, and the detected communities we
 1741 notice that the two clusterings are more similar at shorter time bin widths (see figure 3.14).

1742 When we applied the network noise rejection and community detection process to the
 1743 networks based on the signal correlations ρ_{signal} we found the number of communities we
 1744 detected reduced with increasing time bin width. But the number of communities detected

3.4. Results

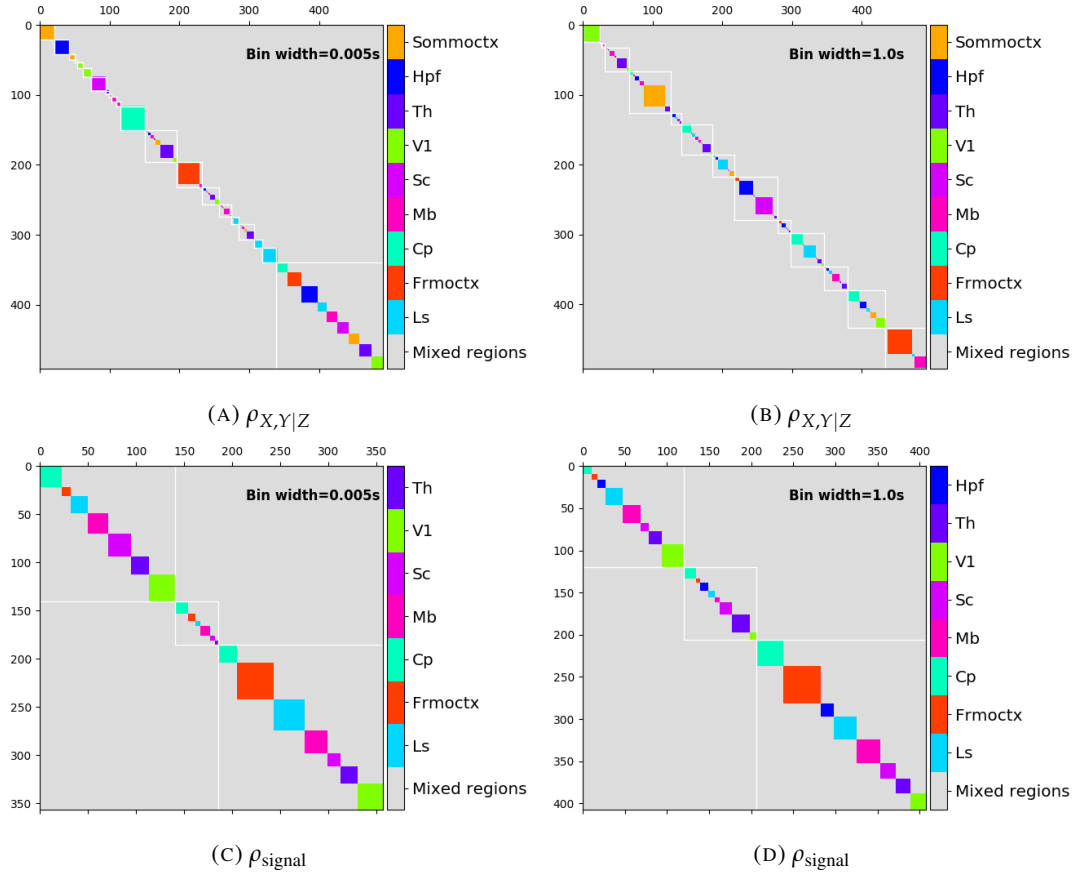


FIGURE 3.13: Matrices showing the regional membership of pairs by colour, and the communities in which those pairs lie. (A-B) Detected communities and regional membership matrix for network based on rectified spike count correlation $\rho_{X,Y|Z}$, using time bin widths of 0.005s and 1s respectively. (C-D) Detected communities and regional membership matrix for network based on rectified signal correlation ρ_{signal} , using time bin widths of 0.005s and 1s respectively.

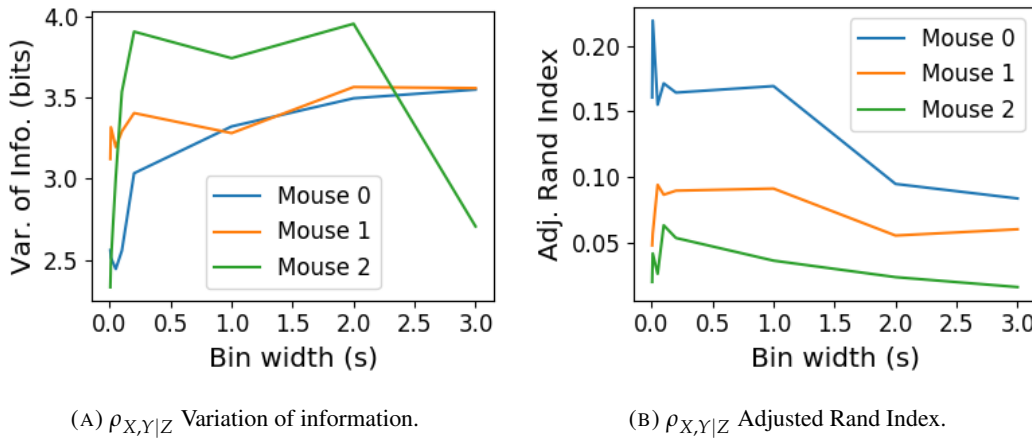
(A) $\rho_{X,Y|Z}$ Variation of information.(B) $\rho_{X,Y|Z}$ Adjusted Rand Index.

FIGURE 3.14: Distance and similarity measures between the anatomical division of the neurons, and the communities detected in the network based on the spike count correlations $\rho_{X,Y|Z}$. (A) The variation of information is a ‘distance’ measure between clusterings. The distance between the anatomical ‘clustering’ and the community clustering increases as the time bin width increases. (B) The adjusted Rand index is a similarity measure between clusterings. The detected communities become less similar to the anatomical division of the cells as the time bin width increases.

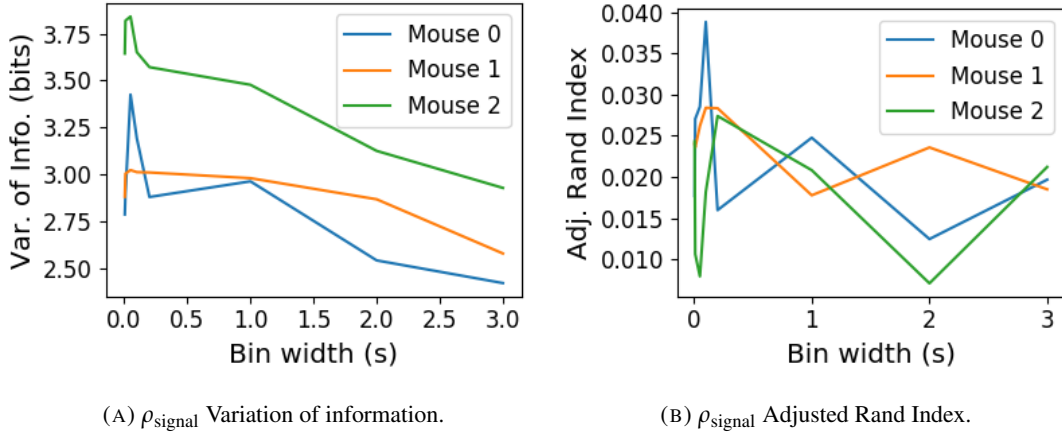
1745 was less than that for the total correlations or the spike count correlations. The commu-
 1746 nities detected always tended to contain cells from multiple regions at both short and long
 1747 timescales (see figures 3.13c and 3.13d). The communities detected bore very little relation
 1748 to the anatomical division of the cells. The adjusted Rand index between the community
 1749 clustering and the anatomical ‘clustering’ is close to zero for every time bin width (see figure
 1750 3.15b). This indicates that the similarity between the clusterings is close to chance. We did
 1751 observe a slight downward trend in the variation of information with increasing bin width
 1752 (see figure 3.15a), but this is more likely due to a decrease in the number of communities
 1753 detected rather than any relationship with anatomy.

1754 We also observed that the network noise rejection process rejected some of the cells
 1755 when applied to the network based on the signal correlations. This means that those cells
 1756 did not contribute to the additional structure of the network beyond that captured by the
 1757 sparse weighted configuration model. This is why the matrices in figures 3.13c and 3.13d are
 1758 smaller than their analogues in figures 3.13a and 3.13b.

1759 3.4.8 Absolute correlations and negative rectified correlations

1760 At the moment, the network noise rejection protocol can only be applied to weighted undi-
 1761 rected graphs with non-negative weights. This meant that we had to rectify our correlated
 1762 networks before applying the network noise rejection and community detection process. We

3.5. Discussion



(A) ρ_{signal} Variation of information.

(B) ρ_{signal} Adjusted Rand Index.

FIGURE 3.15: Distance and similarity measures between the anatomical division of the neurons, and the communities detected in the network based on the signal correlations ρ_{signal} . (A) The variation of information is a ‘distance’ measure between clusterings. The distance between the anatomical ‘clustering’ and the community clustering increases as the time bin width increases. (B) The adjusted Rand index is a similarity measure between clusterings. The detected communities become less similar to the anatomical division of the cells as the time bin width increases.

wanted to investigate what would happen if instead of rectifying the correlations, we used the absolute value, or reversed the signs of the correlations and then rectified.

When we used the absolute value of the correlations, we found very similar results to those shown above for the rectified total correlations and the rectified spike count correlations. We detected more communities using shorter bin widths, and these communities were more similar to the brain’s anatomy than those communities detected using a longer bin width (see figure 3.16). The only exception being that we detected more communities. This could indicate that we detected both positively and negatively correlated communities, but we haven’t done any further investigation so we cannot say for sure.

When we used the sign reversed rectified correlated networks, we tended to find fewer communities. Each community contained cells from many different anatomical regions, at both long and short bin widths (see figures 3.17a, 3.17b, 3.17c, 3.17d). The communities bore little relation to the anatomical distribution of the cells, this can be seen in figure 3.17f, the values close to zero indicate that the similarity between the two clusterings are around chance level. This indicates that there was not much structure in the negatively correlated networks beyond that captured by the sparse weighted configuration model.

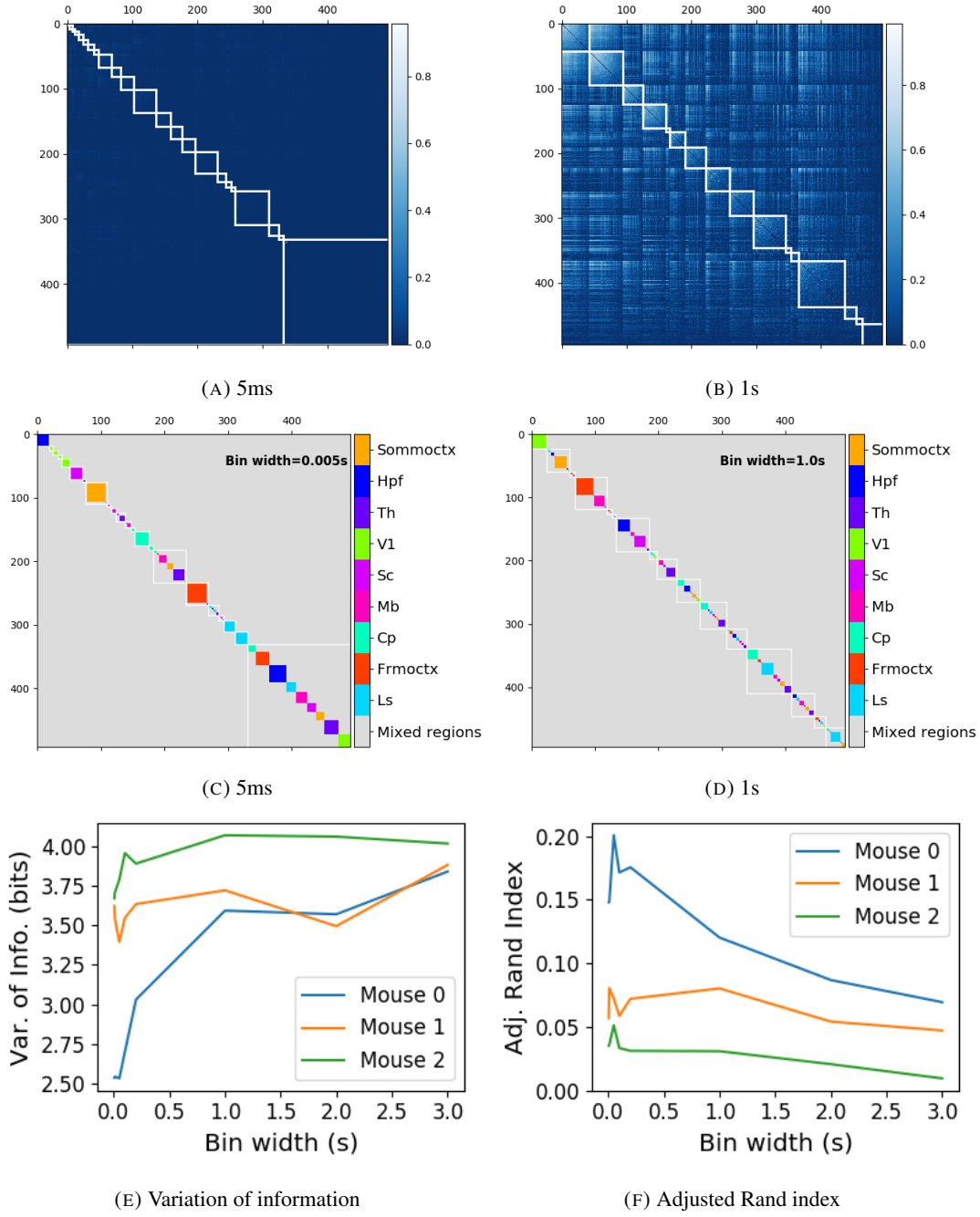


FIGURE 3.16: (A-B) Absolute correlation matrices with detected communities indicated by white lines. These communities are based on the absolute value of the total correlation between each pair of cells. Those entries within a white square indicate that both of those neurons are in the same community. Matrices shown are for 5ms and 1s time bin widths respectively. Main diagonal entries were set to 0. (C-D) Matrices showing the anatomical distribution of pairs along with their community membership. Regional membership is indicated by the colour bar. (E) Variation of information between the anatomical division of the cells, and the detected communities. (F) Adjusted Rand index between the anatomical division, and the detected communities.

3.5. Discussion

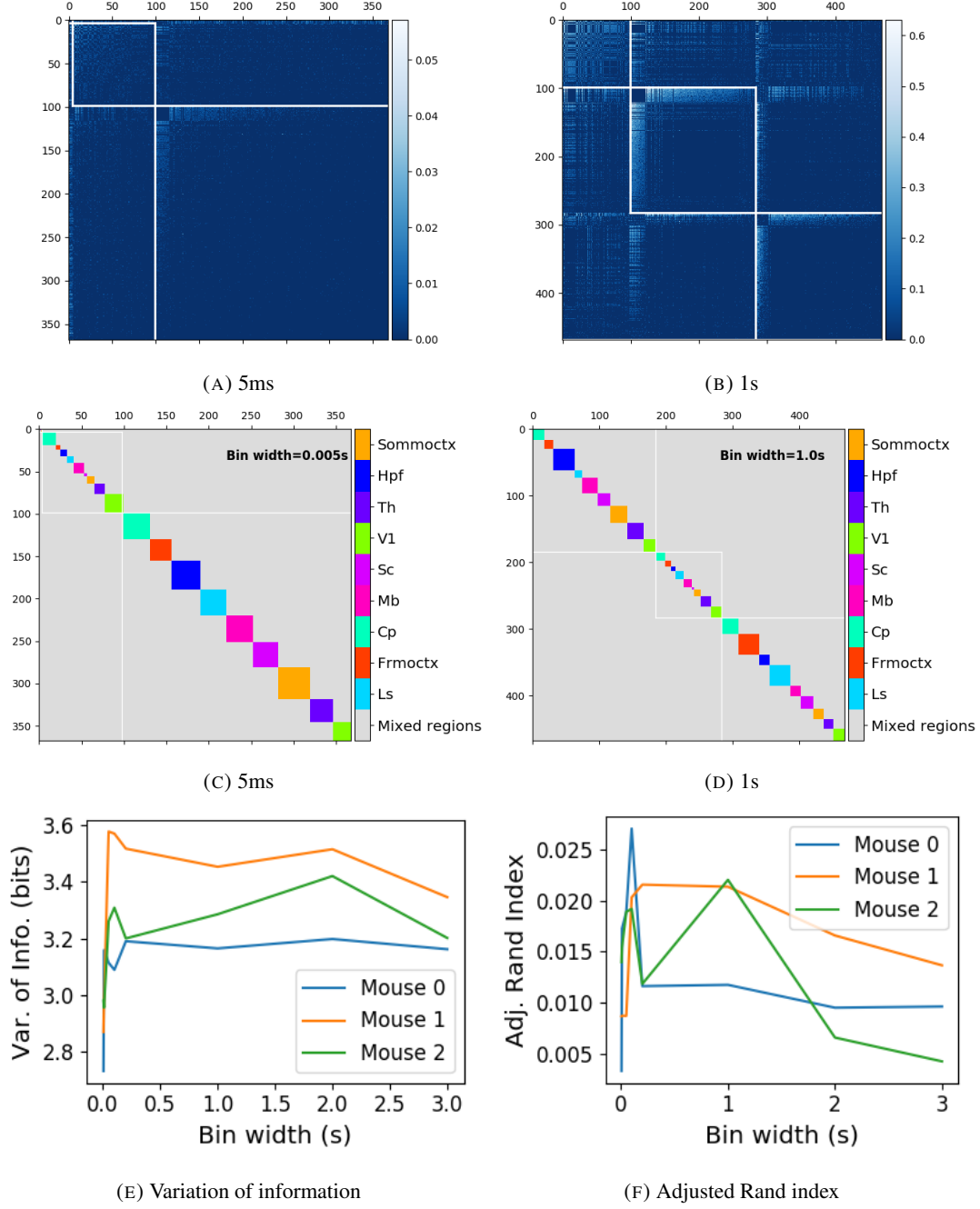


FIGURE 3.17: (A-B) Sign reversed rectified correlation matrices with detected communities indicated by white lines. Those entries within a white square indicate that both of those neurons are in the same community. Matrices shown are for 5ms and 1s time bin widths respectively. Main diagonal entries were set to 0. (C-D) Matrices showing the anatomical distribution of pairs along with their community membership. Regional membership is indicated by the colour bar. (E) Variation of information between the anatomical division of the cells, and the detected communities. (F) Adjusted Rand index between the anatomical division, and the detected communities.

1779 **3.5 Discussion**

1780 It is well established that the brain uses correlated behaviour in neuronal ensembles to repre-
1781 sent the information taken in through sensation (Cohen and Maunsell, 2009; Litwin-Kumar,
1782 Chacron, and Doiron, 2012; deCharms and Merzenich, 1996). However, most studies that
1783 examine the nature of these correlations in-vivo, study an ensemble of cells from only one
1784 or two brain regions (Cohen and Kohn, 2011; Wierzynski et al., 2009; Patterson et al., 2014;
1785 Girard, Hupé, and Bullier, 2001). Furthermore, recent results have shown that behaviour can
1786 drive correlated activity in multiple brain regions, including those not normally associated
1787 with motor control (Stringer et al., 2019; Gründemann et al., 2019; Allen et al., 2019). In this
1788 study, we utilised one of the newly recorded large datasets containing electrophysiological
1789 recordings from multiple brain regions simultaneously. We investigated correlated behaviour
1790 in these different brain regions and we investigated correlated behaviour between neurons in
1791 different regions, during spontaneous behaviour.

1792 A number of studies have found that the timescale of correlated behaviour induced by a
1793 stimulus can be modulated by the stimulus structure and behavioural context. For example,
1794 the spike train correlations between cells in weakly electric fish are modulated by the spa-
1795 tial extent of the stimulus (Litwin-Kumar, Chacron, and Doiron, 2012), and neurons in the
1796 marmoset primary auditory cortex modulate their spike timing (and therefore correlation) in
1797 response to stimulus features without modulating their firing rate (deCharms and Merzenich,
1798 1996). Furthermore, the width of the time bins over which spike counts are measured has
1799 been shown to have an effect on the magnitude of those correlations (Cohen and Kohn, 2011).
1800 Despite this, very little research has been done comparing correlation measures from the same
1801 dataset at different timescales. We investigated this by varying the time bin width used to bin
1802 spike times into spike counts from as short as 5ms up to 3s.

1803 In order to further investigate the effect of these correlations at different timescales, we
1804 regarded our neuronal ensemble as a weighted undirected graph, where each neuron is rep-
1805 resented by a node, and the weight on each edge is the correlation between the neurons
1806 connected by that edge. We then applied a novel clustering method from network science
1807 (Humphries et al., 2019) to identify communities in these networks. Communities in a net-
1808 work graph refer to sets of nodes that are more strongly connected to each other than the
1809 nodes outside of their set. Another way to put this is to say that the nodes in a community
1810 are more strongly connected than *expected*. What connection strength might be expected is
1811 defined by a null network model. We chose a null network model that matched the sparsity

3.5. Discussion

and total strength of our correlation based data networks. So, if two cells were in the same community, those cells were more correlated than would be expected given the correlation strength of their ensemble.

These networks, and the community detection process, were completely agnostic of the anatomical division of the cells in our ensemble. When we compared the detected communities with the anatomical division of the cells using distance and similarity measures for clusterings, we found that the detected communities were more similar to the anatomical division at shorter timescales. That is, when we used a wider time bin to count spikes, and computed pairwise correlations with these spike counts, the correlated communities tended to exist within anatomical regions at shorter timescales, and tended to span anatomical regions at longer timescales. This could reflect localised functional correlations at short time scales rippling outwards across brain regions at longer timescales. The brain may be processing some information quickly locally, and carrying out further, perhaps more detailed, representation over a longer timescale across many regions using the representations that were just built locally.

These changes in communities across timescales could also be driven by the anatomy of the individual cells. For example, it may simply take longer to transmit action potentials over longer distances, hence correlated activity over longer timescales will exist between anatomical regions, rather than within. However, the switch to almost exclusively multi-regional functional networks at 1s bin widths, rather than a mixture of multi-region, and single-region suggests that the inter-regional correlations either overpower, or inhibit the local correlations. So there may be more at play than just timescales.

We acknowledged that the region spanning correlated communities that we detected at longer time scales could exist due to collating activity driven by distinct spontaneous activities. In order to account for this, we modelled the spike counts as a linear function of the top 500 principal components of a video of the mouse's face filmed simultaneously with the electrophysiological readings. We applied our network noise rejection and community detection process to the weighted undirected networks formed by the spike count correlations (or noise correlations) and the signal correlations that we calculated using our model. For the spike count correlation networks, we found much the same results as for the total correlations as described above. For the signal correlations, the communities detected in these networks bore little relation to the anatomical division of the cells. Recent findings have shown that behavioural data accounts for correlations in many brain regions that would otherwise be dismissed as noise (Stringer et al., 2019), our finding shows that these correlations are still

1846 governed by the timescale division between local communication and across-region commu-
1847 nication.

1848 There is a lot of room for further investigation based on this research. For a start, the
1849 data that we used here were collected from nine different regions in the mouse brain, but
1850 none of these regions were part of the somatosensory cortex. Given that a mouse experiences
1851 so much of its environment through its sense of smell, some data from this region would be
1852 interesting to investigate. On the same theme, the mice in the experiment from which the
1853 data were collected were headfixed and placed on a rotating ball, but were otherwise behav-
1854 ing spontaneously. Had these mice been exposed to a visual, aural, or olfactory stimulus,
1855 we could have examined the responses of the cells in the brain regions corresponding to vi-
1856 sion, hearing, and olfaction, and compared these responses to the responses from the other
1857 brain regions. Furthermore, we could have investigated the interaction between the sets of
1858 responses.

1859 Another space for further investigation is the community detection. The algorithm that we
1860 used here never detects overlapping communities. But functional communities could indeed
1861 have overlaps. Clustering methods that detect overlapping clusters do exist (Baadel, Thabtah,
1862 and Lu, 2016). Applying one of those algorithms could yield some interesting results. Also,
1863 the community detection algorithm that we used here cannot process graphs with negative
1864 weights, this forced us to separate positive and negative correlations before applying our
1865 network noise rejection and community detections process, or use the absolute value of our
1866 correlations. A community detection algorithm that can work on weighted undirected graphs
1867 with negative weights could yield some interesting results here.

1868 **Chapter 4**

1869 **A simple two parameter distribution
1870 for modelling neuronal activity and
1871 capturing neuronal association**

1872 *Abstract*

1873 Recent developments in electrophysiological technology have lead to an increase in the size
1874 of electrophysiology datasets. Consequently, there is a requirement for new analysis tech-
1875 niques that can make use of these new datasets, while remaining easy to use in practice. In
1876 this work, we fit some one or two parameter probability distributions to spiking data collected
1877 from a mouse exposed to visual stimuli. We show that the Conway-Maxwell-binomial dis-
1878 tribution is a suitable model for the number of active neurons in a neuronal ensemble at any
1879 given moment. This distribution fits these data better than binomial or beta-binomial distribu-
1880 tions. It also captures the correlated activity in the primary visual cortex induced by stimulus
1881 onset more effectively than simply measuring the correlations, at short timescales (< 10ms).
1882 We also replicate the finding of Churchland et al (2010) relating to stimulus onset quenching
1883 neural variability in cortical areas, and we show a correspondence between this quenching
1884 and changes in one of the parameters of the fitted Conway-Maxwell-binomial distributions.

1885 **4.1 Introduction**

1886 Recent advances in electrophysiological technology, such as ‘Neuropixels’ probes (Jun et al.,
1887 2017) have allowed extracellular voltage measurements to be collected from larger numbers
1888 of cells than traditional methods, in multiple brain regions simultaneously, and routinely.
1889 These larger datasets require innovative methods to extract information from the data in a
1890 reasonable amount of time, ‘reasonable’ being subjective in this case.

1891 Theoretically, all the information at any given moment in an electrophysiological dataset
1892 with n neurons could be captured by calculating the probability distribution for every possi-
1893 ble spiking pattern. This would require defining a random variable with 2^n possible values, a
1894 task that quickly becomes impossible as n increases. Attempts at approximating this random
1895 variable often involve measuring pairwise or higher order correlations (Schneidman et al.,
1896 2006; Flach, 2013; Ganmor, Segev, and Schneidman, 2011). But pairwise correlations may
1897 not be enough to characterise instantaneous neural activity (Tkačik et al., 2014). Further-
1898 more, these kinds of models tend to ignore the temporal structure of neuronal data, in favour
1899 of smaller model size, and scalability.

1900 Higher order correlations would be helpful here, but defining and quantifying these cor-
1901 relations can be tricky (Staude, Grün, and Rotter, 2010). If we use the interaction parameters
1902 arising from the exponential family model as measures of higher order correlations, mea-
1903 suring these correlations becomes computationally impractical quite quickly (the number
1904 of ‘three neuron correlations’ to measure scales with $(^n_3)$). In this work, we dispense with
1905 measuring correlations directly, and we attempt to characterise correlated behaviour using a
1906 parameter in statistical model.

1907 In this work, we examined the ability of simple distributions to model the number of
1908 active (spiking) neurons in a neuronal ensemble at any given timepoint. We compared a
1909 little-known distribution named the Conway-Maxwell-binomial distribution to the binomial
1910 distribution and the beta-binomial distribution. The binomial distribution is a probability dis-
1911 tribution over the number of successes in a sequence of independent and identical Bernoulli
1912 trials. The beta-binomial distribution is similar, but allows for a bit more flexibility while still
1913 being a model for heterogeneity. Similar to the binomial and beta-binomial, the Conway-
1914 Maxwell-binomial distribution is a probability distribution over the number of successes in a
1915 series of Bernoulli trials, but allows over- and under-dispersion relative to the binomial dis-
1916 tribution. This distribution should therefore be a good candidate for our purposes. We found
1917 that Conway-Maxwell-binomial distribution was usually the best candidate of the three that

4.2. Data

1918 we examined.

1919 We also observed some interesting changes in the number of active neurons in the primary
1920 visual cortex and hippocampus at stimulus onset and some changes in this activity in the
1921 thalamus which were sustained for the full duration of the stimulus presentation. This let us
1922 know that there were some responses to model.

1923 We found that fitting a Conway-Maxwell-binomial distribution was a better method of
1924 capturing association between neurons than measuring the spike count correlation for the
1925 short time bins that we used (< 10ms).

1926 Finally, we also wanted to investigate parallels between the parameters of the Conway-
1927 Maxwell-binomial distribution and quantities that have been established as relevant to sen-
1928 sory processing. So, we replicated the findings made by Churchland et al. (2010) relating
1929 to a reduction in neural variability at stimulus onset in the macaque cortical regions, but for
1930 data taken from the mouse primary visual cortex. We compared these findings to the values
1931 of the fitted Conway-Maxwell-binomial distribution parameters.

1932 4.2 Data

1933 We used data collected by Nick Steinmetz and his lab ‘CortexLab at UCL’ (Steinmetz, Caran-
1934 dini, and Harris, 2019). The data can be found online ¹ and are free to use for research
1935 purposes.

1936 Two ‘Phase3’ Neuropixels (Jun et al., 2017) electrode arrays were inserted into the brain
1937 of an awake, head-fixed mouse for about an hour and a half. These electrode arrays recorded
1938 384 channels of neural data each at 30kHz and less than 7 μ V RMS noise levels. The sites
1939 are densely spaced in a ‘continuous tetrode’-like arrangement, and a whole array records
1940 from a 3.8mm span of the brain. One array recorded from visual cortex, hippocampus, and
1941 thalamus, the other array recorded from motor cortex and striatum. The data were spike-
1942 sorted automatically by Kilosort and manually by Nick Steinmetz using Phy. In total 831
1943 well-isolated individual neurons were identified.

1944 4.2.1 Experimental protocol

1945 The mouse was shown a visual stimulus on three monitors placed around the mouse at right
1946 angles to each other, covering about ± 135 degrees azimuth and ± 35 degrees elevation.

¹<http://data.cortexlab.net/dualPhase3/>

1947 The stimulus consisted of sine-wave modulated full-field drifting gratings of 16 drift di-
1948 rections ($0^\circ, 22.5^\circ, \dots, 337.5^\circ$) with 2Hz temporal frequency and 0.08 cycles/degree spatial
1949 frequency displayed for 2 seconds plus a blank condition. Each of these 17 conditions were
1950 presented 10 times in a random order across 170 different trials. There were therefore 160
1951 trials with a drifting-grating visual stimulus present, and 10 trials with a blank stimulus.

1952 **4.3 Methods**

1953 **4.3.1 Binning data**

1954 We converted the spike times for each cell into spike counts by putting the spike times into
1955 time bins of a given ‘width’ (in milliseconds). We used time bins of 1ms, 5ms, and 10ms.
1956 We used different time bin widths to assess the impact of choosing a bin width.

1957 **4.3.2 Number of *active* neurons**

1958 To count the number of active neurons in each neuronal ensemble, we split the time interval
1959 for each trial into bins of a given width. We counted the number of spikes fired by each cell
1960 in each bin. If a cell fired *at least* one spike in a given bin, we regarded that cell as active in
1961 that bin. We recorded the number of active cells in every bin, and for the purposes of further
1962 analysis, we recorded each cell’s individual spike counts.

1963 It should be noted that when we used a bin width of 1ms, the maximum number of
1964 spikes in any bin was 1. For the wider time bins, some bins had spike counts greater than
1965 1. Consequently when using a bin width of 1ms, the number of active neurons and the total
1966 spike count of a given bin were identical. But for wider bin widths, the total spike count was
1967 greater than the number of active neurons.

1968 So for the 1ms bin width, the activity of a neuron and the number of spikes fired by that
1969 neuron in any bin can be modelled as a Bernoulli variable. But for wider time bins, only the
1970 activity can be modelled in this way.

1971 **4.3.3 Moving windows for measurements**

1972 When taking measurements (e.g. moving average over the number of active neurons) or
1973 fitting distributions (eg. the beta binomial distribution) we slid a window containing a certain
1974 number of bins across the data, and made our measurements at each window position. For
1975 example, when analysing 1ms bin data, we used a window containing 100 bins, and we slid

4.3. Methods

Bin width (ms)	Window size (bins)	Window size (ms)	Windows per trial
1ms	100	100ms	296
5ms	40	200ms	286
10ms	40	400ms	266

TABLE 4.1: Details of the different bin width and analysis window sizes used when binning spike times, and analysing those data.

1976 the window across the time interval for each trial moving 10 bins at a time. So that for
 1977 3060ms of data, we made 296 measurements.

1978 For the 5ms bin width data, we used windows containing 40 bins, and slid the window 2
 1979 bins at a time when taking measurements.

1980 For the 10ms bin width data, we used windows containing 40 bins, and slid the window
 1981 1 bin at a time when taking measurements (see table 4.1 for concise details).

1982 By continuing to use windows containing 40 bins, we retained statistical power but sac-
 1983 rificed the number of measurements taken.

1984 There was an interval between each trial with a grey image in place of the moving bar
 1985 stimulus. This interval varied in time. But we included some of this interval when recording
 1986 the data for each trial. We started recording the number of active neurons, and the number
 1987 of spikes from each neuron from 530ms before each trial until 1030ms after each trial. This
 1988 way, we could see the change in our measurements at the onset of a stimulus and the end of
 1989 stimulus presentation.

1990 As mentioned in section 4.3.2, we recorded the number of active neurons in each bin, and
 1991 the spike count for each neuron in each bin. The measurements we took using these data in
 1992 each window were as follows:

1993 **Moving average** The average number of active cells in each window.

1994 **Moving variance** The variance of the number of active cells in each window.

1995 **Average correlation** We measured the correlation between the spike counts of each pair of
 1996 cells in the ensemble, and took the average of these measurements.

1997 **Binomial p** We fitted a binomial distribution to the data in each window and recorded the
 1998 fitted probability of success, p in each case.

1999 **Beta-binomial α, β** We fitted a beta-binomial distribution to the data in each window, and
 2000 recorded the values of the fitted shape parameters, α and β , of each distribution.

2001 **Conway-Maxwell-binomial distribution p, ν** We fitted a Conway-Maxwell-binomial dis-
2002 tribution to the data in each window, and recorded the fitted values of p and ν for each
2003 distribution.

2004 **Log-likelihoods** We also recorded the log-likelihood of each of the fitted distributions for
2005 each window.

2006 **4.3.4 Fano factor**

The *Fano factor* of a random variable is defined as the ratio of the variable's variance to its mean.

$$F = \frac{\sigma^2}{\mu} \quad (4.1)$$

2007 We measured the Fano factor of the spike count of a given cell by measuring the mean and
2008 variance of the spike count across trials, and taking the ratio of those two quantities. When
2009 calculated in this way the Fano factor can be used as a measure of neural variability that
2010 controls for changes in the firing rate. This is similar to the calculation used in (Churchland
2011 et al., 2010).

2012 **4.3.5 Probability Distributions suitable for modelling ensemble activity**

2013 We present here three different probability distributions that could be suitable to model the
2014 number of active neurons in an ensemble. Each distribution has the set $\{0, \dots, n\}$ as its sup-
2015 port, where n is the number of neurons in the ensemble. These are simple distributions with
2016 either two or three parameters each. However, we regard n as known when using these dis-
2017 tributions for modelling, so in effect each distribution has either one or two free parameters.

2018 **Association**

2019 *Association* between random variables is similar to the correlation between random variables
2020 but is more general in concept. The correlation coefficient is a measure of association; and
2021 association doesn't necessarily have a mathematical definition like correlation does. Essen-
2022 tially, an association between two random variables is a dependency of any kind. Positively
2023 associated variables tend to take the same value, and negatively associated variables tend to
2024 take different values. In this research, we work with probability distributions of the num-
2025 ber of successes in a set of Bernoulli trials. These Bernoulli variables may or may not be
2026 associated.

4.3. Methods

2027 A probability distribution over the number of successes in n Bernoulli trials, where the
2028 Bernoulli variables may be associated, could constitute a good model for the number of active
2029 neurons in an ensemble of n neurons. As long as the observation period is divided into time
2030 bins short enough so that any neuron is unlikely to fire more than spike in any time bin.

2031 **Binomial distribution**

The binomial distribution is a two parameter discrete probability distribution that can be thought of as a probability distribution the number of successes from n independent Bernoulli trials, each with the same probability of success. The parameters of the binomial distribution are n the number of trials, and $0 \leq p \leq 1$, the probability of success for each of these trials. A random variable with the binomial distribution can take values from $\{0, \dots, n\}$.

The probability mass function of the distribution is

$$P(k; n, p) = \binom{n}{k} p^k (1-p)^{n-k} \quad (4.2)$$

2032 As a model for the activity of a neuronal ensemble, the main problem with the binomial
2033 distribution is that it treats each neuron, represented as a Bernoulli trial, as independent. It is
2034 well known that neurons are not independent, and that correlated behaviour between neurons
2035 is vital for representing sensory information (Cohen and Maunsell, 2009). The binomial dis-
2036 tribution falls short in this regard, but it is useful as performance benchmark when assessing
2037 the performance of other models.

2038 **Beta-binomial distribution**

2039 The beta distribution is the conjugate distribution of the binomial distribution. The beta-
2040 binomial distribution is the combination of the beta distribution and the binomial distribution,
2041 in that the probability of success for the binomial distribution is sampled from the beta dis-
2042 tribution. This allows the beta-binomial distribution to capture some over dispersion relative
2043 to the binomial distribution.

The beta-binomial distribution is a three parameter distribution, n the number of Bernoulli trials, and $\alpha \in \mathbb{R}_{>0}$ and $\beta \in \mathbb{R}_{>0}$ the shape parameters of the beta distribution. The probability mass function for the beta-binomial distribution is

$$P(k; n, \alpha, \beta) = \binom{n}{k} \frac{B(k + \alpha, n - k + \beta)}{B(\alpha, \beta)} \quad (4.3)$$

2044 where $B(\alpha, \beta)$ is the beta function.

This probability distribution can be reparametrised in a number of ways. One of which defines new parameters π and ρ by

$$\pi = \frac{\alpha}{\alpha + \beta} \quad (4.4)$$

$$\rho = \frac{1}{\alpha + \beta + 1} \quad (4.5)$$

2045 This reparametrisation is useful because π acts as a location parameter analogous to the p
2046 parameter of a binomial distribution. A value of $\rho > 0$ indicates over-dispersion relative to a
2047 binomial distribution.

2048 As a model for the activity of a neuronal ensemble, the beta-binomial distribution is
2049 more suitable than a binomial distribution because the over-dispersion of the beta-binomial
2050 distribution can be used to model positive association between the neurons. An extreme
2051 example of this over-dispersion/positive association can be seen in figure 4.1b. In this figure,
2052 the neurons are positively associated and so tend to take the same value, consequently the
2053 probability mass of the beta-binomial distribution builds up close to $k = 0$ and $k = n$. It is
2054 worth noting that the location parameter for each distribution has the same value, $p = \pi =$
2055 0.5.

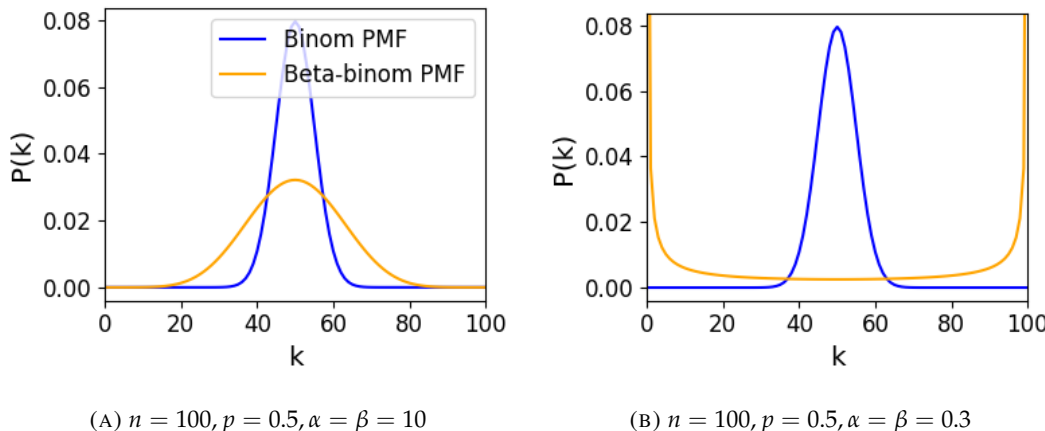


FIGURE 4.1: Figures showing the over-dispersion possible for a beta-binomial distribution relative to a binomial distribution. Parameters are shown in the captions.

2056 **Conway-Maxwell-binomial distribution**

2057 The Conway-Maxwell-binomial distribution (COMb distribution) is a three parameter generalisation of the binomial distribution that allows for over dispersion and under dispersion

4.3. Methods

relative to the binomial distribution. The parameters of the distribution are n the number of Bernoulli trials, and two shape parameters $0 \leq p \leq 1$, and $\nu \in \mathbb{R}$.

The probability mass function of the COMb distribution is

$$P(k; n, p, \nu) = \frac{1}{S(n, p, \nu)} \binom{n}{k}^{\nu} p^k (1-p)^{n-k} \quad (4.6)$$

where

$$S(n, p, \nu) = \sum_{j=0}^n \binom{n}{j}^{\nu} p^j (1-p)^{n-j} \quad (4.7)$$

The only difference between this PMF and the PMF for the standard binomial is the introduction of ν and the consequent introduction of the normalising function $S(n, p, \nu)$.

Indeed, if $\nu = 1$ the COMb distribution is identical to the binomial distribution with the same values for n and p . We can see in figure 4.2d that the KL-divergence $D_{KL}(P_{COMb}(n, p, \nu) || P_{Bin}(n, p)) = 0$ along the line where $\nu = 1$. The analytical expression for the divergence is

$$D_{KL}(P_{COMb}(k; n, p, \nu) || P_{Bin}(k; n, p)) = (\nu - 1) E_{P_{COMb}(k; n, p, \nu)} \left[\log \binom{n}{k} \right] \quad (4.8)$$

$$- \log S(n, p, \nu) \quad (4.9)$$

At $\nu = 1$, we have $S(n, p, 1)$ which is just the sum over the binomial PMF, so $S(n, p, 1) = 1$ and therefore $D_{KL}(P_{COMb}(n, p, \nu) || P_{Bin}(n, p)) = 0$.

If $\nu < 1$ the COMb distribution will exhibit over-dispersion relative to the binomial distribution. If $p = 0.5$ and $\nu = 0$ the COMb distribution is the discrete uniform distribution, and if $\nu < 0$ the mass of the COMb distribution will tend to build up near $k = 0$ and $k = n$. This over-dispersion represents positive association in the Bernoulli variables. An example of this over-dispersion can be seen in figure 4.2b.

If $\nu > 1$ the COMb distribution will exhibit under-dispersion relative to the binomial distribution. The larger the value of ν the more probability mass will build up at $n/2$ for even n , or at $\lfloor n/2 \rfloor$ and $\lceil n/2 \rceil$ for odd n . This under-dispersion represents negative association in the Bernoulli variables. An example of this under-dispersion can be seen in figure 4.2a.

It should be noted that the p parameter of the COMb distribution does not correspond to the mean of the distribution, as is the case for the binomial p parameter, and beta-binomial π parameter. That is, the COMb p parameter is not a location parameter. An illustration of this can be seen in figure 4.2c. This is because an interaction between the p and ν parameters skews the mean. There is no analytical expression for the mean of the COMb distribution.

ν	Relative dispersion	Association between neurons/variables
< 1	over	positive
1	none	none
> 1	under	negative

TABLE 4.2: Relative dispersion of the COMb distribution, and association between Bernoulli variables as represented by the value of the ν parameter.

2079 Since the COMb distribution has the potential to capture positive and negative associa-
2080 tions between the neurons/Bernoulli variables, it should be an excellent candidate for mod-
2081 elling the number of active neurons in a neuronal ensemble.

2082 We wrote a dedicated Python package to enable easy creation and fitting of COMb dis-
2083 tribution objects. The format of the package imitates the format of other distribution objects
2084 from the `scipy.stats` Python package. The COMb package can be found here:
2085 https://github.com/thomasjdelaney/Conway_Maxwell_Binomial_Distribution

2086 4.3.6 Fitting

2087 We fitted binomial, beta-binomial, and Conway-Maxwell-binomial (COMb) distributions to
2088 the neural activity in each of the overlapping windows covering each trial. To fit the distribu-
2089 tions we minimised the appropriate negative log likelihood function using the data from the
2090 window.

There is an analytical solution for maximum likelihood estimate of the binomial distribution's p parameter.

$$\hat{p} = \frac{1}{n} \sum_{i=1}^N k_i \quad (4.10)$$

2091 We minimised the negative log likelihood function of the beta-binomial distribution nu-
2092 merically. We calculated the negative log likelihood for a sample directly, by taking the sum
2093 of the log of the probability mass function for each value in the sample. We minimised the
2094 negation of that function using the `minimise` function of the `scipy.optimize` Python
2095 package.

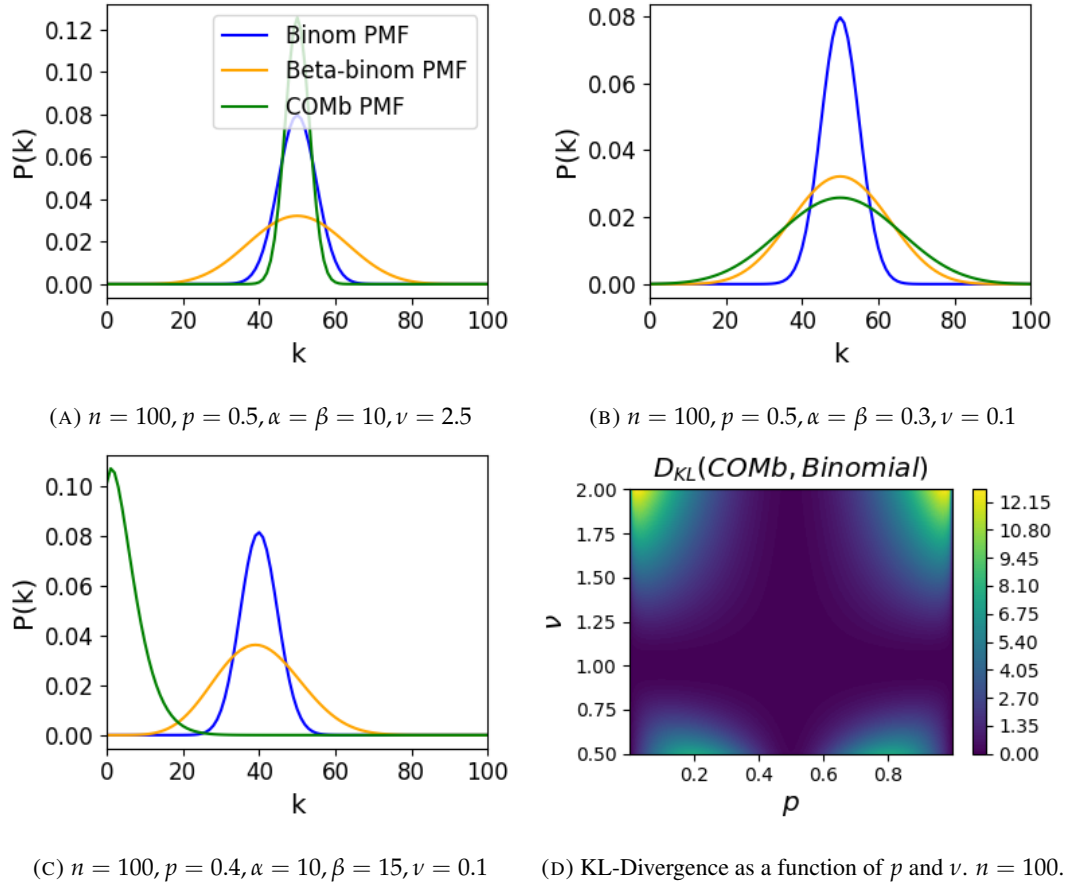


FIGURE 4.2: Figures showing (A) the under-dispersion and (B) over-dispersion permitted by the COMb distribution relative to a binomial distribution. (C) illustrates that the p parameter of the COMb distribution does not correspond to the mean of the distribution, as it does for the binomial and beta-binomial distributions. (D) shows a heatmap for the value of the Kullback-Liebler divergence between the COMb distribution and the standard binomial distribution with same value for n , as a function of p and ν . Parameters are shown in the captions.

The log likelihood function of the COMb distribution given some sample $\{k_1, \dots, k_N\}$ is

$$\ell(p, \nu | k_1, \dots, k_N) = N [n \log(1 - p) - \log S(n, p, \nu)] \quad (4.11)$$

$$+ \log \frac{p}{1 - p} \sum_{i=1}^N k_i \quad (4.12)$$

$$+ \nu \sum_{i=1}^N \log \binom{n}{k_i} \quad (4.13)$$

2096 We minimised the negation of this function using numerical methods. More specifically, we
2097 used the `minimise` function of the `scipy.optimize` Python package.

2098 **4.3.7 Goodness-of-fit**

2099 After fitting, we measured the goodness-of-fit of each model/distribution with their log like-
2100 lihood. We calculated this directly using the `logpmf` functions of the distribution objects in
2101 Python.

2102 **4.4 Results**

2103 We defined a neuron as *active* in a time bin if it fires at least one spike during the time interval
2104 covered by that bin. We measured the number of active neurons in the primary visual cortex
2105 of a mouse in 1ms bins across 160 trials of a moving bar visual stimulus. We then slid a
2106 100ms window across these 1ms bins taking measurements, and fitting distributions along
2107 the way. We did the same for neurons in the thalamus, hippocampus, striatum, and motor
2108 cortex. We repeated the analysis for 5ms time bins with 40 bin windows, and 10ms time bins
2109 with 40 bin windows.

2110 **4.4.1 Increases in mean number of active neurons and variance in number of
2111 active neurons at stimulus onset in some regions**

2112 We measured the average number of active neurons, and the variance of the number of active
2113 neurons in a 100ms sliding window starting 500ms before stimulus onset until 1000ms after
2114 stimulus onset. We found differences in the response across regions. There were no observed
2115 changes in response to the stimulus in the motor cortex or the striatum. The changes in the
2116 other regions are detailed below.

4.4. Results

2117 Primary visual cortex

2118 We found a transient increase in both the average and variance of the number of active neu-
2119 rons at stimulus onset, followed by a fall to pre-stimulus levels, followed by another transient
2120 increase (see figure 4.3). The oscillation in both of these measurements appear to reflect the
2121 frequency of the stimulus (see Data section 4.2.1), and it is known that stimulus structure can
2122 influence response structure(Litwin-Kumar, Chacron, and Doiron, 2012). We see a similar
2123 but lower amplitude oscillation at the end of the stimulus presentation.

2124 Hippocampus

2125 In the hippocampus we observed a transient increase in the average number of active neurons
2126 and in the variance of the number of active neurons at stimulus onset (see figure 4.4). The
2127 increase lasted about 125ms, and the subsequent fall to baseline took the a similar amount of
2128 time.

2129 Thalamus

2130 In the thalamus we observed a transient increase in the both the average and variance of
2131 the number of active neurons on stimulus onset, followed by a fall to pre-stimulus levels,
2132 followed by a sustained increase until the stimulus presentation ends.

2133 As one you might expect for a visual stimulus, the change in the average number of active
2134 neurons was greatest in the primary visual cortex. In this region, this quantity doubled on
2135 stimulus onset. In contrast, in the hippocampus and the thalamus, the average number of
2136 active neurons only increased by a fraction of the unstimulated baseline value. The duration
2137 of the response in V1 and the hippocampus at stimulus onset was 300 – 400ms, but the
2138 response in the thalamus appeared to last for the duration of stimulus presentation. The V1
2139 also showed a change in the average number of active neurons at stimulus end. The change
2140 was similar to that observed at stimulus onset, but smaller in magnitude (see figures 4.3, 4.4,
2141 and 4.5)

2142 4.4.2 Conway-Maxwell-binomial distribution is usually a better fit than bino- 2143 mial or beta-binomial

2144 Since the Conway-Maxwell-binomial distribution has not been fitted to neuronal data before,
2145 it is not clear that it would be a better fit than the binomial or beta-binomial distributions.
2146 In order to find out which parametric distribution was the best fit for the largest proportion

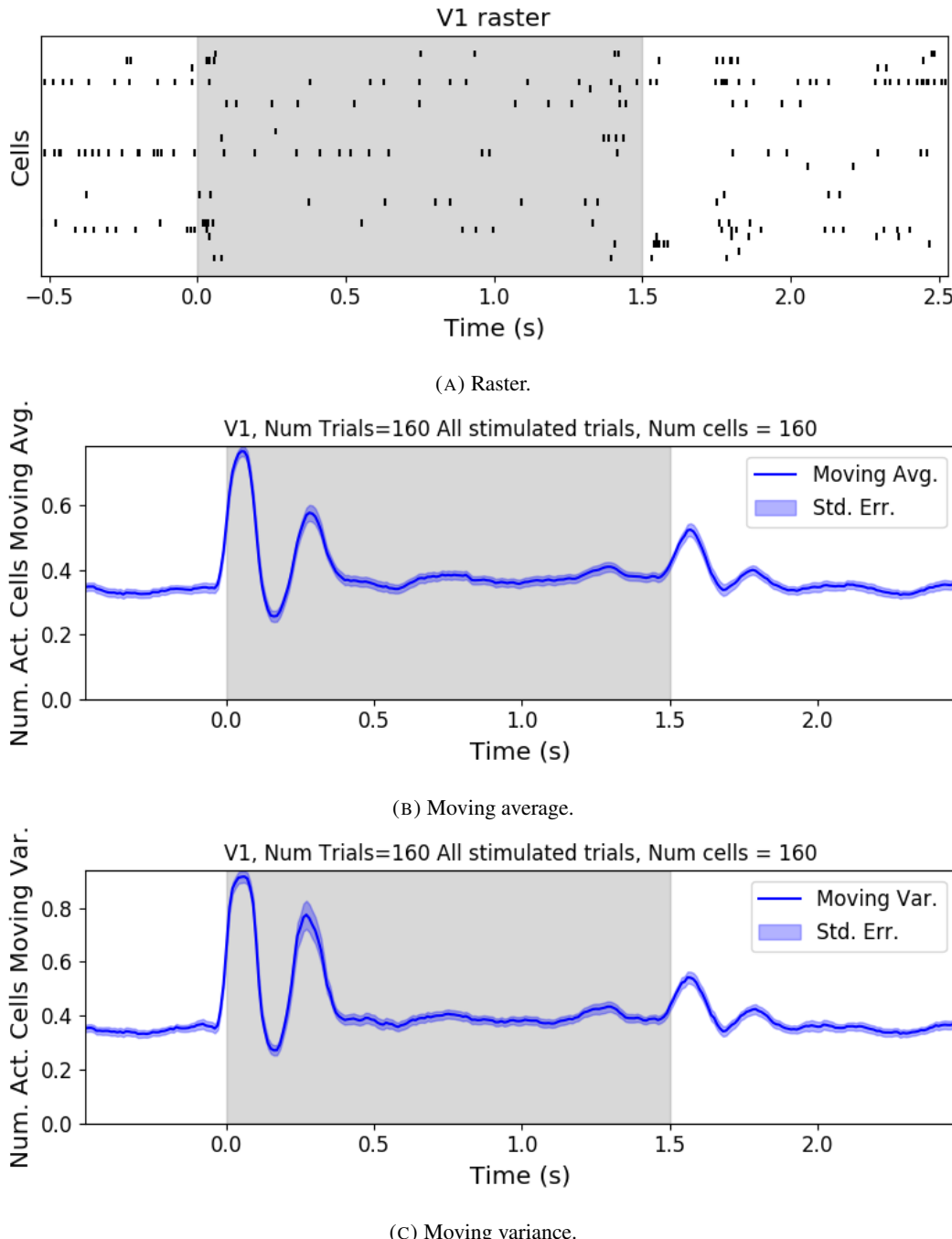


FIGURE 4.3: (A) Raster plot showing the spikes fired by 33 randomly chosen neurons in the primary visual cortex. (B-C) (B) average and (C) variance of the number of active neurons, measured using a sliding window 100ms wide, split into 100 bins. The midpoint of the time interval for each window is used as the timepoint (x-axis point) for the measurements using that window. The grey shaded area indicates the presence of a visual stimulus. The opaque line is an average across the 160 trials that included a visual stimulus of any kind. We can see a transient increase in the average number of active neurons and the variance of this number, followed by a fluctuation and another increase.

4.4. Results

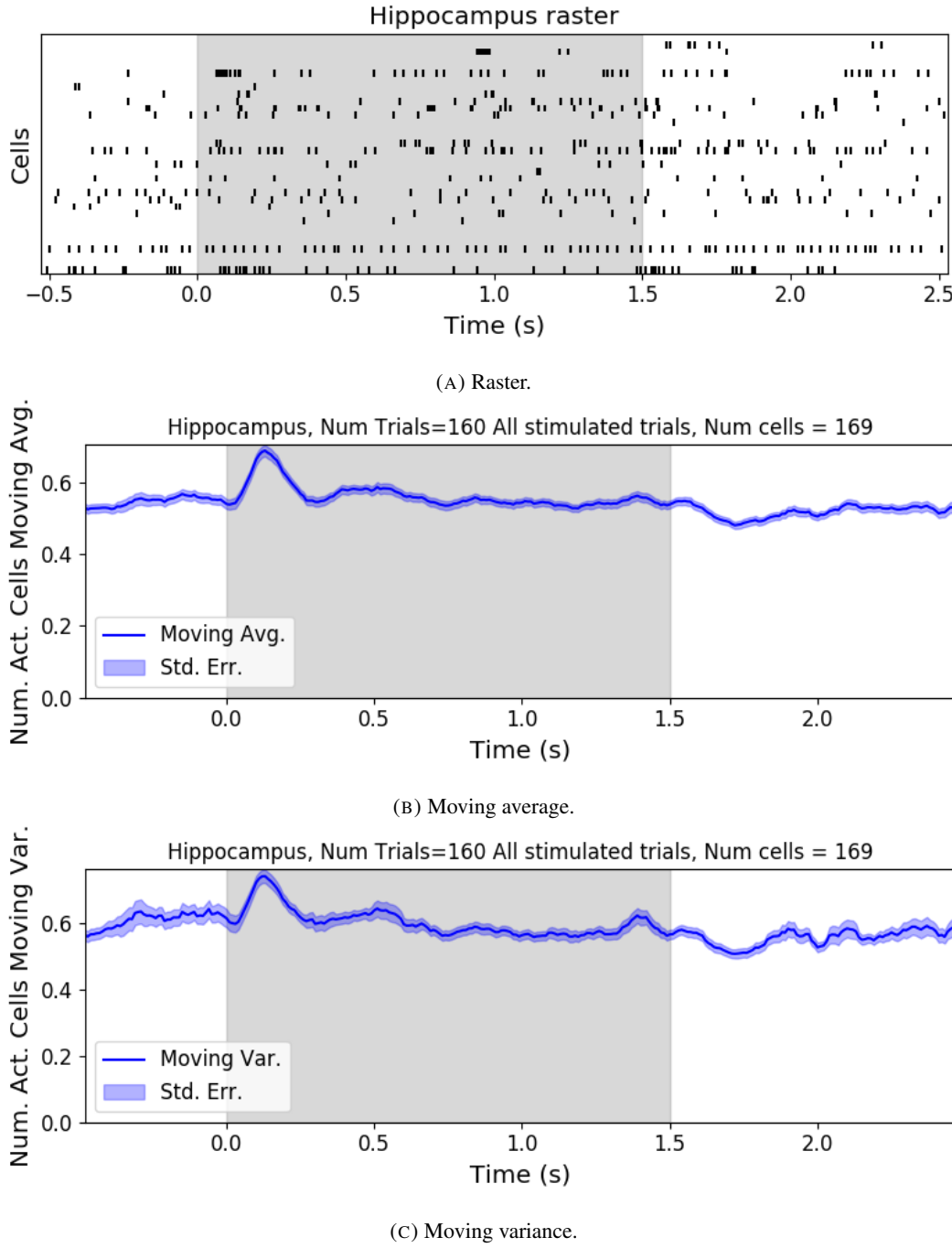


FIGURE 4.4: (A) Raster plot showing the spikes fired by 33 randomly chosen neurons in the hippocampus. (B-C) (B) average and (C) variance of the number of active neurons, measured using a sliding window 100ms wide, split into 100 bins. The midpoint of the time interval for each window is used as the timepoint (x-axis point) for the measurements using that window. The grey shaded area indicates the presence of a visual stimulus. The opaque line is an average across the 160 trials that included a visual stimulus of any kind. We can see a transient increase in the average number of active neurons and the variance of this number at stimulus onset.

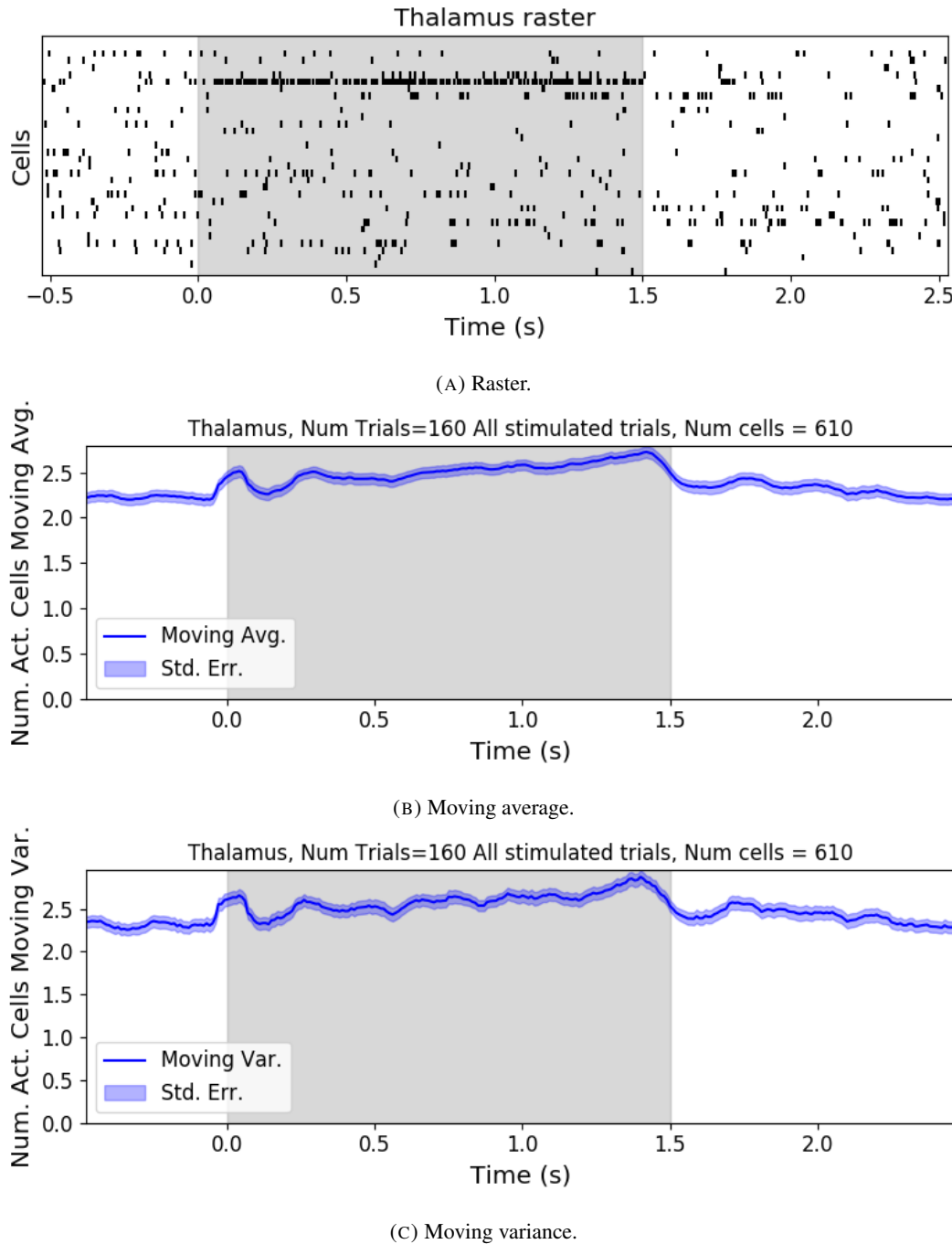
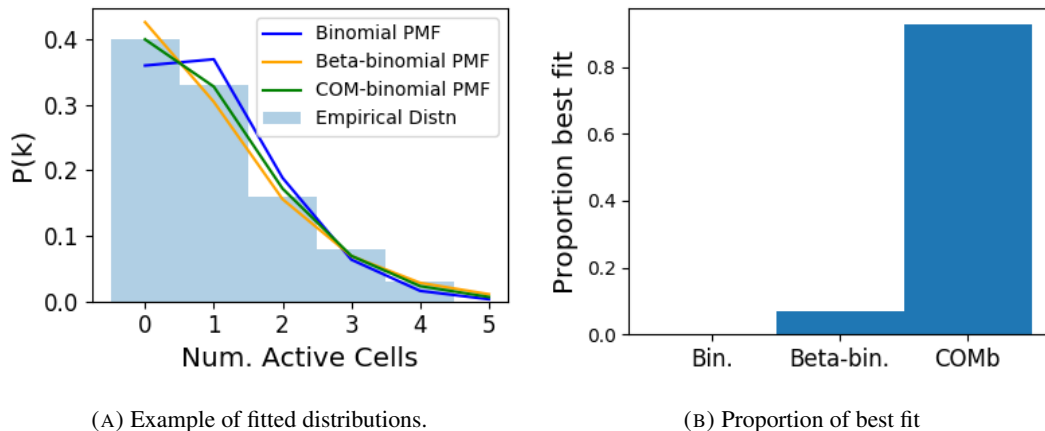


FIGURE 4.5: (A) Raster plot showing the spikes fired by 33 randomly chosen neurons in the thalamus. (B-C) (B) average and (C) variance of the number of active neurons, measured using a sliding window 100ms wide, split into 100 bins. The midpoint of the time interval for each window is used as the timepoint (x-axis point) for the measurements using that window. The grey shaded area indicates the presence of a visual stimulus. The opaque line is an average across the 160 trials that included a visual stimulus of any kind. We can see an immediate increase at stimulus onset, a subsequent fall, and another sustained increased until the stimulus presentation ends.

4.4. Results

of our data, we fit a binomial, a beta-binomial, and a Conway-Maxwell-binomial (COMb) distribution to each window for each bin width, and each region. Then we assessed the goodness-of-fit of each distribution by calculating the log-likelihood of each fitted distribution using the associated sample. We measured the proportion of samples for which each distribution was the best fit, for each bin width value and each region.

We found that the COMb distribution was the best fit for most of the samples regardless of bin width or region. The bin width had an effect on the number of samples for which the COMb distribution was the best fit. The results are summarised in table 4.3. For a bin width of 1ms, the COMb distribution was the best fit for over 90% of samples, the beta-binomial distribution was the best fit for less than 10% of samples, and the binomial distribution was the best fit for less than 1% of samples, across regions. For 5ms bins, the COMb distribution was the best fit for 70 – 80% of samples, the beta-binomial distribution was the best fit for 20 – 30% of the samples, and again the binomial distribution was the best fit for less than 1% of samples, across regions. Finally, for 10ms bins, the COMb distribution was the best fit for 53 – 80% of samples, the beta-binomial distribution was the best fit for 20 – 47% of the samples, and the binomial distribution was the best fit for less than 0.1% of samples, across regions.



(A) Example of fitted distributions.

(B) Proportion of best fit

FIGURE 4.6: (A) An example of the binomial, beta-binomial, and Conway-Maxwell-binomial distributions fitted to a sample of neural activity. The Conway-Maxwell-binomial distribution is the best fit in this case. The histogram shows the empirical distribution of the sample. The probability mass function of each distribution is indicated by a different coloured line. (B) Across all samples in all trials, the proportion of samples for which each fitted distribution was the best fit. The Conway-Maxwell-binomial distribution was the best fit for 93% of the samples taken from V1 using a bin width of 1ms.

Bin Width (ms)	Binomial	Beta-binomial	COMb
1ms	< 1%	< 10%	> 90%
5ms	< 0.1%	20 – 30%	70 – 80%
10ms	< 0.1%	20 – 47%	53 – 80%

TABLE 4.3: Proportion of samples for which each distribution was the best fit, grouped by bin width. The COMb distribution is the best fit most of the time.

2164 **4.4.3 Conway-Maxwell-binomial distribution captures changes in association
2165 at stimulus onset**

2166 We fit a Conway-Maxwell-binomial (COMb) distribution to the number of active neurons in
2167 the 1ms time bins in a 100ms sliding window. We also measured the correlation coefficient
2168 between the spike counts of all possible pairs of neurons, and took the average of these
2169 coefficients. We did this for all the trials with a visual stimulus. We observed a reduction in
2170 the COMb distribution's ν parameter at stimulus onset from around 1 to between 0 and 1 (see
2171 figure 4.7a). A value of ν less than 1 indicates positive association between the neurons (see
2172 section 4.3.5). We might expect to see this positive association reflected in the correlation
2173 coefficients, but this is not the case. We see no change in the time series of average correlation
2174 measures at stimulus onset.

2175 This may be due to the very short time bin we used in this case. We know that using small
2176 time bins can artificially reduce correlation measurements (Cohen and Kohn, 2011). In this
2177 case, fitting the COMb distribution may be a useful way to measure association in a neuronal
2178 ensemble over very short timescales (< 10ms).

2179 **4.4.4 Replicating stimulus related quenching of neural variability**

2180 Churchland et al. (2010) inspected the effect of a stimulus on neural variability. One of the
2181 measures of neural variability that they employed was the Fano factor of the spike counts of
2182 individual cells (see section 4.3.4). They found a reduction in neural variability as measured
2183 by the Fano factor in various cortical areas in a macaque at the onset of various visual stimuli,
2184 or a juice reward (Churchland et al., 2010).

2185 We measured the Fano factor of the spike count of each cell in each brain region, during
2186 each trial. We measured the mean and standard error of these Fano factors from 500ms
2187 before stimulus onset until 1000ms after stimulus end. For the primary visual cortex, we
2188 found a transient reduction in the Fano factor immediately after stimulus onset. We used
2189 a Mann-Whitney U test to check that the Fano factors measured in a window starting at

4.4. Results

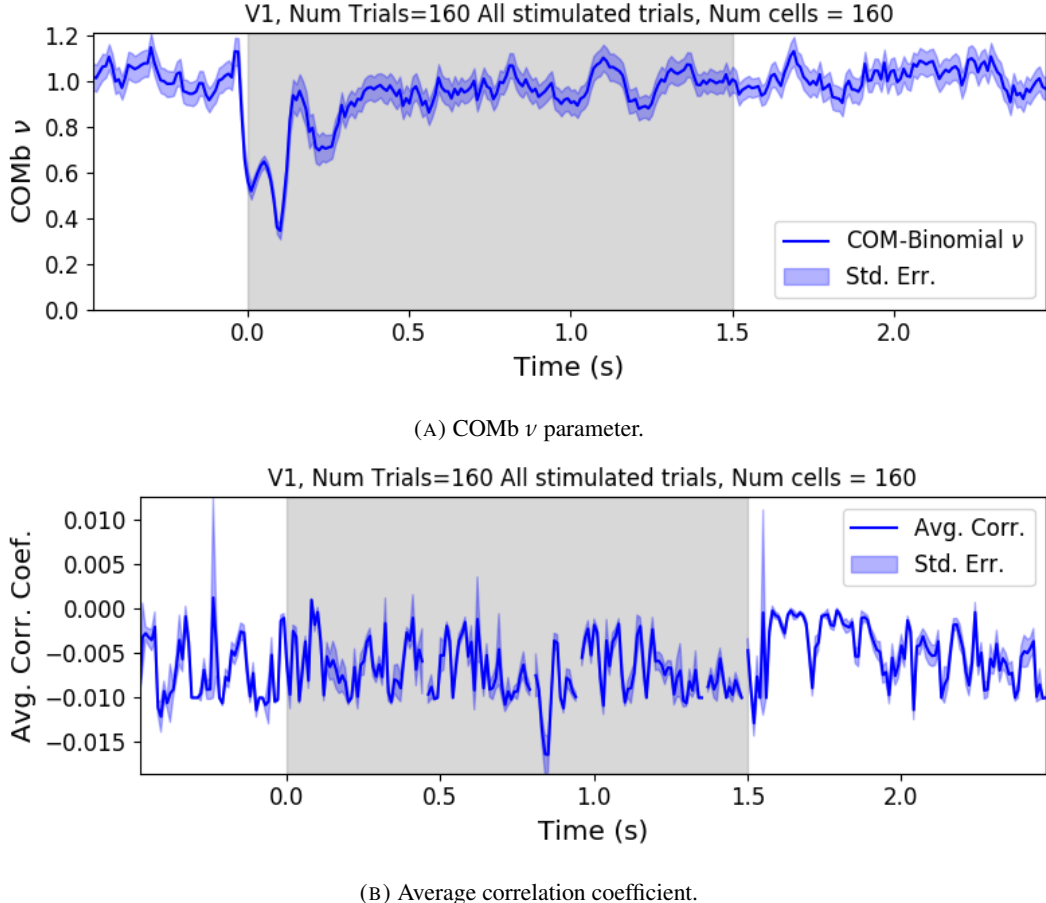


FIGURE 4.7: (A) We fit a Conway-Maxwell-binomial distribution to the number of active neurons in 1ms time bins of a 100ms sliding window. We did this for all trials with a visual stimulus and took the average across those trials. We see a transient drop in value for the distribution’s ν parameter at stimulus onset. This shows an increase in positive association between the neurons. (B) We measured the correlation coefficient between the spike counts of all possible pairs of neurons in the same sliding window. The took the average of those coefficients. We also did this for every visually stimulated trial, and took the average across trials. The increase in positive association is not reflected with an increase in average correlation.

stimulus onset and ending 100ms later were significantly lower than the factors measured in a window ending at stimulus onset ($p < 0.001$, see figure 4.8a). We did not get this statistically significant result in any other region.

Our findings agree with those of Churchland et al. for the primary visual cortex. However Churchland also found a reduction in the Fano factor in the dorsal premotor cortex (PMd) at stimulus onset. Our measurements from the mouse motor cortex show no change at stimulus onset (see figure 4.8b). This could indicate some difference in the functionality of the motor cortex in a macaque and the motor cortex of a mouse.

Similar to these findings in the Fano factor, we found a reduction in the ν parameter of the COMB distribution on stimulus onset in V1 (figure 4.7a) and in no other region from

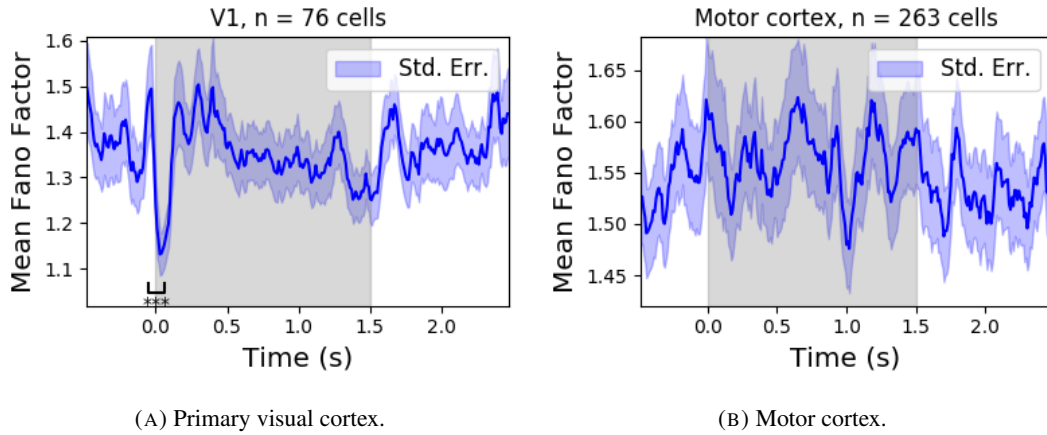


FIGURE 4.8: (A) The mean Fano factor of the spike counts of the cells in the primary visual cortex. Means were taken across cells first, then across trials. There was a significant decrease in the Fano factors immediately after stimulus onset. (B) The mean Fano factor of the spike counts of the cells in the motor cortex. No significant change in measurements at any point.

which we had data. Specifically, the ν parameter reduced from around 1, to between 1 and 0. This represents a change from no association between the neurons, to a positive association. It is possible that this positive association may be responsible for the reduction in the Fano factor.

4.5 Discussion

Our aim in this research was to develop a new statistical method for analysing the activity of a neuronal ensemble at very short timescales. We wanted our method to use information taken from the whole ensemble, but we also wanted the method to be quick and easy to implement. It is likely that analysis methods with these characteristics will become valuable as electrophysiological datasets include readings from more cells over longer time periods. In this case, we used the number of active, or spiking, neurons in a very short time bin ($< 10\text{ms}$) as a measure of ensemble activity.

First of all, we showed that there were changes in response that we could model at these very short time scales in some of the brain regions from which we had recordings. We observed changes in the average number of active neurons, and the variance of the number of active neurons in three different brain regions in response to visual stimuli. Since we know that correlated behaviour is associated with sensory perception (deCharms and Merzenich, 1996), we might hope to measure the pairwise correlations within the neuronal population in order to further investigate these responses. But, using such short time bins can produce

4.5. Discussion

artificially small spike count correlation measurements (Cohen and Maunsell, 2009). Overcoming this limitation was one of our objectives for our new method. In order to do this, we abandoned the idea of measuring the correlations directly and embraced the concept of *association*. In order to quantify the association between neurons, we used the Conway-Maxwell-binomial distribution to model the number of active (spiking) neurons in an ensemble as a sum of possibly associated Bernoulli random variables.

We showed that the Conway-Maxwell-binomial distribution performed better than the more common options of the binomial and beta-binomial distributions. Furthermore, we showed that the positively associated behaviour between neurons in the primary visual cortex could be captured by fitting a Conway-Maxwell-binomial distribution, but was not captured by the more standard approach of measuring the spike count correlation. The associated behaviour could not be measured using spike count correlations, because of the very short bins required to capture short timescale behaviour.

We replicated a famous result from Churchland et al (2010) relating to the quenching of neural variability in cortical areas at stimulus onset, and in doing so, we established a correspondence between the association quantifying parameter of the Conway-Maxwell-binomial (COMb) distribution and the neural variability as measured by the Fano factor. We found a reduction in the ν parameter of the COMB distribution at stimulus onset, indicating a change from no association to positive association between neurons in V1. We found a corresponding reduction in the Fano factor of the individual cells in V1. The positive association between neurons induced by the stimulus would constrain the neurons to fire at the same time. The stimulus also induced a larger number of neurons to spike. These two actions combined could cause an increase in the firing rate of individual cells that is greater in magnitude than the increase in firing rate variability. If this is indeed the case, then the association as captured by the COMB distribution could be regarded as one of the ‘natural parameters’ of the ensemble response for short timescales. That is, a quantity that directly measures some aspect of the behaviour of the ensemble. In this case, it the correlated behaviour of the individual neurons is captured.

This work could be just a first step in creating analysis methods based on the Conway-Maxwell-binomial distribution, or similar statistical models. One way to extend the method would be to pair it up with the ‘Population Tracking model’ (O’Donnell et al., 2017). This model attempts to characterise the interaction between an ensemble and each member of the ensemble by quantifying the probability of spiking for a given a cell, given the number of active cells in the whole population. Combining this model with the COMB distribution

2253 would give us a model that could accurately fit the number of active neurons at any moment,
2254 and that gives a probability of firing for each cell, and therefore probabilities for full spiking
2255 patterns, without adding a huge number of parameters to fit.

2256 A more complex way to extend the model would be to fit a Conway-Maxwell-binomial
2257 distribution to data recorded from multiple brain regions simultaneously, with a different fit
2258 for each region, then to analyse the temporal relationship between the fitted parameters of
2259 each region. If we analysed the time series of the COMB distribution parameters from the
2260 different regions, looking at cross-correlations between regions, this may give some results
2261 relating to the timescales in which information is processed in different brain regions.

2262 **Chapter 5**

2263 **Studies with practical limitations &**
2264 **negative results**

2265 *Abstract*

2266 Here I will present some details on research topics that I started, but that unfortunately did not
2267 lead anywhere useful. There are two pieces of research, based on two papers. Each paper is
2268 related to the overall theme of my PhD of analysing and modelling behaviours of populations
2269 of neurons. The first part is based on a model of parallel spike trains including higher order
2270 interactions by Shimazaki et al (2012). The second part is based on a multiscale model for
2271 making inferences on hierarchical data.

2272 **5.1 Dynamic state space model of pairwise and higher order neu-**
2273 **ronal correlations**

2274 In their paper Shimazaki et al (2012) aimed to model spike trains from populations of neurons
2275 in parallel, with pairwise and higher order dynamic interactions between the trains. They
2276 modelled the spike trains as multi-variate binary processes using a log-linear model, and they
2277 extracted spike interaction parameters using a Bayesian filter/EM-algorithm. They developed
2278 a goodness-of-fit measure for the model to test if including these higher order correlations
2279 is necessary for an accurate model. Their measure was based on the Bayes factor but they
2280 also assessed the suitability of higher order models using the AIC and BIC. So the increase
2281 in the number of parameters associated with fitting higher order interactions was taken into
2282 account. They tested the performance of the model on synthetic data with known higher
2283 order correlations. They used the model to look for higher order correlations in data from
2284 awake behaving animals. They use the model to demonstrate dynamic appearance of higher
2285 order correlations in the monkey motor cortex (Shimazaki et al., 2012).

2286 We used the available Python repository to implement the model, and we successfully
2287 worked through the tutorial provided. But we found that the model did not scale well to
2288 larger populations. We attempted to fit the model to a population of 10 neurons and found we
2289 didn't manage to finish the process. Since, our goal was to find a model to scale to hundreds
2290 or thousands of neurons, we decided that this model was no longer worth pursuing.

2291 **5.2 A multiscale model for hierarchical data applied to**
2292 **neuronal data**

2293 In their paper Kolaczyk et al (2001) developed a framework for a modelling hierarchically
2294 aggregated data, and making inferences based on a model arising from this framework. They
2295 assumed that a hierarchical aggregation existed on the data in question, where each element at
2296 each level of the hierarchy had some associated measurements, an associated mean process,
2297 which was the expected value of these measurements. They also assumed that the measure-
2298 ments of each parent were equal to the sum of the measurements from all of its children.
2299 They showed that these assumptions gave rise to a relationship between parent and child
2300 measurements across all levels of the hierarchy, where the product of the likelihood of the
2301 parameters of the lowest level of the hierarchy can be expressed as products of conditional
2302 likelihoods of the elements of higher levels of the hierarchy (Kolaczyk and Huang, 2010).

5.2. A multiscale model for hierarchical data applied to neuronal data

2303 We hoped that the hierarchical structure of the brain (regions to subregions to cells) and a
2304 high level activity measure (fMRI or EEG) could be combined with this model to infer lower
2305 level activity from a high level measure.

2306 They gave examples of these expressions for measurements sampled from Gaussian dis-
2307 tributions, and Poisson distributions, and showed the definitions of the hierarchical param-
2308 eters which reparametrise the distribution of these data taking the hierarchy into account.
2309 They go on to suggest prior distributions for this multiscale model, and integrate these priors
2310 to give posterior distributions for the measurements from each element at each level in the hi-
2311 erarchy, and expressions for the MAP estimated parameters of each the associated processes
2312 (Kolaczyk and Huang, 2010).

2313 We implemented their model in Python by creating some synthetic data from Poisson
2314 distributions, and defining a hierarchy by agglomerating these data. We calculated the MAP
2315 estimates using our knowledge of the hierarchy, and using the expressions given in the paper.
2316 We found that the MAP estimates were far less accurate than would be achieved by simply
2317 ignoring the hierarchy during estimation, and using a maximum likelihood approach. After
2318 that, we decided to move on.

2319 **Chapter 6**

2320 **Discussion**

2321 In this project, we attempted to address some of the challenges in data collection from
2322 large neuronal ensembles (specifically with calcium imaging) and some of the problems in
2323 analysing the data collected from large neuronal ensembles.

2324 Firstly, we investigated the relationship between cell biochemistry, action potentials and
2325 the fluorescence traces produced by fluorescent calcium indicators. We did this by building
2326 a biophysical model that takes in a spike train and returns the fluorescence trace that that
2327 spike would induce. The model included mechanics for the binding of calcium to fluorescent
2328 and endogenous mobile and immobile buffers, and the consequent changes in concentration
2329 of free and bounded calcium. The model consisted of 17 parameters, 13 of which were
2330 set according to data from the literature, and 4 of which were free parameters. We trained
2331 the model using simultaneously collected spiking and calcium imaging data (Berens et al.,
2332 2018). We fitted the model by matching the $\Delta F/F_0$ in response to an action potential, and
2333 by matching the power spectrum of the actual fluorescence trace. This meant that our model
2334 would include the correct amount of noise as well as return the correct change in amplitude
2335 in response to an action potential.

2336 Since our model produced fluorescence traces, we could apply spike inference algorithms
2337 to the modelled fluorescence traces that our model produced after training, and compare the
2338 performance of the algorithms on the modelled traces to their performance on the real traces.
2339 We used three spike inference algorithms, two of which were based on modelling the cal-
2340 cium trace as an autoregression (Friedrich and Paninski, 2016; Pnevmatikakis et al., 2016),
2341 and another inference algorithm that was a little more biologically inspired, but amounted to
2342 a very similar algorithm (Deneux et al., 2016). We compared the performance of the algo-
2343 rithms by using them to infer spikes from 20 real and modelled fluorescence traces induced
2344 by 20 corresponding real spike trains. We then used several binary classification measures
2345 (true positive rate, accuracy etc.) to asses the quality of the spike inference for the real and

2346 modelled fluorescence traces. We found that the spike inference algorithms performed sim-
2347 ilarly on real and modelled traces, showing that our model is capturing at least some of the
2348 characteristics of the real fluorescence traces.

2349 In order to investigate the effect of indicator characteristics on the modelled fluorescence
2350 trace and spike inference quality, we perturbed the indicator's affinity and dissociation rate
2351 in parallel, keeping the ratio of the two the same for all perturbations. We measured the SNR
2352 of the trace, and the true positive rate of the spike inference algorithms at each perturbed
2353 value pair. We found that perturbing the values lower caused in decrease in SNR and spike
2354 inference quality. This shows that our model could be used to test theoretical fluorescent cal-
2355 cium indicators without having to actually manufacture them. Experimental neuroscientists
2356 could also use our model to judge which indicator characteristics are most influential in their
2357 experimental context.

2358 We then investigated the effect of perturbing buffer concentration, and indicator concen-
2359 tration, on the signal-to-noise ratio of the modelled fluorescence trace and spike inference
2360 quality. This was a worthwhile experiment because endogenous buffer concentrations vary
2361 from cell to cell (Bartol et al., 2015; Maravall et al., 2000; Neher and Augustine, 1992), as
2362 does indicator expression (Chen et al., 2013). We found that extreme perturbations away
2363 from the indicator concentration taken from the literature lowered the SNR of the trace, and
2364 the spike inference quality. We also found that increases in the concentration of endogenous
2365 buffer above the value taken from the literature caused a decrease in the SNR and spike infer-
2366 ence quality. This reiterates that the indicator and endogenous buffers compete to bind with
2367 free calcium molecules, and this has an effect on fluorescence and consequently on spike
2368 inference.

2369 We then created some synthetic spike trains with controlled mean firing rates sampled
2370 the rates from an Ornstein-Uhlenbeck process. We found that the higher the firing rate, the
2371 lower the accuracy of the spike inference algorithms. But the mean firing could perhaps be
2372 inferred from the amplitude of the fluorescence traces. The higher firing rate, the higher the
2373 amplitude. Calibrating the model to facilitate and accurate measurement would require some
2374 kind of ground truth, but relative comparisons could be made without any other knowledge
2375 of the underlying spiking process.

2376 One obvious limitation to our model is the lack of binding mechanics for both the indi-
2377 cator and endogenous buffers. Greenberg et al included these mechanics in their successful
2378 spike inference model. We felt that the timescale of these binding mechanics was so small in
2379 comparison to the fluorescence dynamics that omitting them would make no difference. But

2380 it is possible that their inclusion would improve our model.

2381 After investigating the difficulties with inferring spiking data from calcium imaging data,
2382 we moved from data collection to analysis and we decided to implement a new network anal-
2383 ysis method on data from a neuronal ensemble. Using an electrophysiological dataset with
2384 spike sorted data from 9 different brain regions in 3 mice (Steinmetz, Carandini, and Harris,
2385 2019), we binned the spike times for each cell into spike counts for each cell and measured
2386 the correlation coefficients between these spike counts for a selection of cells evenly dis-
2387 tributed across the 9 regions. We repeated these measurements for time bin widths ranging
2388 from 5ms to 3s. We rectified these measurements and, for a given time bin width, used them
2389 as weights for a weighted undirected graph where each node represents a neuron, and the
2390 weight of each edge is the correlation between the neurons represented by the nodes on that
2391 edge. We applied a novel spectral analysis and community detection method (Humphries
2392 et al., 2019) to this network. This clustered the nodes in our ensemble into communities
2393 whose behaviour was more correlated than expected. Our measure of 'expected correlation
2394 strength' were based on a random network that matched our data network's sparsity and total
2395 weight. We compared the detected communities to the anatomical division of our cells using
2396 clustering comparison measures. We then conditioned the binned spike counts on the be-
2397 haviour of the mouse using the principal components of a video of the mouses face recorded
2398 simultaneously with the electrophysiology. We broke the total covariance down into 'spike
2399 count covariance' and 'signal covariance' components conditioning on the behavioural data
2400 and using the law of total covariance. We then repeated our analysis for spike count corre-
2401 lations, and signal correlation. Finally, since our community detection method was only valid
2402 on graphs with non-negative weights, we used different methods for creating a non-negative
2403 graph from our total correlations, and we repeated our analysis on those graphs.

2404 Our first finding was that the time bin width used to bin spike times into spike counts had
2405 a effect on the mean magnitude of the correlations measured. The wider the bin, the higher
2406 the correlations. Not only that, we separated the pairs into positively and negative correlated
2407 pairs, and we found that positively correlated pairs have greater correlation coefficients when
2408 using a wider bin, and negatively correlated pairs have more negative correlation coefficients
2409 when using a wider bin. We also found that the width of the bin used had an effect on the
2410 distribution of the spike counts. For smaller bin widths, the distribution of spike counts was
2411 better represented by a skewed distribution like the Poisson distribution. For wider bins, the
2412 spike counts were better represented by a Gaussian distribution.

2413 Next we investigated the differences between correlations within regions and between

regions. When we divided the pairs according to those two groups, we found that the mean within-region correlations were higher at every bin width, and the difference between the two means grew with increasing bin width. When we split the pairs of cells according to their regions, we found that the mean within-region correlations in any given region were usually greater than the mean between-region correlations for any region pair involving that region. The difference between the mean within-region correlation and the highest between-region correlations involving that region grew smaller with increasing bin width. To investigate this further, we plotted these mean correlations in matrices. Although the mean within-region correlations were usually the highest value in their row or column, as the bin width increased, the mean between-region correlations grew in magnitude relative to the within-region figure.

Next we chose a null network model, and we used the ‘Network Noise Rejection’ process (Humphries et al., 2019) to check for additional structure in our correlation based data network that was not captured by the null model. We found additional structure for any bin width that we used. We also found that the dimensionality of the additional structure reduced as we increased the bin width. This could mean that the processes or representations that take place over longer timescales within the brain also take place in a lower dimensional space.

We applied a community detection method (Humphries, 2011) to the signal correlation networks arising from the network noise rejection. We found that the number of communities detected decreased with increasing bin width. We also noticed that at shorter bin widths, the detected communities were more likely to consist of cells from one brain region only. We investigated this further by using clustering comparison methods to compare the detected communities with the anatomical division of the cells. We found that for short timescales $< 50\text{ms}$ correlated communities tended to exist within anatomical regions, and for longer timescales $> 100\text{ms}$, the correlated communities tended to exist across anatomical regions. This is broadly in agreement with a similar finding for EEG data from humans performing semantic or memory tasks (Stein and Sarnthein, 2000). Von Stein et al. (2000) found that visual processing taking place locally in the visual system was captured in the gamma frequency range (25 – 70Hz), while semantic processing was captured in the beta range (12 – 18Hz), and tasks involving mental imagery and working memory retention were captured in the theta and alpha ranges (4 – 8Hz, and 8 – 12Hz respectively).

We then conditioned our correlation measures on the the mouse’s behaviour. This allowed us to create spike count correlation (or noise correlation) networks, and signal correlation networks (Cohen and Kohn, 2011). We applied our analysis to these networks. For the

spike count correlation networks we found very similar results to the total correlation networks. More communities at smaller bin widths, and communities resembled the anatomical division at smaller bin widths. Given that recent findings show that behaviour can account for correlated spiking in many areas of the brain (Stringer et al., 2019), these results for the spike count correlation show that this correlated behaviour is still processed locally at short timescales, while processes and representations that take more time make use of correlated activity across multiple regions.

For the signal correlations, we still found additional structure in these networks. But we always detected a smaller number of communities. These communities also had no relation to the anatomical division of the cells. This result shows that there are groups of cells across multiple brain regions that are activated similarly by certain behaviours.

All of the networks so far were based on rectified correlation measures, because the network noise rejection and community detection processing is (currently) only valid for networks with non-negative weights. For the final part of our analysis, we tried different ways of transforming our total correlations into non-negative quantities before applying our analysis. First of all we took the absolute value of our correlation measures. Our results were very similar to those for the rectified correlations with the exception that we detected more communities consistently. It is possible that using this method detects both positively and negatively correlated communities.

We also tried reversing the sign of all the correlations, then rectifying the network. We hope that this would allow us to detect the negatively correlated communities. We did detect communities in these networks, but never more than three, and these communities bore no relationship with the anatomical distribution of the cells.

There is a lot of potential for network science applications in computational neuroscience. For example, some pairwise measure other than correlation coefficients could be used as the weights of the graph. The synaptic connections between cells can be isolated in-vitro (Okun et al., 2015). A map of these synaptic connections could be used as the basis for directed graphs. The analysis methods applicable to directed graphs could give insights about the formation of synaptic connections, or the dynamic changes in these connections over time. Other methods of community detection could be used on directed or undirected graphs. We used a ‘hard’ clustering method in our research, that is, each neuron could be a member of one cluster/community only. ‘Fuzzy-clustering’ methods do exist, where each element of the set to be clustered could be a member of more than one cluster (Baadel, Thabtah, and Lu, 2016).

Having spent much time investigating correlated behaviour using coefficients of spike counts, we decided to try another method for capturing correlated behaviour in neuronal ensembles. We used electrophysiological data taken from 5 brain regions of an awake mouse exposed to visual stimuli (Steinmetz et al., 2019). We modelled the number of active neurons in a given brain region as the number of successes in a collection of dependent Bernoulli random variables using the Conway-Maxwell-binomial distribution. To avoid violating the Bernoulli assumption, we binned the spike times using 1ms bins. The Conway-Maxwell-binomial distribution is a two parameter extension of the standard binomial distribution. The extra parameter allows the distribution to capture possible positive or negative association between the Bernoulli trials (Kadane, 2016). This means that we are assuming that all the neurons are dependent in the same way. This is not an accurate assumption, but it allows us model the data in a simple way.

First of all we established that there were changes in the number of active neurons in response to the visual stimuli. This was the case in the hippocampus, thalamus, and primary visual cortex. Each region had its own signature response. We measured the mean and variance of the number of active neurons in a sliding window starting before stimulus onset, and finishing after the end of stimulus presentation.

As well as the Conway-Maxwell-binomial distribution, we also fitted binomial, and beta-binomial distributions to the number of active neurons in a sliding window. We found that the Conway-Maxwell-binomial distribution was the best fit for over 90% of the samples. This means that the COMb distribution is capturing some dependency between the neurons, because the binomial distribution assumes independence. Also the COMb distribution captures this dependence more accurately than the beta-binomial distribution, which does have some capacity for over dispersion.

Next we showed that the Conway-Maxwell-binomial distribution captured the change in association at stimulus onset better than the correlation coefficient. The extremely small bin width artificially shrunk the correlation coefficient to the point where this measurement didn't detect any correlated activity. But the association parameter of the COMb distribution detected some positive association between the neurons at stimulus onset. So, for particularly short time bins, where neurons can be treated as Bernoulli random variables, the Conway-Maxwell-binomial distribution is a good way to capture correlated behaviour. There are other measurements for capturing association to which this distribution should be compared. Cross-correlograms could be used for some measure of synchrony, for example.

2514 Finally, we replicated a famous finding of Churchland et al. (2010) relating to the quenching
2515 of neural variability at stimulus onset, thereby finding a parallel between this reduction
2516 in the Fano factor and a reduction in the association parameter of the COMb distribution.

2517 We showed that computational neuroscientists can make progress by being inventive with
2518 their statistical models. A similar distribution to investigate would be the Conway-Maxwell-
2519 Poisson distribution. This is similar to the standard Poisson distribution, but with an addi-
2520 tional parameter that allows for over- or under- dispersion relative to a Poisson distribution.
2521 This might be ideal for modelling firing rates of individual neurons. Some interaction be-
2522 tween the fitted parameters could capture the association between neurons.

2523 There is one technology that has the potential to take over from both electrophysiology
2524 and calcium imaging. The technique of voltage imaging has become more useful in recent
2525 years. The aim for neuroscience would be to develop a voltage imaging dye or protein that
2526 images the membrane potential of a neuron with enough spatial and temporal resolution to de-
2527 tect action potentials. The voltage imaging dyes that have been developed so far do not have
2528 high enough spatial resolution to single out individual cells in-vivo using staining (Bando
2529 et al., 2019). But, genetically encoded voltage indicators have been developed that have high
2530 enough resolution to indicate individual spikes and subthreshold activity from small numbers
2531 of cells in the striatum, hippocampus, and cortex of awake behaving mice (Piatkevich et al.,
2532 2019). These indicators have the potential to take over from calcium imaging, and if imaging
2533 deep within the brain becomes possible, electrophysiology could also be replaced. This is
2534 speculation, but the potential is there.

2535 Bibliography

- 2536 Allen, William E. et al. (2019). “Thirst regulates motivated behavior through modulation of
2537 brainwide neural population dynamics”. In: *Science* 364.6437.
- 2538 Baadel, S., F. Thabtah, and J. Lu (2016). “Overlapping clustering: A review”. In: *2016 SAI
2539 Computing Conference (SAI)*, pp. 233–237.
- 2540 Baldassano, Christopher et al. (2017). “Discovering Event Structure in Continuous Narrative
2541 Perception and Memory”. In: *Neuron* 95.3, 709 –721.e5.
- 2542 Bando, Yuki et al. (2019). “Genetic voltage indicators”. In: *BMC Biology* 17.1, p. 71.
- 2543 Bartol, Thomas M. et al. (2015). “Computational reconstitution of spine calcium transients
2544 from individual proteins”. In: *Frontiers in Synaptic Neuroscience* 7, p. 17.
- 2545 Berens, Philipp et al. (May 2018). “Community-based benchmarking improves spike rate in-
2546 ference from two-photon calcium imaging data”. In: *PLOS Computational Biology* 14.5,
2547 pp. 1–13.
- 2548 Bezanson, Jeff et al. (Sept. 2012). “Julia: A Fast Dynamic Language for Technical Comput-
2549 ing”. In: *MIT*.
- 2550 Buccino, Alessio P. et al. (2019). “SpikeInterface, a unified framework for spike sorting”. In:
2551 *bioRxiv*.
- 2552 Chen, Tsai-Wen et al. (July 2013). “Ultrasensitive fluorescent proteins for imaging neuronal
2553 activity”. In: *Nature* 499, 295–300.
- 2554 Churchland, Mark M. et al. (2010). “Stimulus onset quenches neural variability: a widespread
2555 cortical phenomenon”. eng. In: *Nature neuroscience* 13.3. 20173745[pmid], pp. 369–378.
- 2556 Cohen, Marlene R. and Adam Kohn (2011). “Measuring and interpreting neuronal corre-
2557 lations”. In: *Nature Neuroscience* 14.7, pp. 811–819.
- 2558 Cohen, Marlene R. and John H. R. Maunsell (2009). “Attention improves performance pri-
2559 marily by reducing interneuronal correlations”. eng. In: *Nature neuroscience* 12.12. 19915566[pmid],
2560 pp. 1594–1600.
- 2561 Dana, Hod et al. (Sept. 2014). “Thy1-GCaMP6 Transgenic Mice for Neuronal Population
2562 Imaging In Vivo”. In: *PloS one* 9, e108697.

- 2563 deCharms, R. Christopher and Michael M. Merzenich (1996). “Primary cortical representation of sounds by the coordination of action-potential timing”. In: *Nature* 381.6583,
2564 pp. 610–613.
- 2566 Deneux, Thomas et al. (July 2016). “Accurate spike estimation from noisy calcium signals
2567 for ultrafast three-dimensional imaging of large neuronal populations in vivo”. In: *Nature
2568 Communications* 7.1.
- 2569 Dombeck, Daniel A. et al. (2010). “Functional imaging of hippocampal place cells at cellular
2570 resolution during virtual navigation”. In: *Nature Neuroscience* 13.11, pp. 1433–1440.
- 2571 Éltes, Tímea et al. (2019). “Improved spike inference accuracy by estimating the peak am-
2572 plitude of unitary [Ca₂₊] transients in weakly GCaMP6f-expressing hippocampal pyra-
2573 midal cells”. In: *The Journal of Physiology* 597.11, pp. 2925–2947.
- 2574 Faas, Guido C. et al. (2011). “Calmodulin as a direct detector of Ca₂₊ signals”. In: *Nature
2575 Neuroscience* 14.3, pp. 301–304.
- 2576 Fiala, John C. and Kristen M. Harris (1999). *Dendrite Structure*.
- 2577 Flach, Boris (Sept. 2013). “A Class of Random Fields on Complete Graphs with Tractable
2578 Partition Function”. In: *IEEE transactions on pattern analysis and machine intelligence*
2579 35, pp. 2304–6.
- 2580 Forney, G. D. (1973). “The viterbi algorithm”. In: *Proceedings of the IEEE* 61.3, pp. 268–
2581 278.
- 2582 Fosdick, Bailey et al. (Aug. 2016). “Configuring Random Graph Models with Fixed Degree
2583 Sequences”. In: *SIAM Review* 60.
- 2584 Friedrich, Johannes and Liam Paninski (2016). “Fast Active Set Methods for Online Spike In-
2585 ference from Calcium Imaging”. In: *Advances in Neural Information Processing Systems*
2586 29. Ed. by D. D. Lee et al. Curran Associates, Inc., pp. 1984–1992.
- 2587 Ganmor, Elad, Ronen Segev, and Elad Schneidman (2011). “Sparse low-order interaction
2588 network underlies a highly correlated and learnable neural population code”. In: *Pro-
2589 ceedings of the National Academy of Sciences* 108.23, pp. 9679–9684.
- 2590 Girard, P., J. M. Hupé, and J. Bullier (2001). “Feedforward and Feedback Connections Be-
2591 tween Areas V1 and V2 of the Monkey Have Similar Rapid Conduction Velocities”. In:
2592 *Journal of Neurophysiology* 85.3. PMID: 11248002, pp. 1328–1331.
- 2593 Greenberg, David et al. (Nov. 2018). “Accurate action potential inference from a calcium
2594 sensor protein through biophysical modeling:” in:
- 2595 Gründemann, Jan et al. (2019). “Amygdala ensembles encode behavioral states”. In: *Science*
2596 364.6437.

Bibliography

- 2597 Hodgkin, A. L. and A. F. Huxley (1939). “Action Potentials Recorded from Inside a Nerve
2598 Fibre”. In: *Nature* 144.3651, pp. 710–711.
- 2599 Humphries, Mark et al. (Jan. 2019). “Spectral rejection for testing hypotheses of structure in
2600 networks”. In:
- 2601 Humphries, Mark D. (2011). “Spike-Train Communities: Finding Groups of Similar Spike
2602 Trains”. In: *Journal of Neuroscience* 31.6, pp. 2321–2336.
- 2603 Jun, James J. et al. (2017). “Fully integrated silicon probes for high-density recording of
2604 neural activity”. In: *Nature* 551.7679, pp. 232–236.
- 2605 Kadane, Joseph B. (June 2016). “Sums of Possibly Associated Bernoulli Variables: The
2606 Conway–Maxwell-Binomial Distribution”. In: *Bayesian Anal.* 11.2, pp. 403–420.
- 2607 Kilhoffer, Marie-Claude et al. (Sept. 1992). “Use of Engineered Proteins With Internal Tryp-
2608 tophean Reporter Groups and Perturbation Techniques to Probe the Mechanism of Ligand-
2609 Protein Interactions: Investigation of the Mechanism of Calcium Binding to Calmodulin”.
2610 In: *Biochemistry* 31.34, pp. 8098–8106.
- 2611 Koch, Christoff (1999). *Biophysics of Computation: Information Processing in Single Neu-*
2612 *rons*. Oxford University Press.
- 2613 Kolaczyk, Eric and Haiying Huang (Sept. 2010). “Multiscale Statistical Models for Hierar-
2614 chical Spatial Aggregation”. In: *Geographical Analysis* 33, pp. 95 –118.
- 2615 Lee, Suk-HO et al. (July 2000). “Differences in Ca²⁺ buffering properties between excitatory
2616 and inhibitory hippocampal neurons from the rat”. In: *The Journal of Physiology* 525.
- 2617 Litwin-Kumar, Ashok, Maurice Chacron, and Brent Doiron (Sept. 2012). “The Spatial Struc-
2618 ture of Stimuli Shapes the Timescale of Correlations in Population Spiking Activity”. In:
2619 *PLoS computational biology* 8, e1002667.
- 2620 Maravall, M et al. (May 2000). “Estimating intracellular calcium concentrations and buffer-
2621 ing without wavelength ratioing”. In: *Biophysical Journal* 78.5, pp. 2655–2667.
- 2622 Maugis, Pa (Jan. 2014). “Event Conditional Correlation: Or How Non-Linear Linear Depen-
2623 dence Can Be”. In:
- 2624 Meilă, Marina (2007). “Comparing clusterings—an information based distance”. In: *Journal*
2625 *of Multivariate Analysis* 98.5, pp. 873 –895.
- 2626 Murray, John D. et al. (2014). “A hierarchy of intrinsic timescales across primate cortex”. In:
2627 *Nature Neuroscience* 17.12, pp. 1661–1663.
- 2628 Neher, E. and G. J. Augustine (1992). “Calcium gradients and buffers in bovine chromaffin
2629 cells”. eng. In: *The Journal of physiology* 450. 1331424[pmid], pp. 273–301.

- 2630 O'Donnell, Cian et al. (Jan. 2017). "The population tracking model: a simple, scalable statistical model for neural population data". English. In: *Neural Computation* 29.1, pp. 50–93.
- 2631
- 2632
- 2633 Okun, Michael et al. (2015). "Diverse coupling of neurons to populations in sensory cortex". In: *Nature* 521.7553, pp. 511–515.
- 2634
- 2635 Ouzounov, Dimitre G. et al. (2017). "In vivo three-photon imaging of activity of GCaMP6-labeled neurons deep in intact mouse brain". eng. In: *Nature methods* 14.4. 28218900[pmid], pp. 388–390.
- 2636
- 2637
- 2638 Patterson, Carolyn A. et al. (2014). "Similar adaptation effects in primary visual cortex and area MT of the macaque monkey under matched stimulus conditions". In: *Journal of Neurophysiology* 111.6. PMID: 24371295, pp. 1203–1213.
- 2639
- 2640
- 2641 Peron, Simon P. et al. (2015). "A Cellular Resolution Map of Barrel Cortex Activity during Tactile Behavior". In: *Neuron* 86.3, pp. 783–799.
- 2642
- 2643 Piatkevich, Kiryl D. et al. (2019). "Population imaging of neural activity in awake behaving mice". In: *Nature* 574.7778, pp. 413–417.
- 2644
- 2645 Pnevmatikakis, E.A. et al. (Jan. 2016). "Simultaneous Denoising, Deconvolution, and Demixing of Calcium Imaging Data". In: *Neuron* 89.2, pp. 285–299.
- 2646
- 2647 Pnevmatikakis, Eftychios et al. (Nov. 2013). "Bayesian spike inference from calcium imaging data". In: *Conference Record - Asilomar Conference on Signals, Systems and Computers*.
- 2648
- 2649 Pnevmatikakis, Eftychios et al. (Sept. 2014). "A structured matrix factorization framework for large scale calcium imaging data analysis". In:
- 2650
- 2651 Schneidman, Elad et al. (2006). "Weak pairwise correlations imply strongly correlated network states in a neural population". eng. In: *Nature* 440.7087. 16625187[pmid], pp. 1007–1012.
- 2652
- 2653
- 2654 Shannon, C. E. (1948). "A Mathematical Theory of Communication". In: *Bell System Technical Journal* 27.3, pp. 379–423.
- 2655
- 2656 Shimazaki, Hideaki et al. (2012). "State-space analysis of time-varying higher-order spike correlation for multiple neural spike train data". eng. In: *PLoS computational biology* 8.3. 22412358[pmid], e1002385–e1002385.
- 2657
- 2658
- 2659 Staude, Benjamin, Sonja Grün, and Stefan Rotter (2010). "Higher-Order Correlations and Cumulants". In: *Analysis of Parallel Spike Trains*. Ed. by Sonja Grün and Stefan Rotter. Boston, MA: Springer US, pp. 253–280.
- 2660
- 2661

Bibliography

- 2662 Stein, Astrid von and Johannes Sarnthein (2000). “Different frequencies for different scales
2663 of cortical integration: from local gamma to long range alpha/theta synchronization”. In:
2664 *International Journal of Psychophysiology* 38.3, pp. 301 –313.
- 2665 Steinmetz, Nick, Matteo Carandini, and Kenneth D. Harris (2019). ”*Single Phase3*” and
2666 ”*Dual Phase3*” *Neuropixels Datasets*.
- 2667 Steinmetz, Nick et al. (Mar. 2019). “Eight-probe Neuropixels recordings during spontaneous
2668 behaviors”. In:
- 2669 Stevenson, Ian H. and Konrad P. Kording (2011). “How advances in neural recording affect
2670 data analysis”. In: *Nature Neuroscience* 14.2, pp. 139–142.
- 2671 Stringer, Carsen et al. (2019). “Spontaneous behaviors drive multidimensional, brainwide
2672 activity”. In: *Science* 364.6437.
- 2673 Tada, Mayumi et al. (2014). “A highly sensitive fluorescent indicator dye for calcium imaging
2674 of neural activity in vitro and in vivo”. In: *European Journal of Neuroscience* 39.11,
2675 pp. 1720–1728.
- 2676 Tian, Lin et al. (2009). “Imaging neural activity in worms, flies and mice with improved
2677 GCaMP calcium indicators”. eng. In: *Nature methods* 6.12. 19898485[pmid], pp. 875–
2678 881.
- 2679 Tkačik, Gašper et al. (2014). “Searching for collective behavior in a large network of sen-
2680 sory neurons”. eng. In: *PLoS computational biology* 10.1. 24391485[pmid], e1003408–
2681 e1003408.
- 2682 Treves, Alessandro and Stefano Panzeri (1995). “The Upward Bias in Measures of Informa-
2683 tion Derived from Limited Data Samples”. In: *Neural Computation* 7.2, pp. 399–407.
- 2684 Vinh, Nguyen Xuan, Julien Epps, and James Bailey (Dec. 2010). “Information Theoretic
2685 Measures for Clusterings Comparison: Variants, Properties, Normalization and Correc-
2686 tion for Chance”. In: *J. Mach. Learn. Res.* 11, 2837–2854.
- 2687 Vogelstein, Joshua T. et al. (Oct. 2010). “Fast nonnegative deconvolution for spike train infer-
2688 ence from population calcium imaging”. In: *Journal of neurophysiology* 104.6, 295–300.
- 2689 Wierzyński, ”Casimir M. et al. (2009). ””State-Dependent Spike-Timing Relationships be-
2690 tween Hippocampal and Prefrontal Circuits during Sleep””. In: ”*Neuron*” ”61”. ”4”, ”587
2691 –596”.
- 2692 Zariwala, Hatim A. et al. (2012). “A Cre-dependent GCaMP3 reporter mouse for neuronal
2693 imaging in vivo”. eng. In: *The Journal of neuroscience : the official journal of the Society
2694 for Neuroscience* 32.9. 22378886[pmid], pp. 3131–3141.

- 2695 Zou, Hui and Trevor Hastie (2005). “Regularization and variable selection via the Elastic
2696 Net”. In: *Journal of the Royal Statistical Society, Series B* 67, pp. 301–320.